ABSTRACT

Title of Document: METALS IN ARC MAGMAS: THE ROLE OF CU-RICH SULFIDE PHASES.

Michael James Mengason, Ph.D., 2011

Directed By: Dr. Philip A. Candela, Professor
Dr. Philip M. Piccoli, Senior Research Scientist
Geology Department

Based on experiments performed on hydrous andesitic melts at 1000°C, 150 MPa, fO_2 from the Co–CoO to Ni–NiO buffer, and log fS_2 equal to -0.5 to -1.5 (bar), greater than 32 ± 4 ppm copper (all uncertainties = 1 sigma, standard deviation of the mean) in the silicate melt favors the formation of a Cu–Fe sulfide liquid *(CFSL)* relative to pyrrhotite at sulfide saturation. This concentration is well within the range encountered in intrusive and extrusive rocks suggesting that saturation by sulfide liquids is a common occurrence in magmatic arc systems consistent with observations in naturally occurring andesites.

Nernst-type partition coefficients determined from these experiments highlight the importance of accurately modeling the composition of the sulfide phase present during partial melting or fractional crystallization: $D^{pyrrhotite/melt} = 1320 \pm 220$ for Cu,

1.73 ± 0.37 for Mo, 90 ± 19 for Ag, and 500 ± 87 for Au, whereas $D^{CFSL/melt}$ = 7,800 ± 1,400 for Cu, 0.45 ± 0.14 for Mo, 6,800 ± 1,300 for Ag, and 84,000 ± 19,000 for Au.

Data from these experiments support a direct correlation between the solubility of gold and the concentration of sulfur in the silicate melt at low fO_2, as well as a dependence of the solubility of gold on $fS_2^{0.25}$ in pyrrhotite and CFSL.

As a part of this research, pyrrhotite of variable copper concentration was equilibrated at 1000°C in sealed evacuated silica tubes to determine a method that allows the equation of Toulmin and Barton (1964) to be used to calculate fS_2 for Cu-bearing pyrrhotite. This method is consistent for pyrrhotite with up to 6 wt % Cu by using N=2*[(XCu+XFe)/(1.5XCu+XFe+XS)].

These data suggest that separation of CFSL from the magma along with crystalline phases during fractional crystallization can reduce the likelihood of magmatic hydrothermal ore formation. For example, modeling 30 % Rayleigh fractional crystallization (F=1.0 to F=0.7), with 0.1% sulfide among the separating phases, and an initial 65 ppm Cu in the silicate melt, would result in the sequestration of up to 50% of the initial Ag, 60 % Cu, and > 99 % Au.

METALS IN ARC MAGMA: THE ROLE OF CU-RICH SULFIDE PHASES

By

Michael James Mengason

Dissertation submitted to the Faculty of the Graduate School of the
University of Maryland, College Park, in partial fulfillment
of the requirements for the degree of
Doctor or Philosophy
2011

Advisory Committee:
Dr. Philip A. Candela, Professor, Co-Chair
Dr. Philip M. Piccoli, Senior Research Scientist, Co-Chair
Dr. Michael Brown, Professor
Dr. Sarah Penniston-Dorland, Assistant Professor
Dr. Bryan W. Eichhorn, Professor, Dean's Representative

© Copyright by
Michael James Mengason
2011

Preface

This dissertation was structured to incorporate two papers that are presented in chapters 2 and 3. The paper in chapter 2 has been published as Mengason, M, Piccoli, P. M. and Candela, P.A. (2010) An evaluation of the effect of copper on the estimation of sulfur fugacity (fS_2) from pyrrhotite composition. Economic Geology; 105:1163–1169. The paper in chapter 3 is in preparation for publication and will be submitted shortly.

Dedication

To Suzanne, Elise, and Genevieve—my awesome family.

Acknowledgements

This work was supported by the National Science Foundation (EAR 0911098, EAR 0738992). The experimental laboratory of the Laboratory for Mineral Deposits Research (LMDR) used for this work was overhauled with financial support of the National Science Foundation (EAR 0842205) and the University of Maryland. I acknowledge the support of the Maryland NanoCenter and its NispLab. The NispLab is supported in part by the NSF as a MRSEC Shared Experimental Facility. I would also like to acknowledge the assistance given by the Plasma Mass Spectrometry Laboratory at the University of Maryland, including the help of Dr. Bill McDonough and Dr. Richard Ash. Reflected light microscopy was performed in the microscopy laboratory of Dr. Aaron Martin and Dr. Sarah Penniston-Dorland.

I would especially like to acknowledge the members of the LMDR, Dr. Phil Candela, Dr. Phil Piccoli, Dr. Zoltan Zajacz, Dr. Ryan Kerrigan, and Brian Tattitch for their help, ideas, and support throughout this project.

Table of Contents

Preface ii
Dedication iii
Acknowledgements iv
Table of Content v
List of Tables vii
List of Figures viii

Chapter 1: Introduction 1
1.1 Porphyry deposits 2
1.2 Sulfides in subduction zones 4
1.3 Partition coefficients 6
1.4 Goals 8
1.5 Lab development, equipment, and methods 8
1.6 Pyrrhotite composition and sulfur fugacity (fS_2) 13
1.7 Experiments on sulfide solubility and partitioning 15
1.8 Notes 18

Chapter 2: An evaluation of the effect of copper on the estimation of sulfur fugacity (*f*S_2) from pyrrhotite composition 19
2.1 Abstract 19
2.2 Introduction 20
2.3 Experimental methods 25
2.4 Analytical methods 29
2.5 Results 29
2.6 Discussion 32
2.7 Conclusions 39
2.8 Acknowledgements 39
2.9 Appendix 40

Chapter 3: Conditions for Cu-rich sulfide saturation of andesitic melt capable of influencing Ag and Au deposit formation 42
3.1 Abstract 42
3.2 Introduction 44
3.2.1 Copper in arc magmas 49
3.2.2 Bulk rock analysis of volcanic and plutonic rock 49
3.2.3 Data from igneous rocks in arcs 51
3.2.4 Silicate and sulfide melt inclusions in dikes 54

3.2.5 Sulfide inclusions in erupted minerals and quenched silicate melts 55
3.2.6 Cu–Fe sulfide saturation in arc magma 56
3.3 Experimental methods 58
3.3.1 Design of the Cu–Fe–S system experiments 62
3.3.2 Design of the Cu–Fe–S–O system experiments 64
3.3.3 Design of the hydrothermal experiments 66
3.3.4 Furnace assembly 77
3.3.5 Sample processing 80
3.4 Analytical methods 82
3.4.1 Reflected light microscopy 82
3.4.2 EPMA 82
3.4.2.1 Glass 82
3.4.2.2 Sulfides 83
3.4.3 LA–ICP–MS 84
3.5 Results 86
3.5.1 Silica tube experiments 86
3.5.2 Hydrothermal experiments 92
3.5.3 Equilibrium 95
3.5.4 Run product glasses 98
3.5.5 Solubility of Au in the silicate melt 102
3.5.6 Run product sulfides 104
3.5.7 Solubility of Au in sulfide phase 110
3.5.8 Concentration of copper in a silicate melt saturated with pyrrhotite and CFSL 114
3.5.9 Partition coefficients 115
3.5.10 Summary of partitioning coefficients 118
3.6 Discussion 121
3.6.1 Origins of andesitic magmas and sulfide–silicate interactions 121
3.6.2 Sulfide separation and ore metal ratios in arc magmas: partial melting .. 122
3.6.3 Sulfide separation and ore metal ratios in arc magmas: fractional crystallization 132
3.7 Conclusions 140

Chapter 4: Conclusions 146
4.1 Summary of Cu–Fe sulfide phase assemblages as a function of temperature 147
4.2 Tools and observations 150
4.3 Effect of Cu–Fe sulfide on metal budgets 154

Bibliography 158

List of Tables

Chapter 1

Table 1-1 Partition coefficients (Cu, Mo, Ag, and Au) from the literature 7

Chapter 2

Table 2-1 Composition of experimental charges 28
Table 2-2 Run product compositions and calculated sulfur fugacities 31
Table 2-3 Calculated sulfur fugacity from volcanic pyrrhotite 36

Chapter 3

Table 3-1 Compositions of starting material sulfides (by EMPA) 62
Table 3-2 Contents of the Cu–Fe–S experiments 64
Table 3-3 Contents of the Cu–Fe–S–O experiments 66
Table 3-4 Contents of the hydrothermal experiments..... 68
Table 3-5 Compositions of starting material glasses (by EMPA and LA–ICP–MS) . 70
Table 3-6 Compositions of sensor pyrrhotite from silica tube experiments..... 88
Table 3-7 Compositions of pyrrhotite and CFSL run products from silica tube experiments 91
Table 3-8 Run conditions of hydrothermal experiments 93
Table 3-9 Compositions of glass run products from hydrothermal experiments..... 100
Table 3-10 Compositions of pyrrhotite and CFSL run products from hydrothermal experiments 106
Table 3-11 Mole fractions and activities of Au and Cu in recovered metal alloy 111
Table 3-12 Overall partition coefficients from this study..... 119

List of Figures

Chapter 1

Figure 1-1 log fO_2 and eruption temperature from sulfide-containing volcanic rocks . 5
Figure 1-2 Schematics and photos of laboratory equipment 11
Figure 1-3 Kanthal heating wire failures 12

Chapter 2

Figure 2-1 Design of the sealed evacuated silica tubes used in this study. 26
Figure 2-2 Calculated sulfur fugacity and wt % Cu 34
Figure 2-3 The effect of Cu in pyrrhotite on calculated fS_2 from fO_2..... 38

Chapter 3

Figure 3-1 Concentrations of Cu from the NAVDAT database 50
Figure 3-2 Concentrations of Cu from arc sections and dikes..... 54
Figure 3-3 Schematic phase diagram of the system Cu–Fe–S–O for 1000°C. 61
Figure 3-4 Design of the Cu–Fe–S silica tube experiments. 64
Figure 3-5 Design of the Cu–Fe–S–O silica tube experiments..... 66
Figure 3-6 Design of the hydrothermal experiments 71
Figure 3-7 Spot-welding during an experiment 74
Figure 3-8 Reversal experiment..... 76
Figure 3-9 Laboratory equipment 77
Figure 3-10 Concentrations of Au and S in the silicate melt. 104
Figure 3-11 Au concentration in pyrrhotite as a function of $fS_2^{0.25}$. 112
Figure 3-12 Au concentration in CFSL as a function of $fS_2^{0.25}$. 113
Figure 3-13 $D_i^{CFSL/pyrrhotite}$ for Cu, Mo, Ag, and Au as a function of fS_2. 117
Figure 3-14 $D_i^{CFSL/pyrrhotite}$ for Co, Mn, Ti, V, and Zn as a function of fS_2. 118
Figure 3-15 Schematic diagram of a section of arc crust..... 124
Figure 3-16 Modeling partial melting in the presence of sulfides 128
Figure 3-17 Schematic diagram of the system Q–Cu–$Fe_{1-x}S$. 136
Figure 3-18 Modeling fractional crystallization with loss of sulfides 139

Chapter 1: Introduction

Porphyry copper deposits are defined as large volumes (10 to 100 km^3) of partially metal-bearing, hydrothermally altered rocks centered on shallow (~1 to 6 km), intermediate to felsic igneous intrusions (Sillitoe, 2010). They may constitute part of a larger ore system that can contain skarn, epithermal, vein, or related ore bodies. Copper is typically the principal ore metal, but porphyry deposits may contain significant quantities of Zn, Mo, Ag, Sn, Au, Pb, and Bi. These deposits are important sources of the world's Cu, Mo, Au, and other metals. Porphyry deposits are associated with continental and island arcs and are a product of magmatic hydrothermal activity. They are distributed unevenly across arcs and exhibit varying metal ratios and concentrations (Sinclair 2007, Sillitoe 2010). One goal of economic geology is to better understand processes that influence the character and distribution of these deposits to aid in exploration.

The genesis of porphyry deposits is strongly influenced by processes operating during the early stages of magmatic evolution in arc systems, including subduction and magma generation in the upper mantle and lower crust. Sulfide minerals are a common and important reservoir for chalcophile elements in magmatic systems. Chalcophile ore metals may be retained in sulfides in magma source regions, or lost to early formed crystals left behind at deeper levels in the upper mantle or lower to mid crust (e.g., Lynton et al. 1993, Jugo et al. 1999, Simon et al. 2008, Bell et al. 2009). Understanding how chalcophile elements behave during this crucial stage will allow us to better constrain porphyry ore deposit formation.

Here, I present the results of experiments that I designed and performed on equipment that I designed and built as part of the Laboratory for Mineral Deposits Research (LMDR). The experiments provide important details on geologically relevant sulfide phase assemblages and the partitioning of metals between sulfide and silicate melt within a poorly-studied range of magmatic conditions. Experiments were performed at 1000°C, with an andesitic melt co-saturated with pyrrhotite and a Cu–Fe sulfide liquid (CFSL).

1.1 Porphyry deposits

Porphyry deposits are associated with felsic-to-intermediate, moderately-to-highly oxidized intrusive igneous rocks (fO_2 ~ Ni–NiO and higher) at sites of active or past subduction (Sinclair 2007, Sillitoe 2010). Ore metal-bearing sulfides are present either in a network of fracture-controlled stockwork veinlets that are commonly quartz-bearing or as disseminated grains in the adjacent altered rock volume (Berger et al. 2008). Sulfide minerals present in the deposits include: pyrite (FeS_2), pyrrhotite ($Fe_{1-x}S$–where x refers to the presence of vacancies in the structure), chalcopyrite ($CuFeS_2$), bornite (Cu_5FeS_4), chalcosite (CuS_2), molybdenite (MoS_2) and acanthite (Ag_2S). Mineralogical, petrographic, isotopic and fluid inclusion evidence suggests that the alteration and mineralization that constitutes typical porphyry-type ore deposits is magmatic–hydrothermal in origin (Hedenquist and Lowenstern 1994, Hedenquist et al. 1998, Redmond et al. 2004). The prevailing model for the origin of these deposits involves the late-stage exsolution of metal-bearing magmatic volatile phases from shallow magmas. These volatile phases

evolve into hydrothermal ore fluids (Holland 1972, Candela and Holland 1986). The metals in the magma that ultimately partition from the melt into the evolving volatile phases may have been derived from the mantle, from the melting of previous mantle-derived igneous rocks, or from the melting or incorporation of other crustal components.

Porphyry deposits are classified by the metals that can be removed economically from the deposit, and include porphyry Cu, Cu–Au, Cu–Mo, Cu–Au–Ag, Au, Au–Ag, and many other variants. Further, there are groups of characteristic deposit types. Broadly, these can be divided by the economically dominant element recovered, such as porphyry Cu, porphyry Mo, and porphyry Au deposits. The description of a given deposit may change over time as a result of changing economic conditions.

Although porphyry deposits worldwide tend to occur in the same setting (arcs, usually continental arcs), the chemistry of the deposits (ores and rocks) are extremely diverse. This diversity may be related to any number of factors, including but not limited to, variations in source rock depth and composition, initial metal concentrations, depth and temperature of the host at emplacement, depth of volatile saturation and the composition of the volatile phase, sulfur and oxygen fugacity, and host rock composition, among others. One method to evaluate these effects is to perform experiments at known and variable pressure and temperature conditions to study the distribution of metals among the phases (i.e., partition coefficients). Although all phases incorporate metals into their structure (often at concentrations not detected by most analytical instruments), sulfide minerals such as pyrrhotite and

chalcopyrite, and sulfide liquids, concentrate many ore metals. If sulfide phases are separated from the magma, either because they were left behind in the source region or separated from the magma during fractional crystallization, then differences among partition coefficients will cause metals to be lost to a greater or lesser extent. The behavior of sulfide minerals during magmatic evolution is therefore key to explaining some of the diversity seen in deposits. Furthermore, greater loss of metals in this manner may reduce the likelihood that any porphyry mineralization will become an economically viable source of ore metals.

1.2 Sulfides in subduction zones

Sulfides, including copper-rich sulfides, are common in oxidized intrusive and extrusive igneous rocks in subduction-arc complexes (figure 1.1). These sulfides include pyrrhotite (*po*) and a Fe–S–O liquid (*FSOL*). Copper-rich sulfides such as a high-temperature form of chalcopyrite commonly referred to as intermediate solid solution (*iss*), bornite, and a quenched Cu–Fe–S liquid (CFSL) are also present in intrusions associated with some porphyry Cu deposits (Core et al. 2006).

The sulfide phase(s) stable in magma are controlled by the temperature, the sulfur and oxygen fugacity, and the concentration of copper and sulfur in the silicate melt. Low-temperature felsic melts (e.g., rhyolitic) will generally be saturated by crystalline sulfides, while the higher temperatures characteristic of mafic (e.g., basaltic) melts will favor liquid sulfides (Kullerud 1968, Chang et al. 1989). In the range of temperatures characteristic of intermediate (e.g., andesitic) melts the stable

sulfide phases may be crystalline or liquid, depending on the concentration of copper in the silicate melt.

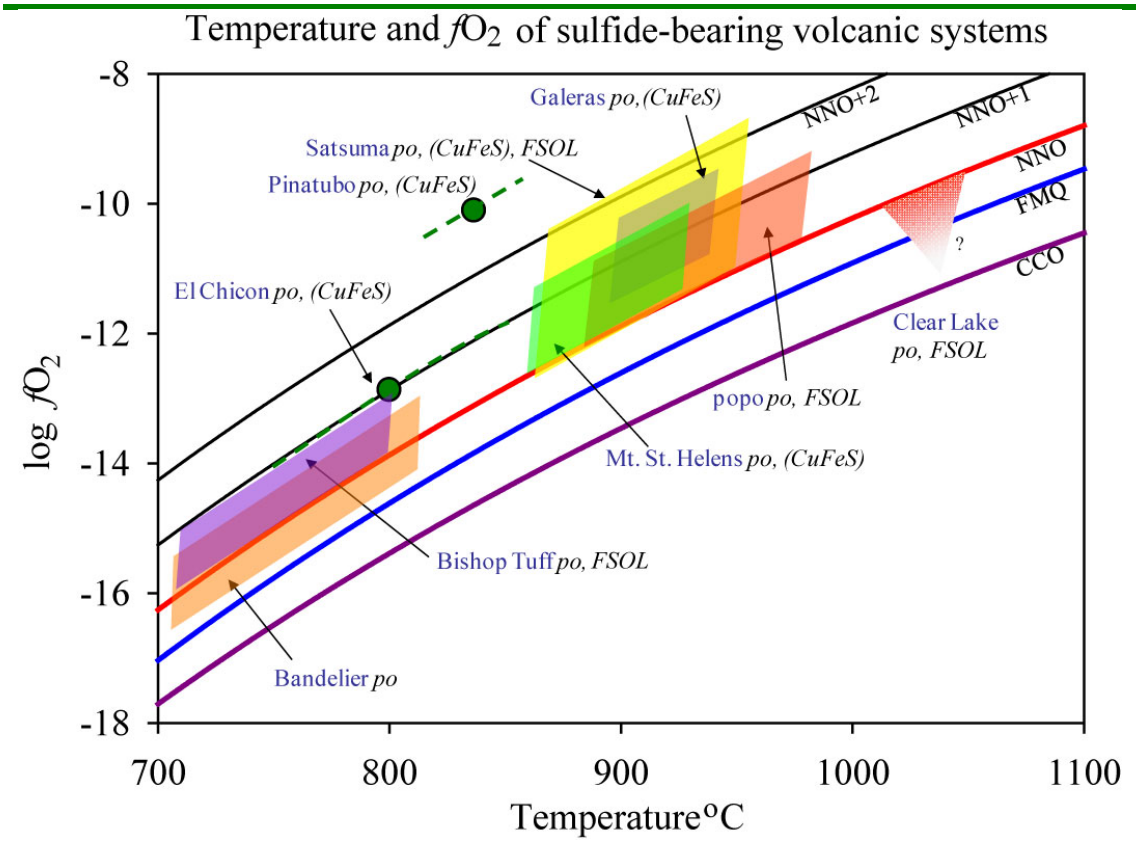

Figure 1-1 log fO_2 and eruption temperature from sulfide-bearing volcanic rocks
In this diagram, CuFeS indicates the presence of either intermediate solid solution or bornite, and FSOL indicates the presence of an immiscible liquid consisting of Fe, S, and O. The cobalt–cobalt oxide (CCO), fayalite–magnetite–quartz (FMQ), and nickel–nickel oxide (NNO) fugacity buffers, as well as the positions of NNO+1 and NNO+2, are plotted for comparison. Data are calculated for a model total pressure of 0.1 MPa. Data from: Stimac et al. (1996), Larocque et al. (1998, 2000), Stimac and Hickmott (1994), Blundy et al. (2006), Ueda and Itaya (1981), Witter et al. (2005), Hildreth and Wilson (2007), Warshaw and Smith (1988), Luhr et al. (1984), Rutherford and Devine (1991), and Calvache and Williams (1997).

1.3 Partition coefficients

The hypothesis that sulfide crystallization from magma can affect the probability of porphyry ore formation is based on a consideration of partition coefficients (Nernst-type $D_i^{sulfdie/siliate-melt}$) from field and experimental studies. These studies have repeatedly shown that sulfides concentrate a significant portion of the bulk chalcophile-metal content of magmas even though sulfides are only a minor component of the hypersolidus assemblage (Table 1-1). When metals are concentrated into an accessory phase, the removal or addition of that phase can substantially reduce the total mass of an ore metal in the magma. These phases are therefore key to understanding the genesis of porphyry deposits. Partition coefficients in Table 1-1 reveal order-of-magnitude differences among sulfide phases for individual elements, or groups of similar elements. Given the magnitude of these differences, the type (composition) of magmatic sulfide may be as important as the amount of sulfide separating from the magma when estimating the effect on the overall metal budget.

Table 1-1 Partition coefficients (Cu, Mo, Ag, and Au) from the literature

		Partition Coefficient	Source
Cu	$D_{Cu}^{po/melt}$	500±200	Lynton (1993)
		~499–502	Stimac and Hickmott (1996)
		2600±300	Jugo et al. (1999)
		174±25	Simon et al. (2008)
	$D_{Cu}^{FSOL/melt}$	>200	Simon et al. (2008)
Mo	$D_{Mo}^{po/melt}$	161	Stimac and Hickmott (1996)
		35±3	Mengason et al. (2011)
	$D_{Mo}^{FSOL/melt}$	90±11	Mengason et al. (2011)
Ag	$D_{Ag}^{po/melt}$	58±8	Simon et al. (2008)
	$D_{Ag}^{FSOL/melt}$	120±20	Simon et al. (2008)
Au	$D_{Au}^{po/melt}$	140±40	Jugo et al. (1999)
		150±83	Yang et al. (2006)
		120±50	Simon et al. (2008)
	$D_{Au}^{FSOL/melt}$	300±100	Simon et al. (2008)
	$D_{Au}^{iss/melt}$	5700±2200	Jugo et al. (1999)
		948±269	Yang et al. (2006)

Based on evidence from previous experimental studies, gold and similar elements may partition strongly into copper-rich sulfide liquids relative to other sulfide phases, or relative to the silicate melt. Consider fractionation of gold between iss and pyrrhotite. Jugo et al. (1999) report that $D_{Au}^{iss/melt}$ is greater than $D_{Au}^{pyrrhotite/melt}$. This demonstrates that gold partitions more strongly into Cu-rich than Fe-rich sulfide minerals. A similar effect has been reported between sulfide liquids and sulfide minerals. Simon et al. (2008) report that $D_{i}^{FSOL/melt}$ is greater than $D_{i}^{pyrrhotite/melt}$ for Cu, Ag, and Au, and Mengason et al. (2011) report that $D_{Mo}^{FSOL/melt}$ is greater than $D_{Mo}^{pyrrhotite/melt}$. Therefore, it is reasonable to suspect that Mo, Ag, and Au may strongly

partition into a copper-rich sulfide liquid relative to copper-poor sulfides. I examine this hypothesis regarding the partitioning behavior of metals with respect to a copper-rich sulfide liquid, in comparison with a sulfide mineral (pyrrhotite), to evaluate their relative influences on the likelihood of porphyry deposit formation.

1.4 Goals

There were three key goals for the experiments performed in this research.

1.) Investigate the conditions necessary for the saturation of an andesitic melt with respect to pyrrhotite only, pyrrhotite + CFSL, and CFSL only as a function of the concentration of copper in the melt.

2.) Calculate partition coefficients for Cu, Mo, Ag, and Au among the sulfides and silicate melt in the experiments.

3.) Use the data from 1 and 2 to evaluate the effect of sulfide separation from the silicate melt on relative concentrations of metals in the melt, the proportion of the total metal lost, and compare how these differ when pyrrhotite only, pyrrhotite + CFSL, or CFSL only is forming and being removed from the system.

1.5 Lab development, equipment, and methods

Part of the work necessary to perform these experiments involved the design and construction of new equipment, the development of new methods, and the incorporation of existing methods into procedures used for this study. Advances in the alloys used in pressure vessels have, in recent years, allowed cold-seal techniques

to be applied to higher pressure and temperature regimes that had previously been accessible. Experiments can now be run in titanium–zirconium–molybdenum (TZM) and newer molybdenum–hafnium-carbide (MHC) metal alloy pressure vessels at temperatures in excess of 1000°C and pressures greater than 100 MPa. However, pressure vessels constructed of these alloys must be isolated from the laboratory atmosphere to prevent oxidation and failure at high temperatures. These vessels therefore require a special design and additional equipment not routinely available in experimental laboratories.

Temperature also influences other aspects of the design. Working at 1000°C, as opposed to 800°C or 900°C, provides more time for the system to attempt to equilibrate to lower temperatures during cooling at the end of the experiment, overwriting the phase assemblage and distribution of metals among the phases achieved at run temperature. We therefore designed a rapid quench system wherein the capsule was physically moved on a scale of one second from the heated zone of the vessel (1000°C in these experiments) to a water-cooled zone maintained near room temperature (~15°C). However, the cooling water is a sink for heat in the vessel that can set up a large gradient in temperature across the capsule and this needed to be evaluated and overcome. In addition, heating the total mass of metal in a short time requires a furnace that can produce a large number of Joules per second. To address these challenges, I, along with Dr. Zoltan Zajacz, Brian Tattich, and the principal investigators of the Laboratory for Mineral Deposits Research (LMDR), Dr. Phil Piccoli and Dr. Phil Candela, developed and submitted a proposal to the National

Science Foundation to construct new equipment for the lab. This proposal was funded as EAR 0842205.

As part of the grant application I worked to design and specify details for the construction of a new set of furnaces. The plans included the physical structure of the frame, the mounting for the furnaces, and a method for quenching the experiment without exposing the user to the pressure vessel. I also investigated and specified the type of insulating ceramics to be used in the furnace construction and designed the wiring system, the electronics, and the data gathering and recording system.

Once the grant was funded, I ordered parts and worked to construct new lab equipment, including the majority of the new MHC bench, the furnaces and electronics, and including programming the data recording equipment (Figure 1-2). As a group we built and tested the high-pressure gas system, wired the electronics and sensor system, and constructed the furnace cores. Ultimately, part of the research undertaken in this study related to the development of a new hydrothermal facility and the equipment and methods associated with it.

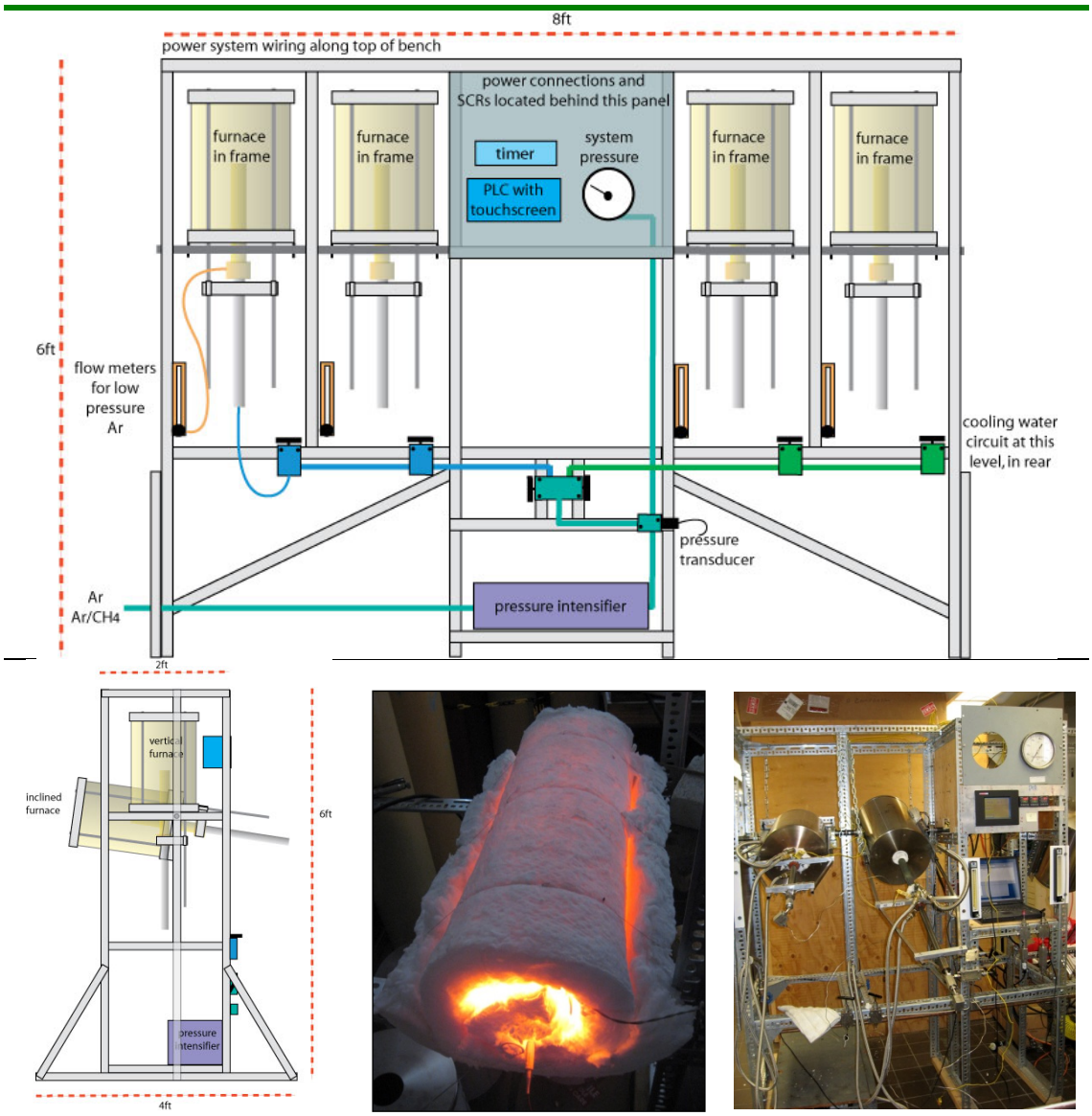

Figure 1-2 Schematics and photos of laboratory equipment

Top and Left: Schematics for a furnace system used to perform hydrothermal experiments at 1000ºC and 150 MPa. Bottom middle: Photo of a temporary furnace constructed to fire the Alundum ceramic insulation at 1300ºC on a new furnace element. Bottom right: Left side of new frame assembly for experimental equipment built with funds from the National Science Foundation equipment grant. All but two of the hydrothermal experiments detailed in this dissertation were performed using this equipment. Two furnaces built in-house are shown, including: the MHC pressure vessel assemblies mounted on pivots (to facilitate sliding and tilting for quenching), the high-pressure gas system, flushing gas system, temperature control system, water cooling system, and computer recording of temperature and pressure sensors.

Part of the work I needed to do in order to complete the research for this dissertation involved the construction of new coil-type furnaces. Early experiments

in both sealed evacuated silica tubes and titanium–zirconium–molybdenum alloy (TZM) pressure vessels suffered failures due to the breakdown of heating elements in the available coil-type furnaces. Extensive experimentation and investigation ultimately identified the common point of. The problem was traced to erosion of the wire by chemical interaction with elements in the Sauereisen high-temperature cement previously used. Figure 1-3 includes images of a sample of new Kanthal wire and a sample taken proximate to a point of failure. Near the point of failure the wire has a smaller cross-section than the unused wire. Under electrical load the smaller cross-section resulted in higher resistance and therefore higher temperature at that point in the wire. At the point of failure that higher temperature in turn increased the resistance of the remaining thickness of wire, which in turn raised the temperature in a runaway event that resulted the wire melting. The solution to this problem is to use Kanthal wire (which forms Al_2O_3 on its surface when heated in air) surrounded by Alundum (Al_2O_3) that is fused at 1300°C into a ceramic insulator. New furnaces in the lab use this insulated wire. The common chemistry between the wire surface and the ceramic prevents degradation of the wire and allows thousands of hours worth of experiments to be run.

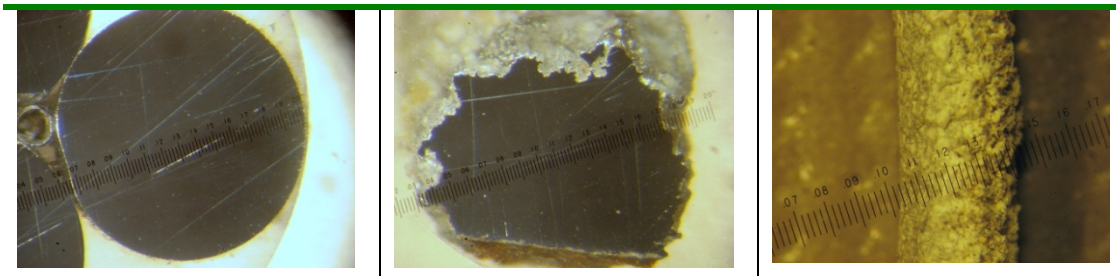

Figure 1-3 Kanthal heating wire failures
Left: Photomicrograph a cross section of new Kanthal wire. Middle: a cross section from near a point of failure showing the loss of material from the edges. Right: the outside of the wire near a point of failure showing eroded surface.

Several improvements were made to the laboratory equipment as part of this upgrade. The previous design for the pressure vessel was lengthened to allow for more heating between the location of the capsule and the water-cooled fixture in order to reduce the thermal gradient over the length of the capsule. In addition to upgrading the design of the wire-coil furnaces, a separate design for a furnace based on a silicon-carbide ceramic heating element was developed. Both furnace designs have been built and were used in experiments detailed in Chapter 3. The power system was designed to incorporate phase-angle-firing silicon-controlled rectifiers to better control the temperature in the furnaces as well as to prolong furnace lifetime. Due to this change, the temperature in the pressure vessel at the location of the experiment becomes stable to within less than 1°C during an experiment. And digital pressure transducers and thermocouples were built into the new furnace control system to allow temperature and pressure to be recorded throughout an experiment.

1.6 Pyrrhotite composition and sulfur fugacity (fS_2)

In Chapter 2, a scientific communication published in the journal *Economic Geology* as "An evaluation of the effect of copper on the estimation of sulfur fugacity (fS_2) from pyrrhotite composition" is presented in which a method is demonstrated that allows the concentration of copper to be included in calculations for determining sulfur fugacity from the composition of pyrrhotite. Sulfur fugacity, along with oxygen fugacity, are master intensive variables that are used in geology to characterize the thermodynamic state of a system. Matching fugacities between experiments and natural systems is necessary (though not sufficient) to determine the

relevance of experiments to understanding the petrogenic processes that occur in magmas and affect the composition of the melt, the volatile phase, and the formation of rocks. Toulmin and Barton (1964) quantified the relationship between the composition of pyrrhotite and sulfur fugacity, relating log fS_2 to the proportion of FeS in pyrrhotite within the system FeS–S_2 that is calculated as 2[XFe/(XFe+XS)] where X is the mole fraction in pyrrhotite. Their equation is useful in volcanology, analysis of sulfide inclusions, analysis of experimental run products, and other fields where pyrrhotite may retain the composition it attained at equilibrium with other sulfur-bearing phases. However, their calculation excludes the effect of copper. The concentration of copper in pyrrhotite may be several weight percent in volcanic rocks (Luhr et al. 1984), sulfide inclusions (Hattori 1996), and in experimental run products (Jugo et al. 1999), and must be factored into the calculation.

A method was needed that would allow calculation of sulfur fugacity from the concentration of copper-rich pyrrhotite that would be consistent with sulfur fugacity calculated from copper-free pyrrhotite in order to prevent the introduction of systematic errors when comparing experiments with different activities of copper. In response, a set of simple experiments was developed in which copper-free pyrrhotite and pyrrhotite with concentrations of ~2, 4, and 6 wt % Cu were allowed to equilibrate with the same sulfur volatile phase, and therefore the same sulfur fugacity. Multiple methods for incorporating the concentration of copper in copper-rich pyrrhotite into the equation of Toulmin and Barton (1964) were evaluated and one was identified that yielded the same sulfur fugacity as that calculated from copper-free pyrrhotite. Compared with other methods of incorporating, or omitting, the

concentration of copper in pyrrhotite, this method prevents the introduction of a systematic error of approximately 1/4 log unit fS_2 per weight percent copper in pyrrhotite. Now, researchers can directly compare results of fS_2 estimates from experimental and natural systems that fall off the Fe–S_2 join (most pyrrhotite), on a like basis.

1.7 Experiments on sulfide solubility and partitioning

Chapter 3 is presented as a draft manuscript for submission to a peer-reviewed journal, albeit a manuscript with more details and explanations than can be included in a published paper. This work is focused on the ability of sulfide phases separated from magma to sequester metals and affect the likelihood of porphyry and related magmatic-hydrothermal deposit formation, or to affect the ratio of metals within deposits. Sulfide phases may be separated from magma when they are retained in the source region during partial melting or they may be separated during crystallization along with other cumulate phases. Specifically, the relative roles played by CFSL and pyrrhotite in the likelihood of deposit formation is investigated.

Key to this endeavor was new data from experiments on the stability of these sulfide phases as a function of temperature and the concentration of copper in the silicate melt. The new equipment and experimental techniques described in section 1.5 were developed in order to perform these experiments.

These experiments were based on simple principals of equilibrium. A relatively large amount of pyrrhotite and CFSL was placed in contact with a relatively small amount of silicate melt, which forced the silicate melt to equilibrate with both

sulfide phases. In arc magmatic systems, the silicate melt dominates over the sulfide phases, which are only accessory phases. Under those circumstances, the composition of the silicate melt will control the composition of the sulfide phase or phases that may be stable, which is the reverse of these experiments. Therefore, these data apply to (and establish the conditions of) the point where the magma changes from being saturated with pyrrhotite only, to pyrrhotite and CFSL, and then to CFSL only.

Using partition coefficients among the phases calculated from these experiments, the effect of sulfide present during partial melting and sulfide separated from the silicate melt during fractional crystallization on the concentrations of Cu, Mo, Ag, and Au in the silicate melt is evaluated. This ultimately places limits on the likelihood of porphyry and related hydrothermal ore deposit formation by these magmas.

The hydrothermal experiments were conducted at high temperatures in the presence of water. Experimental temperatures were comparable to andesitic melts, which are under-represented in the literature relating to magmatic hydrothermal deposits. While performing the experiments at high temperature in the presence of water complicated the experimental design considerably, the selected conditions better reflect natural magmatic systems than experiments conducted at lower temperatures and/or in the absence of water, which may yield different sulfide assemblages. For these reasons, the experiments were performed in cold-seal pressure vessels within noble-metal capsules at 150 MPa and 1000°C, allowing me to produce a hydrous silicic melt of andesitic composition along with sulfide phases appropriate

to that temperature. Maintaining a hydrous volatile phase is possible in this type of experiment using sealed (arc-welded) noble-metal capsules. Gold capsules are commonly used for this purpose; however, they may alloy with copper from the experiment and are very close to their melting point. Problems and solutions associated with the capsules as well as the use of metal–oxide oxygen fugacity buffers, the potential for sulfides to breach the capsules, and other experimental challenges are discussed in chapter 3.

In order to evaluate the run products from these hydrothermal experiments, a parallel series of experiments similar to those in Chapter 2 were designed and run. This allowed evaluation of the systematics of the concentrations of Au, Cu and O_2 in pyrrhotite and the CFSL in a simpler system than that of the hydrothermal experiments. The combination of the two sets of experiments produced a coherent view of the system. I present data from these experiments on the concentration of copper in the silicate melt that defines the point at which it will be co-saturated by pyrrhotite and CFSL. I also present data on relationships between gold solubility within each phase and the concentration of sulfur in the melt, or alternatively, the sulfur fugacity, and coefficients for the partitioning of Cu, Mo, Ag, and Au among pyrrhotite, CFSL, and the andesitic melt. I use these data to discuss the possibility for porphyry ore formation as a function of (1) the sulfides present in the source region of the melt and (2) the sulfides removed from the melt during fractional crystallization.

1.8 Notes

Work presented here was performed in the Laboratory for Mineral Deposits Research at the University of Maryland. Analyses were performed at the University of Maryland at the NISP Lab (Nanoscale Imaging and Spectroscopy Properties Lab) and the Plasma Mass Spectrometry Laboratory. All figures and tables in this dissertation were created by Michael Mengason, all experiments were designed, loaded, and executed by Michael Mengason, and all analyses of run products were performed by Michael Mengason.

Chapter 2: An evaluation of the effect of copper on the estimation of sulfur fugacity (fS_2) from pyrrhotite composition

2.1 Abstract

Pyrrhotite is commonly used to estimate the fugacity of sulfur in natural and experimental systems; however, in some instances, high-temperature pyrrhotite can incorporate copper to such an extent as to raise questions concerning the accuracy of the sulfur fugacities calculated on the basis of their composition. The equation of Toulmin and Barton (1964), which is commonly used to determine sulfur fugacity from the composition of binary pyrrhotite ($Fe_{1-x}S$) solid solutions, can be modified to account for the presence of other phase components. Three methods of incorporating the concentration of copper in the equation of Toulmin and Barton (1964) were evaluated in light of data from experiments performed at 1000°C, which yielded run product pyrrhotite with 0.028 (±0.005, 1σ) to 5.75 (±0.06) weight percent copper. Mixtures of synthetic pyrrhotite and bornite were heated in sealed evacuated silica tubes that were internally divided into separate chambers by silica rods. As a result, pyrrhotite grains with a range of copper concentrations, as well as copper-free 'reference' pyrrhotite, were equilibrated at a common sulfur fugacity. The discrepancy between sulfur fugacity calculated from 'reference' pyrrhotite and copper-rich pyrrhotite, based on EPMA analyses, indicated a source of error and potential for disagreement between published accounts when different methods are used to address the presence of copper.

The term N_{FeS} in the equation of Toulmin and Barton (1964), calculated as $X_{FeS}^{pyrrhotite}$ in the system FeS–S_2, was replaced by terms that incorporated the effect of copper. Method 1: $N = 2\left(\frac{nFe}{nFe+nS}\right)$— copper was ignored; $X_{FeS}^{pyrrhotite}$. Method 2: $N = 2\left(\frac{nFe+nCu}{nFe+1.5nCu+nS}\right)$—copper was treated as $CuS_{0.5}$; $X_{FeS}^{pyrrhotite} + X_{CuS_{0.5}}^{pyrrhotite}$. Method 3: $N = 2\left(\frac{nFe+nCu}{nFe+nCu+nS}\right)$—copper was treated as CuS; $X_{FeS}^{pyrrhotite} + X_{CuS}^{pyrrhotite}$. Method 1 overestimated log fS_2 (bar) by 0.25 (±0.08, 1σ) per wt % copper. Method 2 resulted in consistent fugacity estimates regardless of the concentration of copper in pyrrhotite, and is the recommended method. Method 3 underestimated log fS_2 by 0.3 (±0.2) per wt % copper. These systematic errors are propagated into the calculation of oxygen fugacity based on magnetite-pyrrhotite coexistence resulting in a correction factor of ~¼ log fO_2 per wt % copper by the use of either method 1 or 3 in determining sulfur fugacity.

2.2 Introduction

Pyrrhotite—a common iron-sulfide accessory phase in volcanic and plutonic rocks, metamorphic rocks, meteorites, and experimental run-products—can be used to calculate sulfur fugacity. Samples of pyrrhotite ($Fe_{1-x}S$ – where x denotes vacant octahedral sites) exhibit solid solution between stoichiometric troilite (FeS), and an Fe-deficient (sulfur excess) end member (Fleet 2006). The relationship between the iron to sulfur ratio of pyrrhotite and sulfur fugacity was quantified by Toulmin and Barton (1964) through a series of experiments. This relationship has become a useful tool by which the reactivity of sulfur in systems such as, for example, arc volcanic eruptions (Luhr et al. 1984), can be estimated. However, as shown by Kullerud

(1968), pyrrhotite may also form solid solutions with more copper-rich compositions that were not included in the investigation of Toulmin and Barton (1964). Without a reliable way to incorporate the concentration of copper in pyrrhotites into the equation of Toulmin and Barton (1964) there is the potential for error when calculating sulfur fugacity.

To evaluate whether or not the concentration of copper in pyrrhotite introduces an error in these calculations, a common sulfur fugacity was imposed in this study on copper-rich and copper-free pyrrhotites heated in sealed evacuated silica tubes. Ideally, sulfur fugacities calculated from analyses of pyrrhotite grains that were equilibrated together should be the same. If the presence of copper in pyrrhotite is a source of error in this calculation, it would result in a discrepancy between calculated sulfur fugacities that is directly related to the difference in copper concentrations. Pyrrhotite run-products were produced in these experiments with copper concentrations ranging from 0.028 (±0.005, 1σ) to 5.75 (±0.06) wt % and used to test for this potential error. Methods to minimize any error were also tested against the dataset. Our work has been undertaken to allow consistent calculation of sulfur fugacity, and to promote continuity among published accounts of sulfur fugacity (e.g. Luhr et al. 1984, Jugo et al. 1999).

Sulfur fugacity (log bar) is related to pyrrhotite composition by the equation

$$\log fS_2 = (70.03 - 85.83N)(1000/T - 1) + 39.30\sqrt{1 - 0.9981N} - 11.91$$

where temperature is in Kelvin, and N is equal to $X_{FeS}^{pyrrhotite}$ in the system FeS–S_2 ($N = 2\left(\frac{nFe}{nFe+nS}\right)$ where n is the number of moles) from Toulmin and Barton (1964). This relationship is based on experiments performed in sealed evacuated silica tubes

containing synthesized electrum and pyrrhotite. Toulmin and Barton (1964) used the electrum tarnish method to bracket the sulfur fugacity of the gas system in a given experiment based on inspection of the electrum surface, and used XRD to determine the composition of the pyrrhotite starting material. This work resulted in a simple relationship that has been used to determine sulfur fugacity for over 40 years.

The maximum bias in estimates due to the concentration of copper in pyrrhotite will be from analysis of pyrrhotite with the maximum concentration of copper. The maximum concentration of copper in pyrrhotite is approximately 7 wt % copper, and occurs in the temperature range of 900°C to 1000°C (Kullerud, 1968). Pyrrhotite formed at lower temperatures will have lower concentrations of copper, and consequently will be less susceptible to this bias. Biased sulfur fugacity estimates would seem to be most likely when considering pyrrhotite from igneous or high-grade metamorphic rocks.

On cooling pyrrhotite may either exsolve a copper-rich phase such as chalcopyrite ($CuFeS_2$), or the ratio of chalcopyrite coexisting with pyrrhotite may increase. Many samples of pyrrhotite may have possessed a higher concentration of copper at higher temperatures. In a survey of terrestrial pyrrhotite from 82 American, European, and African mineral deposits, Arnold (1967) identified no pyrrhotite with greater than 0.4 (±0.2) wt % copper, but chalcopyrite was present with pyrrhotite (which was shown to have low temperature structure) in 69 of the 82 cases. Samples of pyrrhotite which have retained their higher-temperature copper concentration during cooling, and pyrrhotite where exsolved copper-rich phases are re-integrated

for the calculation, are the cases where incorrectly incorporating copper in sulfur fugacity calculations will most likely lead to unnecessary error.

In some volcanic and experimental systems, the rapid temperature drop may preserve high copper concentrations. Luhr et al. (1984) reported pyrrhotite with 2.95 wt % copper in trachyandesite from El Chichón. Hattori (1996) reported pyrrhotite with 2.53 wt % copper in basalt, and with 6.19 wt % copper in andesite, from Mt. Pinatubo. Examples of high copper concentrations in pyrrhotite run products from experiments include 2.2 wt % from Simon et al. (2008), 5.41% from Bell et al. (2009), and 6.9 wt % from Jugo et al. (1999). The isolation of pyrrhotite in sulfide inclusions may also prevent the loss of copper.

The same processes that preserve concentrations of copper from magmatic conditions may also prevent re-equilibration with higher or lower sulfur fugacities. Pyrrhotite from these systems provides information on the activity of copper as well as the fugacity of sulfur in pre-eruptive magmas, or at conditions that prevail during high-temperature experimentation. The sulfur fugacity of magmas has been of interest to economic geologists due to the relationship between sulfur fugacity and the solubility of PGE's (Bell et al. 2009, Sattari et al. 2002) and copper (Gaetani and Grove 1997, Holzheid and Lodders 2001, Ripley et al. 2002) in silicate melts, and the influence that sulfur fugacity may exert on sulfide–silicate melt partition coefficients for chalcophile elements (Jugo et al. 1999, Simon et al. 2008). The specific impetus for this study is the need to evaluate sulfur fugacities and partition coefficients for magmas which are the predecessors of intrusions related to magmatic-hydrothermal ore deposits.

Pyrrhotite is the most common sulfide in intermediate to felsic arc magmas associated with magmatic-hydrothermal deposits. Arc magmas tend to be highly sulfidized relative to the fayalite–magnetite–quartz–pyrrhotite (FMQP) sulfur fugacity buffer. The value of FMQP used here has been calculated from the equation of Whitney (1984). Examples include: 3.2 log fS_2 units above FMQP (FMQP +3.2) at El Chichón (Luhr et al., 1984), +1.9 at Mt. St. Helens (Hopson and Melson 1990), +3.9 at Julcani (Drexler 1984), and +2.4±0.6 at Satsuma Iwo-Jima (Ueda and Itaya 1981). Wallace (2005) has pointed out the discrepancy between estimates of globally subducted sulfur, ~ 1.8 x 10^{13} g/year (Wallace 2005), and globally emitted sulfur, ~ 1.1 x 10^{13} g/year (Hilton et al. 2002). These data suggest that at least some portion of the sulfur may precipitate from arc magmas within the crustal reservoir. Pyrrhotite and other sulfides have been identified as sinks in magmatic systems for copper, silver, gold, and molybdenum. These elements have been shown to partition preferentially into Fe-sulfides (pyrrhotite—Lynton et al. 1993), Cu–Fe–sulfides (chalcopyrite–intermediate solid solution, $CuFeS_2$—Jugo et al. 1999), and Fe–S–O liquids (Mengason 2007, Simon et al. 2008) relative to felsic silicate melts.

Considering (1) the potential effect of sulfur fugacity on sulfide-melt partition coefficients, (2) the generally high sulfur fugacity in the parental arc magmas of porphyry deposits, (3) the deposition of sulfides in the crust, and (4) preferential partitioning of metals often mined in porphyry deposits into sulfides, suggests that a large percentage of the initial metal budget of arc magmas is lost through sulfide deposition during crystal fractionation. Conversely, the partial melting of a portion of crust that contains sulfide deposits may elevate the budgets of these and other metals

in some magmas. Given the high copper concentrations in pyrrhotite and other sulfide phases appropriate to these systems, a reliable method for estimating sulfur fugacity is required.

2.3 Experimental methods

Experiments were designed around the simple idea of equilibrating reference pyrrhotite and pyrrhotites ranging in copper concentration. The pyrrhotite samples in these experiments were isolated in chambers that prevented the exchange of copper and iron by the use of a physical barrier, because copper and iron are not volatile at these conditions, but allowed the free exchange of sulfurous gas creating a common gas phase. Given that the pyrrhotites in each chamber were equilibrated with a common gas phase, they should record the same sulfur fugacity, regardless of copper concentration.

Experiments consisted of sealed, evacuated silica tubes (3mm ID x 7mm OD), divided into chambers by 3 mm diameter silica rods, with the chambers initially containing either pyrrhotite, or a mixture of pyrrhotite and bornite (Fig. 2-1). Pyrrhotite and bornite were synthesized for these experiments from elemental copper, iron, and sulfur as appropriate (Table 2-1). Three or more of these silica capsules were bound together and placed into a vertical tube-style furnace that allowed for a rapid water-bath quench.

Silica capsules for the experiments were designed and constructed with four chambers (Fig. 2-1 and Table 2-1). This included a reference chamber at the bottom, with three other chambers stacked above. Capsule 84b contained an additional chamber in which a small chip of platinum was placed to lower the intrinsic sulfur

fugacity of the phase assemblage. Due to a thick rind of PtS on the chip, pyrrhotite in the experiment was likely not in equilibrium with the platinum metal. Capsule 84c also contained an additional chamber in which powdered iron metal was added to lower the sulfur fugacity of the experiment.

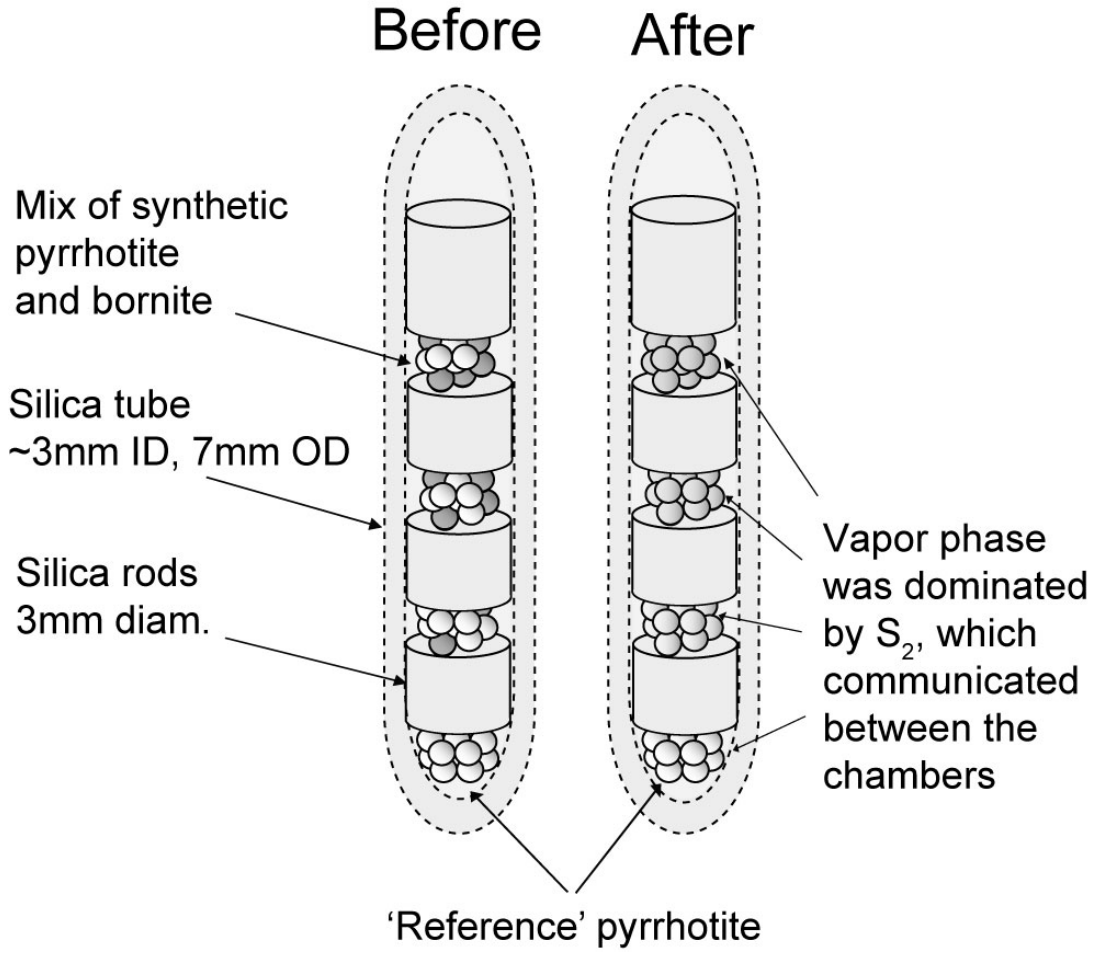

Figure 2-1 Design of the sealed evacuated silica tubes used in this study.
Silica rods were used to divide the tubes into separate chambers. Synthetic pyrrhotite was placed in the bottom chamber to serve as a copper-free reference indicator of sulfur fugacity. Mixtures of synthetic pyrrhotite and bornite were placed in the remaining chambers to form pyrrhotites ranging in copper concentration. Sulfur gas could move among the chambers unifying the sulfur fugacity of the experiment, but copper and iron could not because of their negligibly low volatility.

These experiments, run simultaneously in one furnace, yielded 3 chambers of reference pyrrhotites and 9 chambers of pyrrhotites with copper concentrations ranging from 2.29 to 5.75 wt %.

Capsules were heated to 1050°C for several hours, then the temperature was lowered and the capsules were held at 1000°C for at least 5 days. The temperature varied by less than 2°C, and the total temperature difference over the length of a capsule was also on the order of 2°C. Experiments and calculations were performed at 1000°C because of the relevance of this temperature to the intermediate magmas we are addressing. Although the temperature is higher than the temperatures of the original experiments of Toulmin and Barton (1964), there is no reason to question the validity of their calibration under our experimental conditions, given the linearity of their data as a function of 1/T. To terminate the experiment, capsules were drop-quenched in a water bath. Following quench, the chambers were emptied separately, and the contents analyzed.

Table 2-1 Composition of experimental charges

Experiment	Chamber	pyrrhotite (g)	bornite (g)
84a	Ref	0.00394	na
	1	0.00380	0.00012
	2	0.00315	0.00020
	3	0.00332	0.00030
84b*	Ref	0.00358	na
	1	0.00343	0.00014
	2	0.00302	0.00022
	3	0.00358	0.00038
84c*	Ref	0.00332	na
	1	0.00338	0.00013
	2	0.00324	0.00022
	3	0.00385	0.00042

Composition of synthetic starting materials (EMPA)

Starting material		Cu		Fe		S	
	n	wt %	± *1σ*	wt %	± *1σ*	wt %	± *1σ*
pyrrhotite	*4*	0.01	*0.01*	60.72	*0.05*	39.5	*0.3*
bornite	*6*	58	*2*	11.9	*0.4*	30	*1*

na = none added. Analysis of starting materials by WDS. n = number of samples.

* In order to lower the intrinsic fS_2 of the experiment, 84b contained a small amount of metallic Pt, and 84c contained a small amount of metallic Fe, in additional chambers.

2.4 Analytical methods

Electron probe microanalysis (EPMA) was performed using a JEOL JXA-8900 Superprobe. Prior to analysis by EPMA, run products were mounted in epoxy, polished, and images were collected by using reflected-light microscopy. Wavelength dispersive spectrometry (WDS) analysis of the run products was performed using a defocused 30μm beam, with an accelerating voltage of 20kV, and a cup current of 50nA. Chalcopyrite from Inguaran, Michoacan, Mexico (USGS 107945–S) was used as the standard for copper using an LiF crystal. Pyrrhotite from Santa Eulalia, Mexico (USNM R7570) was used as the standard for iron (LiF) and sulfur (PETH). X-rays were collected for 40 seconds on peak and 20 seconds on background for copper, 25 seconds peak and 10 seconds background for iron, and 50 seconds peak and 20 seconds background for sulfur.

2.5 Results

Corrections to the equation from Toulmin and Barton (1964) were evaluated by calculating sulfur fugacity three ways. In method 1, copper was ignored and only iron and sulfur were used in the calculation. For this method, *N* from the Toulmin and Barton equation equaled the mole fraction of FeS in the system FeS–S_2: $N = \left(X_{FeS}^{pyrrhotite}\right) = 2\left(\frac{nFe}{nFe+nS}\right)$. For method 2, copper was incorporated as $CuS_{0.5}$ in the system FeS–$CuS_{0.5}$–S_2, and $N = \left(X_{FeS}^{pyrrhotite} + X_{CuS_{0.5}}^{pyrrhotite}\right) = 2\left(\frac{nFe+nCu}{nFe+1.5nCu+nS}\right)$. For method 3, copper was incorporated as CuS in the system FeS–CuS–S_2 and $N = \left(X_{FeS}^{pyrrhotite} + X_{CuS}^{pyrrhotite}\right) = 2\left(\frac{nFe+nCu}{nFe+nCu+nS}\right)$. Details on these calculations can be found in the appendix.

The concentrations of copper, iron and sulfur from analysis of run product pyrrhotites are listed in Table 2-2. Uncertainties are given as one standard deviation of the averaged analyses for each chamber. The distribution of copper in pyrrhotite is homogeneous according to our analyses. The relative standard deviation for the pyrrhotites of each chamber is less than or equal to 1% for all but one chamber, 84c, where it is 6%. Considering the starting conditions of the experiment—pyrrhotite with 0.01 wt % copper plus bornite with 58 wt % copper—the presence of a single homogenous pyrrhotite phase in the run products with greater than 5 wt % copper strongly suggests that sufficient time has elapsed for the experiment to have approached a state of equilibrium with regard to copper in pyrrhotite. Likewise, pyrrhotite in the experiment lost between 0.6 and 2.6 wt % sulfur from the starting composition, ending with all chambers having a relative standard deviation of less than 0.8%. This, again, strongly suggests that sufficient time passed for the experiment to have attained equilibrium.

Table 2-2 Run product compositions and calculated sulfur fugacities

			Cu		Fe		S		Formula	Method 1			Method 2			Method 3		
Exp	Chb	n	wt %	± 1σ	wt %	± 1σ	wt %	± 1σ	□ = vacancy	*N*	*log fS₂*	± 1σ	*N*	*log fS₂*	± 1σ	*N*	*log fS₂*	± 1σ
84a	Ref	12	0.04	*0.01*	60.9	*0.1*	38.9	*0.1*	$\square_{0.101}Cu_{<0.001}Fe_{0.899}S$	0.947	-0.3	*0.1*	0.947	-0.3	*0.1*	0.947	-0.3	*0.1*
	1	8	2.29	*0.01*	59.08	*0.08*	38.5	*0.3*	$\square_{0.089}Cu_{0.030}Fe_{0.881}S$	0.937	0.3	*0.2*	0.946	-0.2	*0.2*	0.954	-0.7	*0.2*
	2	9	3.80	*0.03*	57.4	*0.1*	37.8	*0.3*	$\square_{0.077}Cu_{0.051}Fe_{0.872}S$	0.932	0.6	*0.2*	0.947	-0.3	*0.2*	0.960	-1.2	*0.2*
	3	8	5.15	*0.04*	56.8	*0.1*	37.7	*0.2*	$\square_{0.066}Cu_{0.069}Fe_{0.865}S$	0.928	0.8	*0.2*	0.949	-0.4	*0.2*	0.966	-1.7	*0.2*
84b	Ref	12	0.04	*0.01*	61.2	*0.1*	38.5	*0.2*	$\square_{0.087}Cu_{<0.001}Fe_{0.913}S$	0.954	-0.8	*0.2*	0.955	-0.8	*0.2*	0.955	-0.8	*0.2*
	1	8	3.01	*0.02*	58.9	*0.2*	38.0	*0.2*	$\square_{0.070}Cu_{0.040}Fe_{0.890}S$	0.942	0.0	*0.2*	0.954	-0.8	*0.2*	0.964	-1.5	*0.3*
	2	8	4.19	*0.04*	57.80	*0.09*	37.7	*0.1*	$\square_{0.064}Cu_{0.056}Fe_{0.880}S$	0.936	0.4	*0.1*	0.953	-0.7	*0.1*	0.967	-1.8	*0.1*
	3	8	5.75	*0.06*	56.63	*0.07*	37.5	*0.1*	$\square_{0.056}Cu_{0.077}Fe_{0.867}S$	0.929	0.8	*0.1*	0.952	-0.7	*0.1*	0.971	-2.2	*0.1*
84c	Ref	12	0.028	*0.005*	61.5	*0.1*	38.3	*0.3*	$\square_{0.078}Cu_{<0.001}Fe_{0.922}S$	0.959	-1.2	*0.3*	0.960	-1.2	*0.3*	0.960	-1.2	*0.3*
	1	8	2.79	*0.02*	59.5	*0.1*	37.5	*0.1*	$\square_{0.051}Cu_{0.038}Fe_{0.911}S$	0.953	-0.7	*0.1*	0.964	-1.6	*0.1*	0.974	-2.4	*0.1*
	2	8	4.66	*0.05*	57.8	*0.1*	37.3	*0.2*	$\square_{0.047}Cu_{0.063}Fe_{0.890}S$	0.942	0.0	*0.2*	0.960	-1.2	*0.2*	0.976	-2.6	*0.2*
	3	8	5.2	*0.3*	57.4	*0.3*	36.9	*0.2*	$\square_{0.036}Cu_{0.071}Fe_{0.893}S$	0.944	-0.1	*0.4*	0.964	-1.6	*0.5*	0.982	-3.3	*0.6*

(Ref) indicates the reference, copper-free, pyrrhotite.

Chambers (Chb) 1,2, and 3, indicate copper-bearing pyrrhotites in a given experiment (Exp).

Number of analyses indicated by n. Vacancies (□) calculated by cation deficiency.

N is the value used with the equation of Toulmin and Barton (1969).

Sulfur fugacity has been calculated by using the three methods described. The uncertainties on copper, iron and sulfur have been propagated and given as 1σ. By design, all chambers within an experiment have the same sulfur fugacity. Calculation by methods 1 and 3 performed poorly: the calculated fugacities for copper-rich pyrrhotites deviated from the reference pyrrhotite beyond the 1σ level. Method 2 worked well, with most calculated fugacities overlapping the reference values, and this is the suggested method to follow.

2.6 Discussion

The magnitude of the systematic error introduced by the use of method 1 or 3 has been calculated, and is shown in Figure 2-2. In these cases, the calculated sulfur fugacity increasingly deviates from the reference fS_2 with increasing concentration of copper in the run product pyrrhotites. Method 1 overestimates log fS_2 by 0.25 (±0.08, 1σ) per wt % copper, and method 3 underestimates log fS_2 by 0.3 (±0.2, 1σ) per wt % copper.

The effect of this systematic error on sulfur fugacity can be seen in Table 3, which shows sulfur fugacity calculated by methods 1, 2, and 3, for pyrrhotite from volcanic rocks. Luhr et al. (1984) used a method similar to method 3 (see Table 2-3). In previous literature, other common transition metals have generally been treated as analogs of FeS: CoS, ZnS, MnS, and NiS. $CuS_{0.5}$, and by extension $AgS_{0.5}$ and $AuS_{0.5}$, may be exceptions to this rule. Although it will be rare for more than one or two cations to be present in concentrations that would significantly affect calculated

sulfur fugacity, it is suggested that the inclusion of those listed above would take the following form:

$$N = 2\left(\frac{nFe + nCo + nZn + nMn + nNi + nCu + nAg + nAu}{nFe + nCo + nZn + nMn + nNi + 1.5nCu + 1.5nAg + 1.5nAu + nS}\right).$$

Whitney (1984) calculated the equilibrium magnetite–pyrrhotite boundary in log fS_2 and log fO_2 space (Figure 2-3). This graph can be used to calculate sulfur fugacity from a known oxygen fugacity, or oxygen fugacity from a known sulfur fugacity. If oxygen fugacity can be calculated from another method such as magnetite–ilmenite (Buddington and Lindsley, 1964) or ilmenite–biotite (Ague and Brimhall 1988, Candela 1989), then the corresponding sulfur fugacity of a system known to have contained pyrrhotite can be calculated (see arrows—Figure 2-3). In log fO_2–log fS_2 space, the position of the magnetite–pyrrhotite boundary will shift in response to the presence of other cations in pyrrhotite. Whitney (1984) calculated a correction factor of $2\log[Fe/(Fe+Cu)]$ to compensate for this effect. Based on the derivation presented in that paper and the formulation of the equilibrium, our data suggest that $2\log\left[Fe/(Fe+2Cu)\right]$ may be more appropriate. Magnetite–pyrrhotite boundaries for copper-free pyrrhotite and pyrrhotite containing 2, 4, and 6 wt % copper are plotted in Figure 2-3. At 6 wt % copper, this correction is -0.26 log fS_2 for a given fO_2.

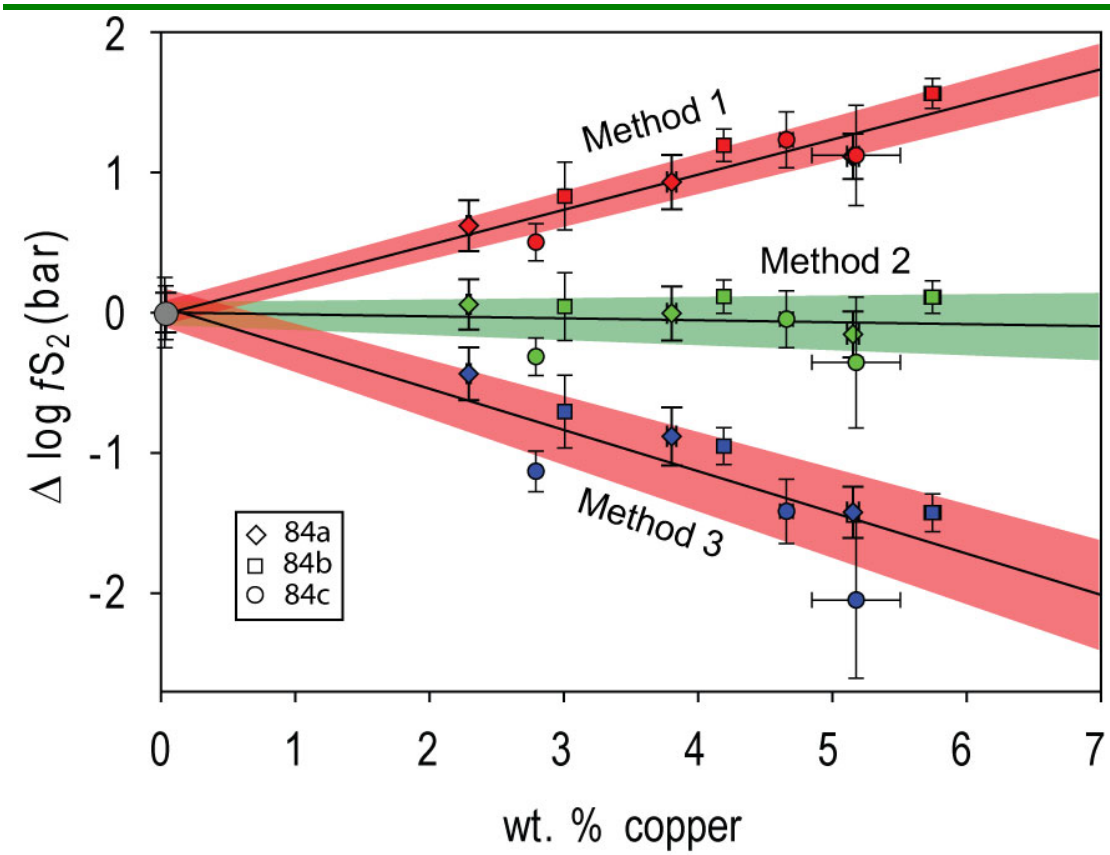

Figure 2-2 Calculated sulfur fugacity and wt % Cu
Calculated sulfur fugacity is plotted against the concentration of copper in run product pyrrhotite samples. For each experiment, sulfur fugacity estimates have been normalized to the fugacity of the reference pyrrhotite. The data from experiments 84a (diamond), b (square), and c (circle), are plotted with 1σ uncertainty on log fS_2, copper wt %, and regression fit. Top—the slope indicates that method 1 overestimates by 0.25 (±0.08, 1σ) log units fS_2 (bar) per wt % copper in pyrrhotite. Middle—regression is within uncertainty of horizontal (no bias introduced). Bottom—method 3 underestimates by 0.3 (±0.2, 1σ) log units.

Conversely, if the current state of sample pyrrhotite is amenable to analysis, then the sulfur fugacity of the system can be directly calculated by using the equations of Toulmin and Barton (1964). This allows sulfur fugacity to be used to calculate oxygen fugacity. In the case where copper is present in pyrrhotite, there are two sources of error: the location of the magnetite–pyrrhotite boundary in fO_2–fS_2 space, and error introduced by inaccurately calculating the sulfur fugacity of the system, yielding a total error equal to ~¼ log unit fO_2 per wt % copper in pyrrhotite.

Table 2-3 Calculated sulfur fugacity from volcanic pyrrhotite

Source	wt % copper in pyrrhotite	Temperature	log fS_2 (bar)		
			Cu omitted $N = 2\left(\frac{nFe}{nFe+nS}\right)$	Cu incorporated as $CuS_{0.5}$ $N = 2\left(\frac{nFe+nCu}{nFe+1.5nCu+nS}\right)$	Cu incorporated as CuS $N = 2\left(\frac{nFe+nCu}{nFe+nCu+nS}\right)$
Luhr (1984)[1]	2.95%	800°C	-0.8	-1.7	-2.3
Hattori (1996)[2]	2.52%	973°C	-0.7	-1.5	-2.2
Hattori (1996)[2]	6.19%	856°C	0.7	-1.0	-2.6

[1] For copper incorporated as CuS, CuS was removed prior to calculating FeS–S_2 as described in Luhr (1984), and $N = 2\left(\frac{nFe}{nFe+nS}\right)$, producing a slightly different fugacity estimate from method 3.
[2] Nickel incorporated as NiS.

The fugacity of sulfur, oxygen, and water can be used to calculate the fugacities of SO_2 and H_2S, which are the dominant sulfur-bearing gases at magmatic conditions. An error in determining fS_2 would propagate through to calculations of these fugacities. For example, calculating the fugacity of these gases at 1000°C, with fH_2O = 2000, fO_2 at the Ni–NiO buffer, and fS_2 = 0.1, would yield fSO_2 =1.9 and fH_2S =61.4 (all fugacities in bar, calculations based on data from the JANAF tables; Chase 1998). Using method 1 to calculate sulfur fugacity from a pyrrhotite with 6 wt % copper would yield fSO_2 = 10.5 bar, and fH_2S = 345.1 bar. Using method 3 on the same pyrrhotite would yield fSO_2 = 0.2 bar and fH_2S = 7.8 bar. Method 1 overestimates fSO_2 and fH_2S by a factor of 5.6, and method 3 underestimates fSO_2 and fH_2S by a factor of 7.9. Although a minor gas species, fS_2 is a key variable in understanding the dynamics of sulfur in magmas.

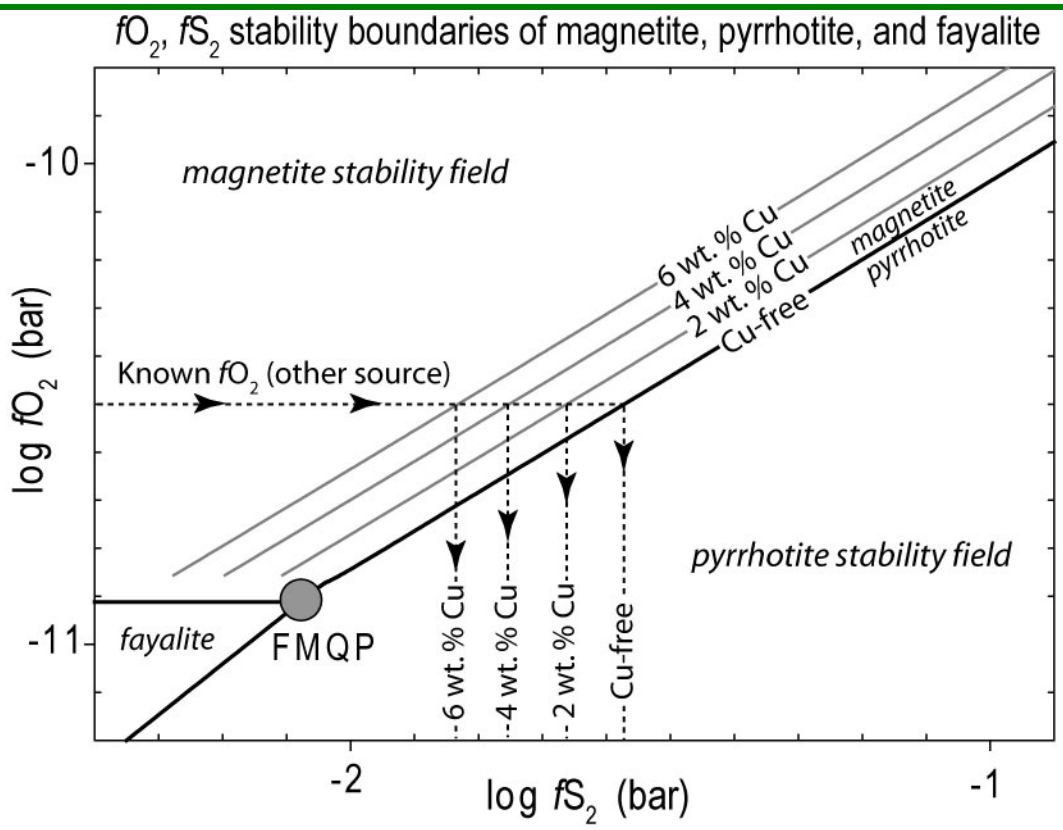

Figure 2-3 The effect of Cu in pyrrhotite on calculated fS_2 from fO_2.
The stability fields of magnetite, pyrrhotite, and fayalite are plotted with respect to sulfur and oxygen fugacity based on Whitney (1984), at 0.1 MPa (1 bar), 1000°C, and quartz saturation. Solid black lines indicate stability boundaries. The location of the magnetite–pyrrhotite boundary moves left with increasing concentration of copper in pyrrhotite (grey lines). If the oxygen fugacity of a system that is known to have contained magnetite and pyrrhotite (in equilibrium) can be established by another method, then it may be translated to sulfur fugacity (dotted lines).

The question of the crystal chemical substitution of copper into the pyrrhotite structure remains. Except in the case of end-member troilite, pyrrhotite possesses vacancies, Fe^{2+} and Fe^{3+} atoms occupying octahedral sites in the structure. Copper may substitute into any of these sites. To address this problem, vacancies were calculated from the cation deficiency of pyrrhotites from these experiments. For example, a run product from experiment 84a with 5.15 % copper has a formula of

$\square_{0.066}Cu_{0.069}Fe_{0.865}S$ (□=vacancy). Comparing the reference and copper-rich pyrrhotites, for every two moles of copper added, one fills a vacancy, and the other replaces an Fe atom. Identifying whether Fe^{2+} or Fe^{3+} has been replaced was calculated assuming that copper in pyrrhotite is present as Cu^{1+} and by using a simple ionic formalism. The results for these experiments are in agreement with Cu^{1+} replacing Fe^{2+} as might be expected. At extremes of high and low sulfur fugacity these relationships may change.

2.7 Conclusions

A method has been identified by which calculations of sulfur fugacity from the composition of copper-bearing pyrrhotite can be performed by using the equation of Toulmin and Barton (1964). Our method expands the applicability of the Toulmin and Barton (1964) equation to include pyrrhotite with major element concentrations of copper. Based on our experiments, substituting $N = 2\left(\frac{nFe+nCu}{nFe+1.5nCu+nS}\right)$ for $N = 2\left(\frac{nFe}{nFe+nS}\right)$ from Toulmin and Barton (1964), results in agreement among copper-bearing and copper-free pyrrhotites formed under the same conditions of sulfur fugacity over the range of copper concentrations studied. The use of this method will allow for consistent reporting among literature sources of sulfur fugacities estimated according to Toulmin and Barton (1964).

2.8 Acknowledgements

This work was supported by the National Science Foundation (EAR 0911098, EAR0738992). The experimental lab was overhauled with financial support of the National Science Foundation (EAR 0842205) and the University of Maryland. We

acknowledge the support of the Maryland NanoCenter and its NispLab. The NispLab is supported in part by the NSF as a MRSEC Shared Experimental Facility. We would like to acknowledge the assistance of Zoltan Zajacz with fugacity calculations. We would also like to acknowledge the helpful comments of our reviews Evgeniy Osadchii and Gleb Pokrovski that enhanced the clarity of this paper.

2.9 Appendix

The methods for calculating mole fractions described in this paper have been derived as follows.

For method 1, N is equal to the mole fraction of FeS ($X_{FeS}^{pyrrhotite}$), in the system FeS–S_2. That is:

$$N = X_{FeS}^{pyrrhotite} = \frac{nFeS}{nFeS + nS_2}$$

where n = number of moles. This can be calculated as:

$$\frac{nFe}{nFe + \frac{(nS - nFe)}{2}} = \frac{nFe}{nFe + \frac{nS}{2} - \frac{nFe}{2}}$$

which simplifies to $\frac{nFe}{\frac{nS}{2} + \frac{nFe}{2}}$, and finally $N = 2\left(\frac{nFe}{nFe + nS}\right)$.

For method 2, N is equal to the sum of the mole fractions of FeS and $CuS_{0.5}$ in pyrrhotite, in the system FeS–$CuS_{0.5}$–S_2. That is:

$$N = \left(X_{FeS}^{pyrrhotite} + X_{CuS_{0.5}}^{pyrrhotite}\right) = \left(\frac{nFeS}{nFeS + nCuS_{0.5} + nS_2} + \frac{nCuS_{0.5}}{nFeS + nCuS_{0.5} + nS_2}\right).$$

This can be calculated as:

$$\frac{nFe}{nFe+nCu+\frac{(nS-nFe-\frac{1}{2}nCu)}{2}}+\frac{nCu}{nFe+nCu+\frac{(nS-nFe-\frac{1}{2}nCu)}{2}}$$

which is equal to $\frac{nFe+nCu}{nFe+nCu+\frac{nS}{2}-\frac{nFe}{2}-\frac{\frac{1}{2}nCu}{2}}$ which simplifies to $\frac{nFe+nCu}{\frac{nFe}{2}+\frac{3nCu}{4}+\frac{nS}{2}}$

and finally $N=2\left(\frac{nFe+nCu}{nFe+1.5nCu+nS}\right)$.

For method 3, N is equal to the sum of the mole fractions of FeS and CuS, in the system FeS–CuS–S_2. That is:

$$N=\left(X_{FeS}^{pyrrhotite}+X_{CuS}^{pyrrhotite}\right)=\left(\frac{nFeS}{nFeS+nCuS+nS_2}+\frac{nCuS}{nFeS+nCuS+nS_2}\right).$$

This can be calculated as:

$$\frac{nFe}{nFe+nCu+\frac{(nS-nFe-nCu)}{2}}+\frac{nCu}{nFe+nCu+\frac{(nS-nFe-nCu)}{2}}$$

which is equal to $\frac{nFe+nCu}{nFe+nCu+\frac{nS}{2}-\frac{nFe}{2}-\frac{nCu}{2}}$ which simplifies to

$\frac{nFe+nCu}{\frac{nFe}{2}+\frac{nCu}{2}+\frac{nS}{2}}$ and finally $N=2\left(\frac{nFe+nCu}{nFe+nCu+nS}\right)$.

Chapter 3: Conditions for Cu-rich sulfide saturation of andesitic melt: influence on Ag and Au deposit formation

3.1 Abstract

Exploring the potential implications of the saturation of magma by sulfides, and in particular copper-rich sulfides, may help to explain the uneven global distribution of porphyry and related magmatic–hydrothermal deposits that remains an important goal of economic geology. A first step is to evaluate the conditions at which the magma will transition from saturation by one sulfide by saturation by another. The transition from an andesitic melt saturated by a Cu–Fe sulfide liquid (CFSL) to one saturated by pyrrhotite will occur at 32 ± 4 ppm copper in the silicate melt (all uncertainties = 1 sigma, standard deviation of the mean) based on experiments performed to evaluate the concentration of copper in an andesitic silicate melt saturated by pyrrhotite, a Cu–Fe sulfide liquid (CFSL), and a H_2O-rich volatile phase. Experiments were performed at 1000°C and 150 MPa, with fO_2 equal to the cobalt–cobalt oxide (CCO) buffer and log fS_2 (determined from the composition of pyrrhotite run products) = -1.5 (bar), or at fO_2 equal to the nickel–nickel oxide (NNO) buffers and log fS_2 = -0.5 (bar), with FeO in the silicate melt ranging from 4 to 6%. The importance of this distinction is highlighted by Nernst-type partition coefficients determined in this study: $D_i^{pyrrhotite/silciate-melt}$ equals 1320 ± 220 for Cu, 1.73 ± 0.37 for Mo, 90 ± 19 for Ag, and 500 ± 87 for Au; and $D_i^{CFSL/silciate-melt}$ equals 7,800 ± 1,400 for Cu, 0.45 ± 0.14 for Mo, 6,800 ± 1,300 for Ag, and 84,000 ± 19,000 for Au.

The separation of sulfide from the silicate melt during partial melting or fractional crystallization will reduce the metal available for later formation of an ore deposit, reducing the likelihood of an ore deposit forming. In one model scenario, up to 50 % Ag, 60 % Cu, and > 99 % Au may be sequestered in CFSL during 30 % Rayleigh fractional crystallization (F=1.0 to F=0.7), with 0.1% sulfide among the separating phases, partition coefficients from this study, and an initial concentration of copper in the silicate melt of 65 ppm. This would greatly reduce the likelihood of formation of a deposit containing gold, and to a lesser extent copper and silver. In models with only pyrrhotite present, the total metal loss was greatly reduced.

The degree to which silicate melts may transport gold, and sulfides may sequester gold, has also been examined in these experiments that are saturated with a Cu–Au alloy. Data from these experiments are consistent with the hypothesis that the solubility of gold in the silicate melt increases as a function of the concentration of sulfur in the melt at $fO_2 \leq$ the NNO buffer, and over the range of fS_2 in this study. Data from these experiments also support a power law relation between the concentration of gold in pyrrhotite and CFSL with fS_2, as the function $X^{po}_{AuS_{0.5}} = K' \bullet (fS_2)^{0.25}$ *(where K' is the apparent equilibrium constant = 0.00028)*, and $X^{CFSL}_{AuS_{0.5}} = K' \bullet (fS_2)^{0.25}$ *(K' = 0.05)*. This suggests the maximum amount of gold that may be sequestered by pyrrhotite and CFSL is reduced at low fS_2, and that the maximum amount of gold than may be transported by silicate melts is reduced at low concentrations of sulfur.

A basic tenet of modeling presented here is that copper is an essential constituent of the CFSL phase, and that sulfide liquids lacking copper will not be

stable. This is in contrast to sulfide liquids at higher temperatures (> ~1050°C depending on fO_2 and fS_2), where the composition of the sulfide liquid can vary from CFSL to a Fe–S–O liquid (FSOL) that contains little or no copper. Given differences between partition coefficients for pyrrhotite and CFSL, and sulfide liquids in general, the temperature of formation during partial melting, or the temperature range within which fractional crystallization occurs, will strongly affect the likelihood or nature of porphyry magmatic–hydrothermal deposit formation.

3.2 Introduction

Magmatic–hydrothermal ore deposits associated with subduction zones are a crucial source of economically important metals; however, the processes that lead to intrusions lacking significant mineralization versus those that generate the wide diversity of intrusion-related ores remain a subject of contention. A requirement for deposit formation is the transfer of metals and sulfur from mantle or lower crust to the Earth's epizone. However, the effectiveness of this transfer and the likelihood of deposit formation may be reduced during the differentiation of arc magmas to the intermediate to felsic compositions associated with porphyry and other magmatic–hydrothermal ore deposits. During evolution of these magmas, the separation of sulfides can exert a strong control on ore metal concentrations in magmatic systems (*cf.*, Jugo et al. 1999). Depending upon the ranges of temperature, pressure, fugacities of oxygen and sulfur, and concentrations of copper in the melt, various sulfide phases may be stable in the hypersolidus assemblage during arc magma evolution. A series of experiments are presented here to investigate the role of Cu–Fe

sulfides in controlling the budget of select ore metals (Cu, Mo, Ag, Au) in andesitic magmas.

Porphyry and other magmatic–hydrothermal ore deposits are spatially and temporally associated with subduction zones (e.g., Sinclair 2007, Sillitoe 2010). These ore bodies form when metals and sulfur from upper crustal felsic to intermediate magma chambers are transferred by a magmatic volatile phase along temperature and chemical gradients to sites of ore deposition which can become significantly enriched in Cu, Mo, Ag, Au and other elements relative to crustal averages (e.g., Hedenquist et al. 1998, Hedenquist and Lowenstern 1994, Redmond et al. 2004, Candela and Piccoli 2005). Porphyry and related deposits are shallow-level expressions of magma produced in subduction zones and are a record of processes that affect the total and relative abundances of ore metals.

Sulfide minerals not only host Cu, Mo, Ag, and Au in porphyry and related hydrothermal deposits, but sulfides are also common accessory minerals in intrusive and extrusive igneous rocks (Sillitoe 2010). Cu, Ag, and Au have been shown to partition preferentially into magmatic sulfide phases relative to silicate melt (e.g., Lynton et al. 1993, Jugo et al. 1999, Simon et al. 2008, Bell et al. 2009, Stimac and Hickmont 1994, 1996). Mo is also associated with porphyry deposits and has been shown to partition into FSOL and pyrrhotite (Mengason et al. 2011), and to form magmatic molybdenite (MoS_2, Audetat et al. 2011). Copper, Ag, and Au are incompatible in most silicate and oxide phases, as is Mo to a lesser degree, and at depth the presence of an H_2O-rich volatile phase is unlikely. Partial melting in the absence of sulfides will therefore concentrate the metals in the silicate melt. Efficient

scavenging of ore metals from the source region by the silicate melt during the generation of arc magmas is the first step in increasing the likelihood of porphyry deposit formation. Sulfides present among residual phases may retain a large portion of the metals, reducing the ore forming potential of the generated magmas.

Porphyry deposits are shallow features but the source of metals may be in the lower crust or mantle wedge, depending on the prevailing sources of magmas in the area. Effective transport of ore metals through the crust by the magma is the second step in increasing the likely of porphyry deposit formation. Fractional crystallization will commonly affect rising magmas within the crust. Fractional crystallization is one method for generating the differentiated intermediate-to-felsic magmas associated with porphyry deposits. Silicate melts undergoing fractional crystallization in the absence of sulfides or an H_2O-rich volatile phase would not be expected to lose metals given the incompatibility of porphyry ore metals in silicate and oxide minerals. However, ore metals carried by the silicate melt will partition strongly into any sulfides formed during fractional crystallization. Sulfides separated from the silicate melt along with other cumulate phases will sequester metals, reducing the total metal load of the silicate melt, and reducing the likelihood of porphyry deposit formation.

One goal in the quest to better understand the distribution of porphyry deposits is to evaluate the role of sulfides in these two processes. In order to evaluate the effect of sulfides on the potential for porphyry deposit formation, it is important to investigate which sulfides may be present during partial melting or fractional

crystallization, and to what degree to ore metals (Cu, Mo, Ag, and Au) will partition into various sulfide phases.

Sulfides identified in arc magmas are commonly Fe- and Cu-rich (e.g., Stimac and Hickmont 1996, Luhr et al. 1984, Hattori 1996, see section 3.2.1). But, there is no single sulfide archetype, in the sense of one structure and one composition that spans the temperature, pressure, and oxygen and sulfur fugacity range of magma in arc systems. The only stable sulfide phase at temperatures in excess of 1200°C is a sulfide liquid that is immiscible within a silicate melt. Sulfide liquids can be thought of as solutions of Cu- and Fe-rich end-members (Fleet 2006). Pyrrhotite has been shown in experiments to coexist with FSOL (Naldrett 1969) and CFSL (Kullerud 1968) at temperatures below 1192°C. In the system Cu–Fe–S, chalcocite (Cu_2S) can coexist with a sulfide liquid starting at 1129°C. Iron substitution for copper expands the stability field from Cu_2S to less Cu-rich compositions at lower temperatures, and chalcocite becomes one end-member of bornite solid solution (*bornite* = Cu_5FeS_4) (Kullerud 1968). In the Cu–Fe–S–O system, at ~850°C, no sulfide liquids are stable and only crystalline sulfides remain (Kullerud 1968 and Naldrett 1969). Therefore a silicate melt in arc magmas at temperatures from ~1200°C to ~850°C could be saturated by a sulfide liquid, pyrrhotite, bornite solid solution, or a sulfide liquid and pyrrhotite, or a sulfide liquid and bornite solid solution.

Among sulfide phases, partition coefficients ($D_{Au}^{sulfide/silicate-melt}$) for ore metals vary widely. For example, partition coefficients for Au are greater for intermediate-solid-solution ($CuFeS_2$, a high-temperature form of chalcopyrite) than pyrrhotite (Jugo et al. 1999, Bell et al. 2009). Partition coefficients for gold are also greater for

FSOL than for pyrrhotite (Mungall 2005, Mengason 2007, Simon et al. 2008). In the examples above, gold partitions more strongly into the more Cu-rich sulfide or the sulfide liquid, relative to pyrrhotite. Partition coefficients between sulfides and coexisting silicate melt influence the degree to which sulfides in the source region can decrease the efficiency with which ore metals are scavenged and the degree to which ore metals are lost to sulfide separation during fractional crystallization. Because partition coefficients can vary significantly from one sulfide to another, and because the hypersolidus sulfide assemblage present may change as a function of the intensive variables that prevail during magmatic differentiation, modeling the budget of chalcophile elements in magmas requires an understanding of which sulfide phases are present in at a range of temperatures and conditions.

This chapter includes a review of examples of the concentration of copper in arc magmas and in sulfide phases to illustrate the ubiquity of sulfides throughout magmatic processes and to underscore the need to understand the conditions necessary for formation of Cu-rich sulfide phases. The results of experiments designed to investigate whether Cu-rich pyrrhotite, a Cu-Fe sulfide liquid (CFSL), or both will be stable as a function of the concentration of copper in a silicate melt, are presented. With these experiments, the hypothesis that $D_i^{sulfide/silicate-melt}$ for Mo, Ag, and Au will be greater for CFSL than pyrrhotite is tested; these data support this behavior for Ag, and Au, but not Mo. Finally, the relative effects of CFSL and pyrrhotite on the metal budgets of Mo, Ag, and Au are examined during the formation by partial melting and the crystallization of arc magma.

3.2.1 Copper in arc magmas

Estimates of the concentrations of copper in arc magmas can be made based on: (1) the bulk rock chemistry of extrusive rocks and shallowly-emplaced intrusive rocks; (2) the bulk rock chemistry from exposed crustal arc sections; and (3) the chemistry of silicate glasses and Cu-bearing phases present in inclusions in minerals and rapidly quenched volcanic ejecta.

3.2.2 Bulk rock chemistry of volcanic and plutonic rock

Compositions of wide ranges of rock types are aggregated into databases from a variety of sources. The NAVDAT database (www.navdat.org) tabulates chemical analyses of samples from western North America. The concentrations of copper and silica from the database are plotted in Figure 3-1 for volcanic or plutonic rocks (as identified by the original authors). The average concentration of copper in the rocks decreases with increasing concentrations of silica. Outliers for volcanic rocks extend upwards to ~1000 ppm Cu, and outliers for plutonic rocks extend to > 1 wt % Cu. Samples with high concentrations of copper span the range of concentrations of SiO_2 and likely indicate the presence of Cu-rich sulfides. Even omitting outliers, for any given concentration of SiO_2, the range of copper concentrations can typically span more than an order of magnitude. This suggests that small amounts of Cu-bearing phases are common throughout the dataset, and, it would be incorrect to assume that they occur only in the case of extreme values. Further, these Cu-bearing sulfides may be, in part, hydrothermal and not magmatic, and therefore the estimate of magmatic copper concentrations based on these data should be considered a maximum.

Experiments reported here fall in the range of 58–62 wt % SiO_2 (anhydrous). Samples from the NAVDAT database, excluding samples with greater than 200 ppm Cu (which includes 97 % of the data), with 58–62 wt % SiO_2 have 34 ± 29 ppm Cu (80±800 ppm Cu including all data).

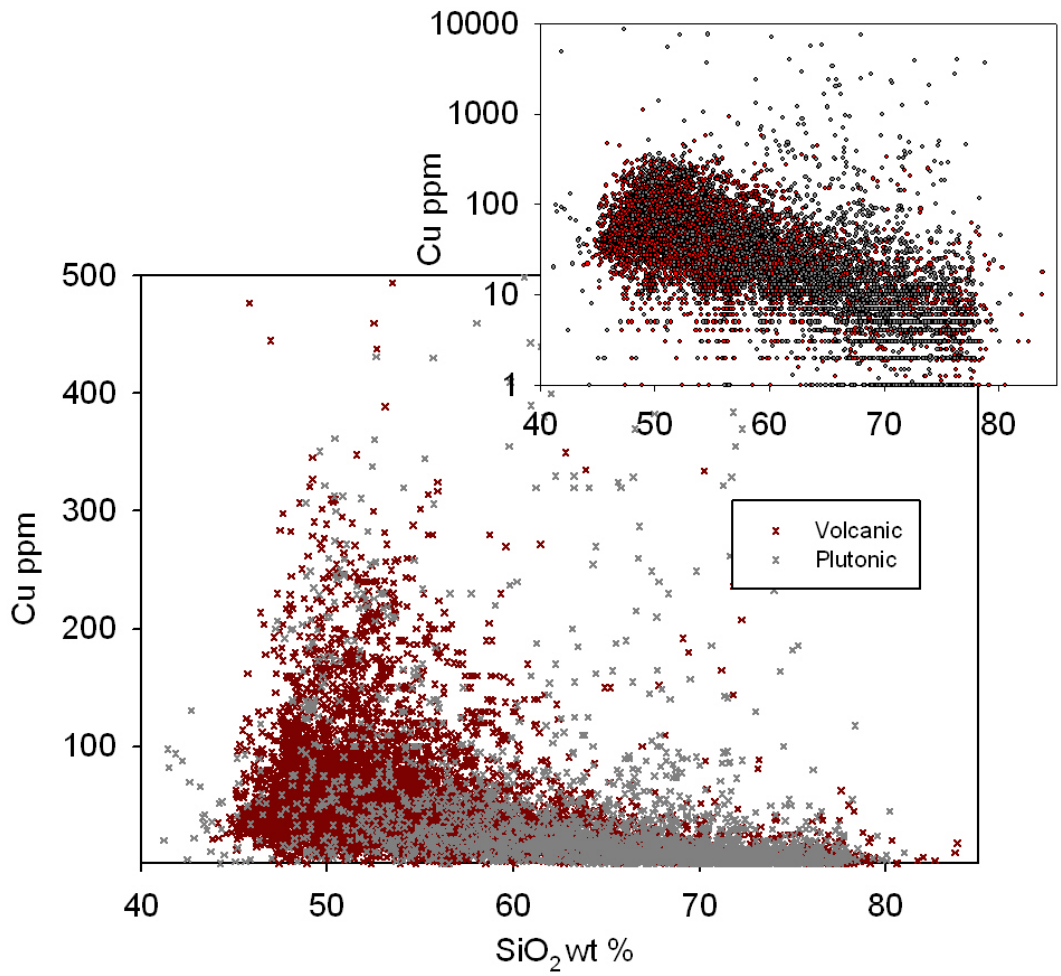

Figure 3-1 Concentrations of Cu from the NAVDAT database
Concentrations of copper from bulk rock analyses plotted against the concentration of SiO_2 for volcanic and plutonic rocks from the western U.S. and Mexico. Data taken from the NAVDAT database. Inset shows log-scale plot of the same data. Copper concentrations decrease with increasing silica content. Many individual samples plot well above the general trend and likely contain Cu-sulfides. Omitting outliers with > 200 ppm Cu, the average concentration of copper in rocks with 58 to 62 wt % SiO_2 is 34 ± 29 ppm.

3.2.3 Data from igneous rocks in arcs

Copper concentrations in rocks from exposed sections of two island arcs and one continental arc are included here. Exposed sections provide an excellent record of how copper is segregated during crystallization and remelting within arcs. In general, copper concentrations are inversely proportional to SiO_2, as described above.

In plutonic and volcanic rocks of the Bonanza group, interpreted as an accreted island arc section on Vancouver Island, Canada (Debari et al. 1999), concentrations of copper decrease with increasing concentrations of SiO_2 (Larocque and Canil 2010, Figure 3-2). In this sequence, the authors interpret basal mafic units (olivine-, hornblende- or plagioclase-bearing) as cumulates produced during fractional crystallization, which drove the parent melt to intermediate and felsic compositions. The lowest SiO_2 rocks described are olivine cumulates which do not fit the trend of decreasing copper with increasing SiO_2 concentration. These rocks, with approximately 40% SiO_2, have 21 ppm Cu on average compared with dominantly hornblende- (44 % SiO_2, 85 ppm Cu) and plagioclase-bearing (47 % SiO_2, 71 ppm Cu) cumulates. Melts separated from these cumulates formed mafic volcanic rocks (48 % SiO_2, 57 ppm Cu), a series of intrusive rock ("gabbro to diorite"—Figure 3-2) average (51 % SiO_2, 55 ppm Cu), and a series of plutonic rocks with intermediate (57 % SiO_2, 22 ppm Cu) to more felsic (70 % SiO_2, 7 ppm Cu) compositions (Larocque and Canil 2010).

In the Talkeetna arc section, south-central Alaska, USA (Greene et al. 2006), concentrations of copper decrease with increasing SiO_2 (that is, they are higher in mafic cumulates than in separated felsic melts) (Figure 3-2). The Talkeetna formation

(Pflaker et al. 1989) and related rocks are interpreted to be part of an accreted island arc section that exposes units from the upper mantle to volcanic units of the upper crust. Greene et al. (2006) interpret part of the sequence as basal cumulate gabbronorites associated with mid and upper-crustal plutonic and volcanic daughter products. The gabbronorites have a range of SiO_2 and concentrations of copper that average 47 % SiO_2 and 173 ppm Cu (41–53% SiO_2 and 830–5 ppm Cu). The ultramafic rocks average 43 % SiO_2, and 406 ppm Cu and the basaltic rocks average 48 % SiO_2, 95 ppm Cu. Melts separated from cumulates produced basalts (49 % SiO_2, 53 ppm Cu), chilled mafic magmas in the margins of dikes (52 % SiO_2, 77 ppm Cu), basaltic andesites (57% SiO_2, 70 ppm Cu), intermediate members of an intrusive suite (58 % SiO_2, 77 ppm Cu), dacites (68 % SiO_2, 83 ppm Cu), and felsic members of an intrusive suite (70 % SiO_2, 9 ppm Cu). There is little change among the concentrations of copper in the daughter melts, save the dramatic decrease in concentrations of copper in the most felsic members.

In the Famatinian arc section, Argentina (Otamendi et al., 2009), concentrations of copper similarly decrease with increasing concentrations of SiO_2. (Figure 3-2) The Famatinian section represents a continental arc formed during subduction on the margin of Gondwana (Pankhurst et al. 1998). Concentrations of copper decrease from a chilled basaltic dike (45% SiO_2, 225 ppm Cu) and gabbroic enclaves (45% SiO_2, 143 ppm Cu), to mafic melanosomes in migmatites (51% SiO_2, 111 ppm Cu), tonalitic rock (54% SiO_2, 60 ppm Cu), through intermediate (59 SiO_2, 66 ppm Cu), to felsic leucotonalitic veins (71% SiO_2, 14 ppm Cu), and leucogranitic veins (74% SiO_2, 2 ppm Cu). Otamendi et al. (2009) do not suggest a simple

fractional crystallization trend among the units; rather, they propose that the gabbroic intrusions at the base of the section led to the generation of the leucogranitic veins by melting of metasedimentary country rock, creating metasedimentary migmatites (62 SiO_2, 2 ppm Cu). They proposed that the leucogranitic melts caused partial melting (partial remobilization) of previously emplaced mafic igneous rock, generating mafic migmatites and melts of intermediate compositions that interacted with existing country rock to form tonalites and diorites. The diorites have wide ranging concentrations of SiO_2 and copper, which, according to their model, is dependent upon the amount of mafic rock assimilated.

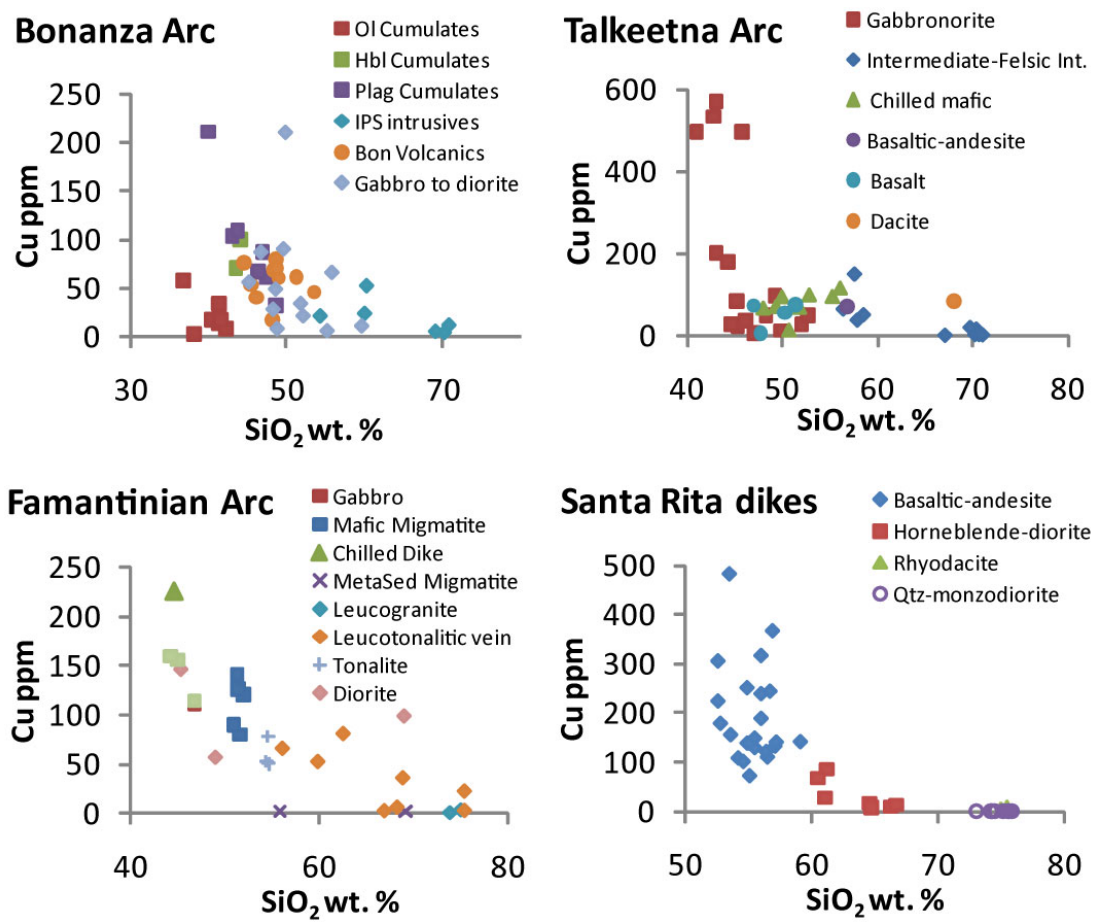

Figure 3-2 Concentrations of Cu from arc sections and dikes
Copper concentration as a function of the concentration of silica for the arc sections discussed in the text: Bonanza arc—Larocque and Canil, (2010); Talkeetna arc—Greene et al. (2006); Famatinian arc—Otamendi et al. (2009). Proposed fractional crystallization and partial melting produce similar trends. A similar trend is apparent in melt inclusions from dikes associated with porphyry Cu mineralization at Santa-Rita, NM (Audetat and Pettke 2006).

3.2.4 Silicate and sulfide melt inclusions in basaltic andesite to rhyodacite dikes

In a study of basaltic andesite to rhyodacite dikes associated with porphyry Cu mineralization at Santa Rita, New Mexico, Audetat and Pettke (2006) analyzed silicate glass and sulfides present in melt inclusions found in igneous minerals (Figure 3-2). Small dikes may cool rapidly and preserve the composition of early melts that

later undergo substantial differentiation. Melt inclusions were found in minerals in basaltic andesites (average: 55 wt % SiO_2, 200 ppm Cu), hornblende-diorites (64 wt % SiO_2, 30 ppm Cu), quartz-monzodiorite (75 wt % SiO_2, 24 ppm Cu), and rhyodacite (75 wt % SiO_2, 6 ppm Cu). Sulfide inclusions were also found in the basaltic andesite (averaging 46 wt % Cu), the hornblende-diorites (pyrrhotite with 1–6 wt % Cu), and rhyodacite with (pyrrhotite 1–3 wt % Cu, and a more Cu rich phase with 24 % Cu).

3.2.5 Sulfide inclusions in erupted minerals and glass

Hattori (1996) identified sulfide inclusions in quenched glass and minerals from basaltic, andesitic, and dacitic volcanic rocks from the 1980 eruption of Mt. St. Helens. Sulfides in the volcanic glass are both globular (suggestive of the presence of a sulfide liquid immiscible in the silicate melt) and angular (suggestive of crystalline sulfides). The range of sulfide compositions and the range of minerals serving as hosts to sulfide minerals both underscore the ubiquity of sulfide–silicate melt interactions during magma emplacement and differentiation. Examples of sulfides identified from dacites, andesites, and basalts are detailed below.

Sulfides in dacitic pumices occur in glass, plagioclase, hornblende, orthopyroxene, potassium feldspar, and magnetite. Most sulfides (21 samples) have chalcopyrite-like compositions with the concentration of copper averaging 31±4 wt %. Some chalcopyrite grains were analyzed for trace elements, and averaged 26±14 ppm Ag, and ≤8 ppm Mo. Analysis of the Cu-rich portion of a glass-hosted sulfide revealed a bornite-like composition, with 56±2 wt % Cu. Trace element analysis of

sulfides comprising a mixture of chalcopyrite and bornite yielded 170±80 ppm Ag and 4 to 149 ppm Mo. Pyrrhotite was reported as inclusions in the glass and in hornblende, ranging from Cu-free to 0.65 wt % Cu.

Chalcopyrite occurred in a sample of andesite as inclusions in glass, potassium feldspar, hornblende, and orthopyroxene, and averaged 32±5 wt % Cu. Bornite (53.7 wt % Cu) was found with chalcopyrite in one of the glass-hosted inclusions. Pyrrhotite that ranged in composition from Cu-free to 6.2 wt % Cu was hosted in ilmenite and orthopyroxene, and identified within a crystal mass of olivine and hornblende.

A basalt fragment yielded a larger range of sulfide compositions. Two sulfides, with an average concentration of copper of 32±1 wt %, were found in contact with magnetite and glass. One of those inclusions also hosted bornite with 52 wt % Cu. Hornblende and orthopyroxene also hosted a series of sulfides with compositions intermediate between pyrrhotite and chalcopyrite, ranging from 8 to 23 wt % Cu. Pyrrhotite in potassium feldspar, glass, hornblende, clinopyroxene, and ilmenite ranged from Cu-free to 2.5 wt % Cu. Nickel was present in most of the pyrrhotite grains. One Cu-free pyrrhotite contained 30 ppm Ag, and another contained 26 ppm Mo. One Cu-bearing pyrrhotite contained 64 ppm Mo and 46 ppm Ag.

3.2.6 Cu–Fe sulfide saturation in arc magma

In data from NAVDAT and in the arc sections presented, the concentration of copper in arc magma is inversely proportional to the concentration of silica. Data

from Audetat and Pettke (2006) as well as others (e.g., de Hoog et al. 2001, Halter et al. 2005) indicate that basaltic melts in subduction zones have concentrations of copper considerably higher than in felsic melts. Low concentrations of copper in evolved arc magmas suggest sequestration of copper in cryptic reservoirs to satisfy simple mass balance. The most likely reservoir is sulfides in mafic cumulates found at the base of exposed arc sections. In both the Talkeetna and Bonanza arc sections, Cu-rich sulfides have been identified within mafic cumulates (Richards 2011). In another example, the porphyry Cu deposits at Bingham, Utah, chalcopyrite and bornite make up 0.3 wt % and 2 wt % respectively of mafic enclaves thought to be the products of crystallization which produced intrusions of granitoid composition (Core et al. 2006). The sulfide inclusions detailed by Hattori (1996) are present in a range of melt compositions and in minerals that formed at a range of temperatures, suggesting that sulfides form not in discrete events but rather throughout arc-magmatic systems. Sulfides, and in particular Cu-rich sulfides, play a continuing role in the evolution of the metal budgets of chalcophile elements throughout the process of magmatic differentiation. Data are needed on the conditions required to saturate the range of melt compositions in arc magmas with Cu–Fe phases, in order to model the effect of sulfides on the budgets of ore metals.

Previous work on the saturation of silicate melts with Cu–Fe sulfide phases includes sulfide liquids in basaltic melts (Holzheid and Lodders 2001, Ripley et al. 2002), and sulfide minerals in rhyolitic melts (Jugo et al., 1998). The conditions chosen are intermediate in both composition (andesitic) and temperature (1000°C),

and allow examination of a two-sulfide magmatic system, to evaluate the effects of sulfide saturation in silicate magmas.

Experiments presented here were designed to replicate, under controlled conditions, a magma consisting of a melt of andesitic composition, pyrrhotite, and a Cu–Fe–S liquid (CFSL). These experiments had three goals: to determine the concentration of copper necessary to saturate an andesitic melt with pyrrhotite only, as opposed to CFSL and pyrrhotite, or with CFSL only; to determine partition coefficients for the distribution of Cu, Mo, Ag, and Au among the sulfide phases and the silicate melt; and to identify processes in subduction arc magmatism which may enhance or diminish the potential for ore deposit formation.

3.3 Experimental methods

As part of the experimental program, two series of experiments were designed and performed for this research. One series of experiments contained pyrrhotite, CFSL, an andesitic melt, and a volatile phase, enclosed in a gold capsule loaded into cold-seal pressure vessels. In addition to these a second, simpler, series of experiments contained just pyrrhotite and CFSL enclosed in sealed evacuated silica tubes. The two series were complimentary. The silica tube experiments yielded data on the equilibrium compositions of pyrrhotite and CFSL and partition coefficients for the ore metals between them under more controlled conditions than in the hydrothermal experiments allowing the effect of oxygen and gold metal saturation on the compositions of the sulfide phases to be investigated independently. The

hydrothermal experiments yielded data on the concentrations of Cu, Fe and S in an andesitic melt saturated with both pyrrhotite and CFSL, and partition coefficients among pyrrhotite, CFSL, and the silicate melt. Data from the simplified system served as a baseline for understanding the results of the more complete system.

The technique employed here for the hydrothermal experiments follows traditional cold seal pressure vessel methodology. This method of applying pressure to the sample was chosen based on the pressure and temperature regime of interest, for the ability to generate a hydrous silicate melt, and to use larger sample sizes relative to piston cylinder or diamond anvil techniques. Many experimental studies involving silicate melts are performed under atmospheric pressure. However, for these experiments, the liquidus for both the silicate and sulfide phases had to be considered. At the higher temperature needed to form a dry andesitic melt, pyrrhotite would not be stable, or would be stable over only a narrow range of sulfur fugacities. The system used here allows experiments to be performed in a temperature and composition space poorly represented in the literature but typical of ore-forming arc magmas.

As a guide to the run-product compositions expected in the Cu–Fe–S system, phase diagrams from Kullerud (1968, Figure 3.3 base) and Chang et al. (1989), are useful starting points. In the Cu–Fe–S system, at 1000°C, pyrrhotite (containing up to ~6 wt % Cu) can coexist with Cu-rich CFSL. Those compositions are strongly dependent on fS_2. In the Fe–S–O system, oxygen can account for 8–10 wt % of sulfide liquids coexisting with magnetite and pyrrhotite (Naldrett 1969, Simon 2008, Mengason 2011) (Figure 3-3, side). At the fO_2, and fS_2 of this system, the

temperature (1000°C) is too low to form FSOL. Studies of the sulfide liquids in the Cu–Fe–S–O system have produced sulfide liquids with much less oxygen, on the order of 1–2 % (Ripley et al. 2002, Mungall et al. 2005, Kress 2008) with oxygen and copper concentrations inversely related. Preliminary hydrothermal experiments contained pyrrhotite run products with lower-than-expected concentrations of copper. Oxygen may lower the melting point of CFSL, changing the composition of coexisting Cu-rich sulfides. In addition, variable gold contents between runs at different fO_2 and fS_2 conditions suggested a need for investigation of the system Au–Cu–Fe–S–O to better interpret these results. The simplified series of experiments were designed to allow examination of the Cu–Fe–S and Cu–Fe–S–O systems, both with and without gold saturation, at the same temperature and over the same range of fO_2 and fS_2 of the more complete hydrothermal experiments.

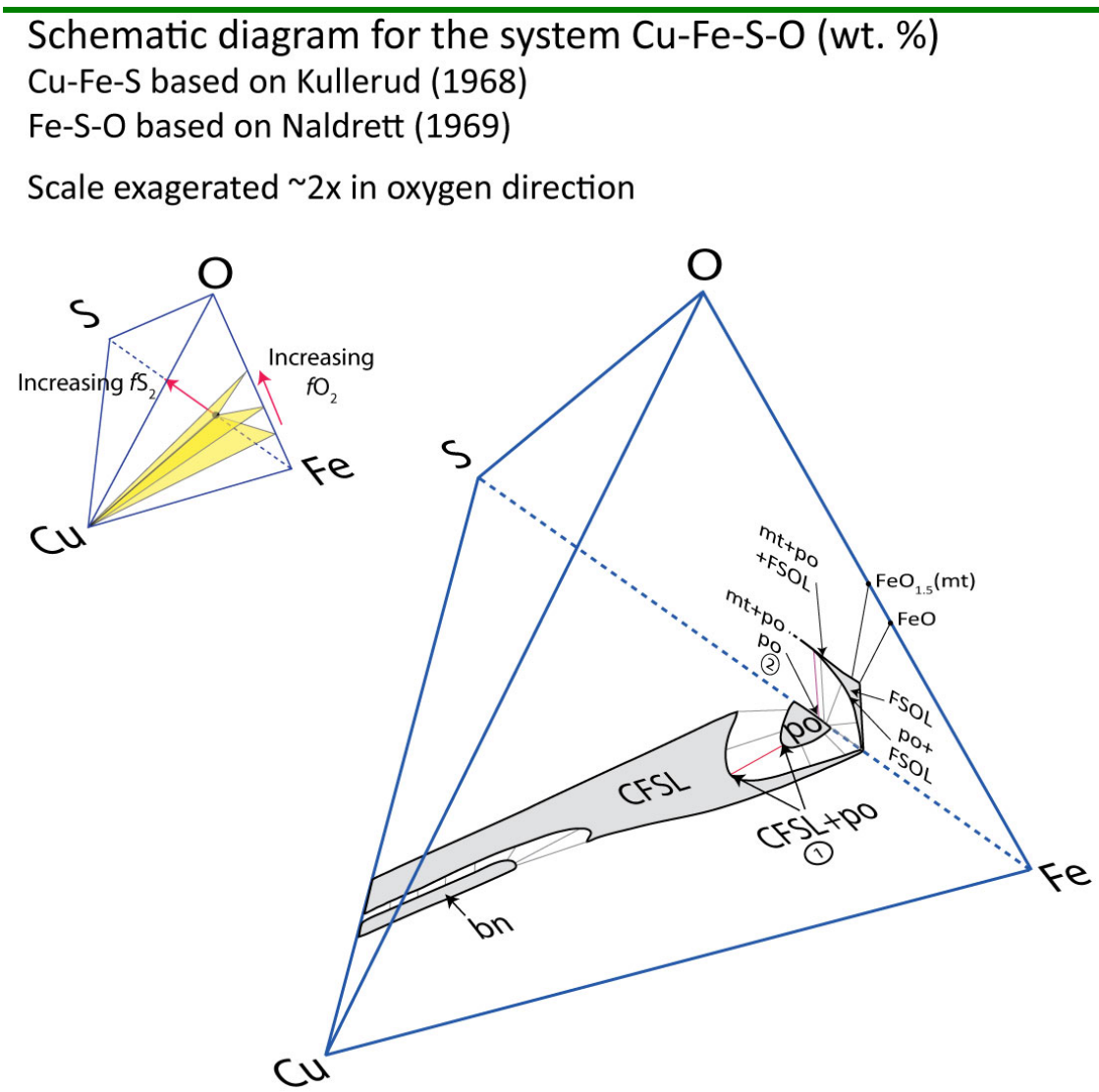

Figure 3-3 Schematic phase diagram of the system Cu–Fe–S–O for 1000°C.
Note that this system is a subsystem of the larger experimental and natural systems which are the object of this study. Please note that a gas phase is also present and that the scale is exaggerated toward the oxygen apex. In the range of fO_2 and fS_2 of experiments performed here, the possible solid phases include pyrrhotite (po), bornite solid solution (bn), and magnetite (mt). The solid phases are connected by tie lines (thin grey, red, or purple tie-lines) to Cu–Fe–S liquid (CFSL) or Fe–S–O liquid (FSOL). (1) Experiments were designed to co-saturate a silicate melt with po and CFSL (red tie line). At lower fO_2 and fS_2 (*see inset diagram, yellow planes illustrate sections through the diagram*), CFSL and FSOL are end members of a single sulfide liquid phase field (not shown) connecting the liquid fields in the Fe–S–O and Cu–Fe–S systems. However, at higher fS_2 and fO_2 the CFSL field does extend to FSOL compositions. (2) The silicate melt is saturated with po but not mt in these experiments. Even if the melt had been saturated with mt (purple tie line), FSOL would not have been stable at this temperature.

3.3.1 Design of the Cu–Fe–S system experiments

In a study of the effect of copper on the fugacity–composition relationships for pyrrhotite, Mengason et al. (2010) used evacuated sealed silicate tubes that were divided into chambers to allow multiple sample charges consisting of pyrrhotite and bornite to be run together without coming into physical contact with one another. The sulfur-bearing volatile phase was able to communicate between the chambers, which allowed all samples to come into equilibrium with the same volatile phase, and therefore the same fugacity of sulfur. In those experiments, pyrrhotite with approximately 2, 4, and 6 wt % Cu were produced. The design of silica tube (Figure 3-4) in the current study builds on the design of Mengason et al. (2010) with three additions: bornite and pyrrhotite were doped with Mo, Ag, and Au; the ratio of bornite:pyrrhotite in these experiments allowed pyrrhotite and CFSL to be formed; and Cu–Au alloy metal was added to replicates in additional chambers included within each silica tube. These changes allowed pyrrhotite and CFSL to be recovered from the experiments, partition coefficients ($D^{CFSL/po}$) to be calculated for Mo, Ag and Au, and the maximum concentration of Au in metal-saturated CFSL to be measured. Pyrrhotite and bornite starting materials were synthesized in sealed evacuated silica tubes for these experiments. Compositions of the starting materials are listed in Table 3-1.

Table 3-1 Compositions of starting material sulfides (by EMPA)

	Cu		Fe		S		Ag		Au		Mo		Total
	wt % (1σ)						ppm (1σ)						
pyrrhotite	0.04	*0.01*	59.2	*0.1*	40.21	*0.07*	570	*40*	330	*20*	260	*80*	99.5
bornite	63.8	*0.5*	10.8	*0.2*	26.8	*0.3*	1000	*100*	700	*200*	130	*140*	101.6

As described in Mengason et al. (2010), silica tubes were cleaned, dried, and fused at one end with a methane–oxygen torch to form a test-tube shape. The silica tubes had an outer diameter of 4 mm, and a wall thickness of 1 mm. If a small sample of material were to be spread over a large area, some grains could be isolated from the majority of the charge resulting in heterogeneity in the run products. The smaller interior diameter of the silica tube, relative to Mengason et al. (2010), allowed less starting material to be safely used in each charge. In addition, a narrower tube with thinner walls equates to less total silica, and less thermal mass, and gives the potential for a more rapid quench. Pyrrhotite was loaded into the bottom of the silica tube to serve as an fS_2 sensor. 'Sensor' pyrrhotite was synthesized with only trace Cu, Mo, Ag, and Au. A silica rod, 2 mm in diameter by approximately 2 mm in length, was added to separate the sensor from the first charge. All of the silica-rod spacers slid slowly into the tube under their own weight, indicating that air could pass around the spacer but that there was not a large gap between the spacer and the tube walls. A mixture of bornite and pyrrhotite was then added, along with a Cu–Au alloy (Cu_6Au_{94} in runs 116a–b, Cu_3Au_{97} in runs 117a–b and 118a–b). Another spacer was added, followed by bornite and Cu–Au alloy. This was then repeated without the alloy to create two more chambers (Figure 3-4). The loaded silica tube was placed under vacuum and sealed.

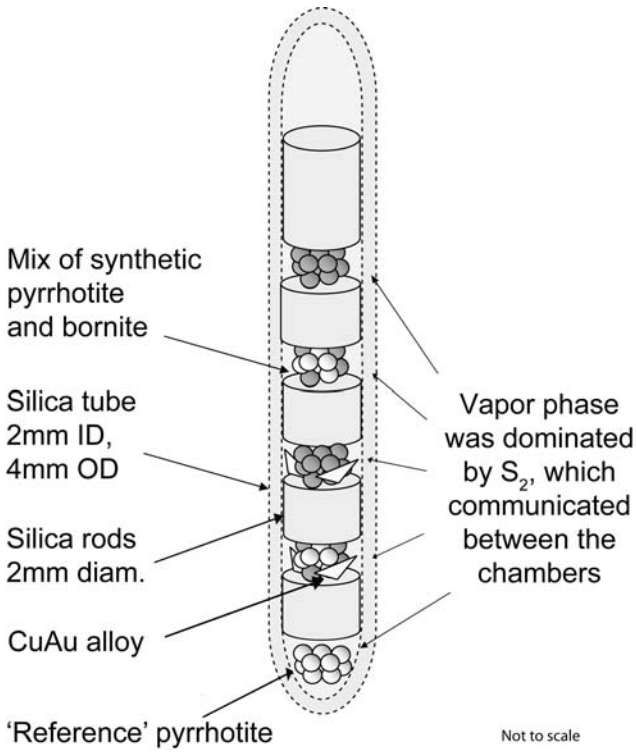

Figure 3-4 Design of the Cu–Fe–S silica tube experiments.
(left)
Silica tubes were divided into chambers by silica rods which prevented direct contact between charges, but allowed a common sulfur volatile phase to develop and equilibrate.

Table 3-2 Contents of the Cu–Fe–S experiments
(Below)
Weight (in mg) of pyrrhotite (po) and bornite (bn), used in experiments. In order to reduce the intrinsic sulfur fugacity of some experiments, Cu was added to experiment 116b (mass not recorded) and Fe was added to experiments 118a and 118b in separate chambers (not shown).

		116a mg	116b mg	118a mg	118b mg
4	bn	6.0	6.2	4.0	4.1
3	po	6.0	5.6	6.2	6.1
	bn	0.7	1.2	0.9	1.1
2	bn	6.1	6.2	4.1	3.8
	Alloy	1.5	1.5	1.2	1.3
1	po	6.2	6.2	6.3	6.1
	bn	0.8	0.9	1.0	1.0
	Alloy	1.5	1.3	1.4	1.2
	Fe	–	–	0.8	1.0

3.3.2 Design of the Cu–Fe–S–O system experiments

Performing experiments that contain magnetite in silica tubes is problematic. At the site of contact between magnetite and silica tube wall, the silica glass devitrifies and can no longer isolate the system from the outside environment. This is also true for 'oxy-sulfide' liquids such as an Fe–S–O liquid *(FSOL)* (Naldrett 1969, Mengason 2007). In order to expand from the Cu–Fe–S system to the Cu–Fe–S–O system, some material must be used to separate the oxygen-bearing phase from the

silica tube. In experiments detailed in Mengason (2007), Simon et al. (2008), and Mengason et al. (2011), magnetite and pyrrhotite were loaded into a depression in packed rhyolitic glass powder so that—at temperature—the magnetite, pyrrhotite, and Fe–S–O melt would be ensconced within the rhyolitic melt. However, this added other experimental difficulties, and was not used here. Silver foil has been used to isolate iron from the walls of the silica tube in the synthesis of magnetite, but silver would melt at this temperature. Copper and gold were ruled out, as they were components of the system. Platinum and palladium would interact with sulfides, and also limit the system to one sulfur fugacity. In this case, ceramic thermocouple insulators (alumina–silica) were found to work adequately. The tubular thermocouple insulators were cut and sealed at one end with a methane–oxygen torch in the same manner as the silica tubes. These ceramic tubes were then loaded with the charges and stacked inside the silica tube, which was then evacuated and sealed (Figure 3-2).

One potential disadvantage of this method should be noted. The ceramic tubes appear to have been thermally insulating and led to a coarser-grained sulfide melt than was seen in other experiments (e.g., rapid quench cold seal pressure vessel). In the future, it may be worthwhile experimenting with a series of metals to fill this role. The metal cannot be one that is readily incorporated into the sulfide phases (e.g., Fe, Ni, Zn), or the oxide phases (e.g., Ti, V, Mn). In addition, the metal should not sulfidize or oxidize below the fugacities of interest. Some promising metals, such as tantalum, may fail this criterion.

The composition of these experimental charges is similar to the Cu–Fe–S experiments, with the following differences. Magnetite was included with pyrrhotite

in the bottom ceramic tube, and bornite-only chambers were omitted. Magnetite and pyrrhotite is a sub-solidus assemblage at 1000°C for the range of oxygen and sulfur fugacities of interest. Oxygen and sulfur fugacity were calculated from the composition of pyrrhotite in the run products given the coexistence of magnetite and pyrrhotite (Whitney 1984). Bornite-only chambers were omitted to reduce the size of the silica tube in the furnace, and because bornite behaved unpredictably in earlier, similar experiments.

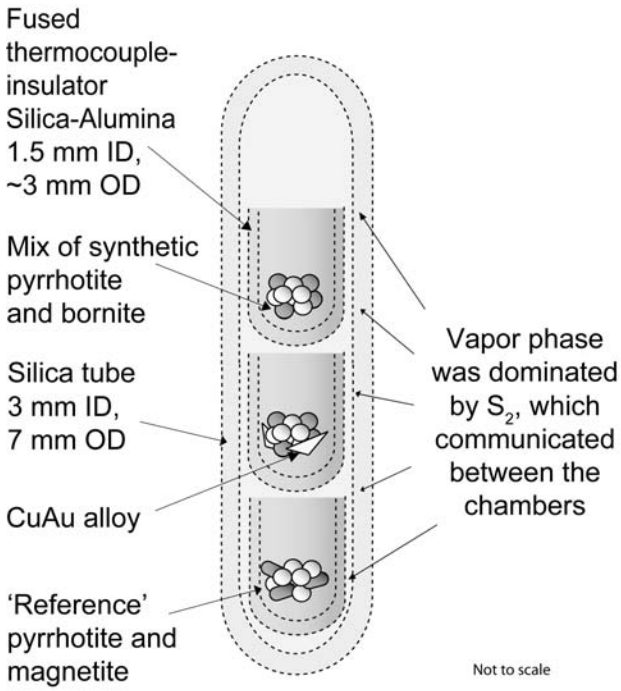

Figure 3-5 Design of the Cu–Fe–S–O silica tube experiments
(left)
Schematic of the fused thermocouple insulators which prevented contact between charges, but allowed a common sulfur volatile phase to develop within the silica tube.

Table 3-3 Contents of the Cu–Fe–S–O experiments
(below)
Weight (mg) of pyrrhotite (po) and bornite (bn) used in experiments. In order to reduce the intrinsic sulfur fugacity of experiment 117b, Cu was added to in a separate compartment (not shown).

		117a mg	**117b mg**
2	po2	2.8	3.4
	bn4	0.4	0.4
1	po2	3.0	3.0
	bn4	0.4	0.3
	Alloy	0.5	0.7
	Cu	–	0.1

3.3.3 Design of the hydrothermal experiments

The hydrothermal experiments were designed to generate a hydrous andesitic melt saturated with pyrrhotite, CFSL, and a H_2O-rich volatile phase, and to allow

these to approach equilibrium compositions with regard to phase assemblage and the distribution of metals among the phases. The temperature (1000°C) and pressure (150 MPa) were chosen to be in a geologically reasonable range for the stability of a hydrous andesitic melt in order to insure saturation by relevant sulfide phases. Lower temperatures would induce crystallization that would hinder analysis and alter the composition of the silicate melt. Higher temperatures would approach the melting point of the capsule alloy. Starting materials included powdered glasses (Table 3-5, AND–2 and AND–4) prepared from a sample of andesite (Table 3-5, sample ID MVO 819 in Zelmer et al. 2003, sample provided by Dr. Stephen Sparks, University of Bristol), synthetic pyrrhotite and bornite (Table 3-1) used to generate Cu-rich pyrrhotite and CFSL, and an aqueous solution to supply additional H_2O to the volatile phase. Magnetite was also added to two experimental charges. A summary of the composition of the experimental charges is provided in table 3-4. The following section provides details of the construction of the experiments (Figure 3-6) and a discussion of some of the constraints which influenced the design.

Table 3-4 Contents of the hydrothermal experiments

	Inner capsule								Outer capsule			
run	Capsule	AND–2	AND–4	bornite	pyrrhotite	silica	magnetite	solution	Co	Ni+NiO	Dist H_2O	buffer
#	Material	mg	mg	mg	mg	prep.?	mg	(ul)	mg	mg	(ul)	type
85	$Cu_{5.6}Au_{94.4}$	22.1		2.9	12.3			8	108.1		40	Pt Cap
86	Cu_3Au_{97}	20.2		1.6	11.9			8	110.5		40	Pt Cap
109	Au_{100}		22.2	1.8	10.0	yes		10	100.4		30	ZrO_2
121	Cu_2Au_{98}		20.4	1.0	5.9	yes		6	56.6		60	ZrO_2
124*	Cu_6Au_{94}		21.7	0.9	6.0	yes		6	61.2		60	ZrO_2
92	Cu_3Au_{97}	22.0		1.5	9.9			5		109.1	30	ZrO_2
94	Cu_3Au_{97}	21.3		1.5	10.3			5		99.0	25	ZrO_2
100	$Cu_{5.6}Au_{94.4}$	21.7		0.7	10.7		3.9	10		90.0	30	ZrO_2
102	Au_{100}		23.1	2.1	8.1		0.5	10		76.8	30	ZrO_2
103	Au_{100}		23.1	1.3	9.2	yes		10		90.6	30	ZrO_2
108	Au_{100}		21.5	1.6	10.2	yes		10		110.0	30	ZrO_2
114	Cu_1Au_{99}		19.1	0.2	8.2			6		258.0	80	ZrO_2
120	Cu_2Au_{98}		21.4	0.9	5.7	yes		6		87.6	60	ZrO_2
125	Cu_3Au_{97}		21.8	1.0	6.2	yes		6		79.2	60	ZrO_2
127	Cu_3Au_{97}		21.8	0.9	6.0	yes		6		62.9	60	ZrO_2

See text for details on phases, capsule materials, and construction details. * = 900°C, all other runs at 1000°C. Silica preparation indicates that the samples were brought to temperature in a silica tube, quenched, then added to these experiments (see text). Aqueous solution = 1.8% NaCl equivalent, Na:K 1:1, Na:H, 10:1, 100 ppm Cs added as CsCl.

In cold-seal pressure vessel research, the sample is contained in a welded noble-metal capsule. The use of gold can be problematic because copper from the experimental charge can alloy with the gold. This would cause a changing bulk sulfide composition until equilibrium with the capsule is reached. To test a method of reducing the time needed for equilibration, some gold tubing (3 mm OD, 0.12 mm wall thickness) used to form the sample capsules was electroplated with copper, and alloyed in evacuated silica tubes (see Zajacz et al. 2011 for details of this method). Given the low melting point of Cu–Au alloys, this limited the experiments to pyrrhotite, or pyrrhotite + CFSL sulfide assemblages. The use of sulfides with a higher concentration of copper would have resulted in capsule failure at the temperature of these experiments.

Sulfides, and sulfide liquids in particular, can incorporate Au into their structure. As was learned during the course of this study, sulfide liquids under conditions created here may have several wt % Au. The sulfide charge could incorporate a part of the capsule at the point of contact, and cause failure. This is particularly likely under conditions of high fS_2, and during the first few minutes of the experiment when the system is out of equilibrium and conditions can fluctuate greatly. One material the sulfides phases are known not to incorporate is a silicate melt. To take advantage of this, the capsule was loaded in such a way that the sulfide phases would be suspended within the silicate melt at run conditions (see Figure 3-6). In general, this was a successful approach.

Table 3-5 Compositions of starting material glasses (by EMPA and LA–ICP–MS)

	AND–2			AND–4			MVO 819
	wt %	*1σ*	*n*	**wt %**	*1σ*	*n*	**wt %**
SiO_2	**58.7**	*0.3*	*10*	***58.3***	*0.2*	*13*	59.96
TiO_2*	**0.53**	*0.1*	*4*	***0.52***	*0.06*	*5*	0.56
Al_2O_3	**16.4**	*0.2*	*10*	***16.0***	*0.2*	*13*	17.68
FeO	**5.3**	*0.2*	*10*	***5.4***	*0.2*	*13*	6.07
MnO*	**0.151**	*0.005*	*4*	***0.12***	*0.01*	*5*	0.17
MgO	**2.76**	*0.07*	*10*	***2.64***	*0.07*	*13*	2.91
CaO	**7.1**	*1.1*	*10*	***6.5***	*0.1*	*13*	7.27
Na_2O	**2.93**	*0.05*	*10*	***3.4***	*0.1*	*13*	3.71
K_2O	**0.81**	*0.08*	*10*	***0.90***	*0.02*	*13*	0.88
Total		**94.7**			**93.8**		**99.9**
H_2O		**5.3**			**6.2**		
Co	***14.2***	*8*	*4*	**12.3**	*0.9*	*5*	15.5
Cu	**< 1**	–	*3*	**0.35**	*0.04*	*5*	19.8
Zn	***71***	*3*	*4*	**70**	*10*	*5*	52.8
Mo	**6.2**	*0.6*	*3*	**0.8**	*0.1*	*5*	–
Ag	***0.02***	*0.02*	*3*	**0.042**	*0.008*	*3*	–
Cs	***0.63***	*0.03*	*4*	**0.56**	*0.02*	*5*	0.60
Au	**0.11**	*0.01*	*3*	**0.13**	*0.04*	*5*	–

For AND–2 and AND–4: Oxides = EMPA analysis except TiO_2 and MnO (*) analyzed with LA–ICP–MS, H_2O by difference from oxide total, trace elements were by LA–ICP–MS. See section 3.3 for details of analyses.
Analyses of MVO 819 taken from Zelmer et al. (2003)

When loading the capsule, powdered andesitic glass (~20 mg) was added first. A depression was formed in the packed powder, and the sulfide starting materials (~10 mg) were placed in this depression, then covered with additional powdered andesite and packed again. See Table 3-4 for the weights of starting materials in specific experiments. The andesitic powder formed a silicate melt at the run temperature, which enveloped the sulfides. An aliquot of an aqueous solution was also added to the capsule to generate a volatile phase, followed by another small sample (< 1 mg) of andesitic powder to reduce evaporation by trapping the solution within pore spaces. The capsule was frozen using dry ice and arc-welded. Using dry ice helped prevent the loss of volatiles from the short (12–15 mm) capsules during

welding, reduced the formation of frost on the capsule between welds, and the presence of CO_2 helped prevent oxidation of copper in the alloy capsule (Figure 3-6).

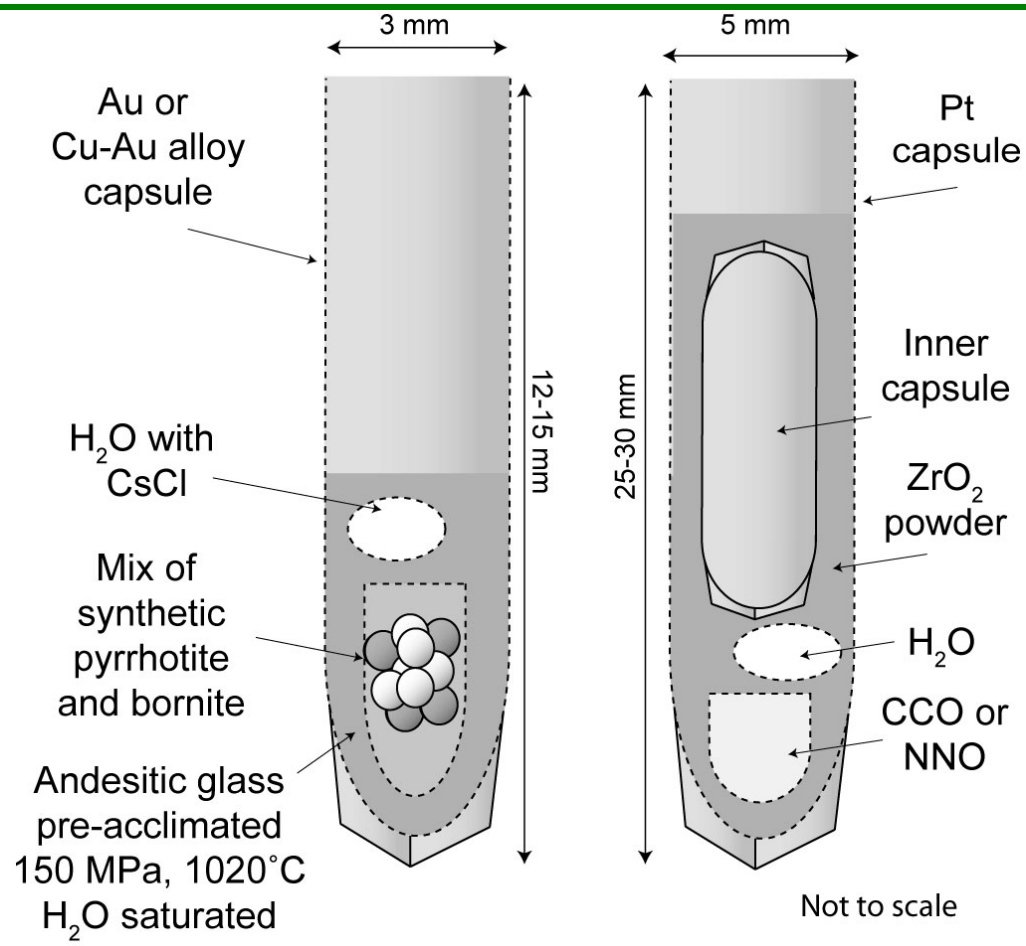

Figure 3-6 Design of the hydrothermal experiments
Construction of the capsules is illustrated in this cut-away diagram (final design). Left—The inner capsule is Au or Cu–Au alloy (Cu plated and annealed), 3 mm OD x 12–15 mm length. Pre-acclimated powdered glass is packed into base. Sulfides are loaded into a depression in the powdered glass and covered with more powdered glass. Aqueous solution is added to the powder, which is then packed down. The capsule is frozen in dry ice and arc-welded. Dry ice also reduces oxidation during welding by displacing oxygen and water from the welding atmosphere. Right—The outer Pt capsule (5 mm OD x 25–30 mm length) is used to prevent contamination of the pressure vessel by melting out of the inner capsule. ZrO_2 powder is packed in the base. Co or Ni+NiO is added in a depression and covered. Distilled water is added, covered and the charge packed down. More ZrO_2 powder is loosely added and the inner capsule is inserted and covered. The charge is packed down a final time, and the capsule is frozen and arc-welded. The final capsule had minimal unfilled volume which preventing extensive deformation under pressure and aided the quench process.

The andesite was pre-acclimated to the run conditions (1000°C and 150 MPa). This was done to reduce the time needed for the system to reach equilibration. A sample of powdered andesite from Soufriere Hills, Montserrat (sample ID MVO 819 in Zelmer et al. 2003, sample provided by Steve Sparks) was loaded into a Au capsule along with sufficient water to reach water-saturation, and run for a duration of 24 hours. The glass was removed from the capsule and ground to a powder. The aqueous phase had 1.8 wt % NaCl equivalent, with Na:K equal to 1:1, and Na:H equal to 10:1. This solution was used to limit changes to the silicate melt during the experiment as it equilibrated with the volatile phase. Cesium has a low diffusivity relative to other 1+ ions in silicate melts (Mungall 2002b and references therein) and was added to the solution as CsCl (100 ppm Cs, final) to evaluate whether metals in the system could reach homogeneity within the melt within the run duration.

Oxygen fugacity was controlled in the experiments in two ways: a capsule-in-capsule application of the metal–oxide buffer method, and a mixed Ar–H_2 pressure medium. The capsule containing the experimental charge was placed inside a platinum capsule (5 mm OD x 25–30 mm length). The space created between the capsule walls was used to house a Ni–NiO or Co–CoO buffer assemblage and distilled water. The oxygen fugacity of the inner capsule equilibrated by hydrogen diffusion through the capsule wall with the outer capsule, in which fO_2 was fixed by the buffer assemblage. Hydrogen permeation through the outer capsule wall would result in a loss of hydrogen to the pressure vessel, consuming buffering capacity. To prevent this loss, a mixture of Ar and H_2 calibrated to reproduce the H_2 fugacity of the buffer assemblage was used as the pressure medium.

Nickel and cobalt in the buffers alloy with gold, which could lower its melting point below the temperature of the experiments. To avoid this failure mode, the buffers were separated from the inner capsule. In early experiments (run numbers 85 and 86), the buffers were packed in separate 3 mm capsules (Pt), which were crimped but not welded shut, and placed in the bottom of the 5 mm Pt outer capsules. The Pt outer capsule was also used to contain the products of any accidental melting to prevent damage to the MHC vessels, but in some experiments the Au and Pt capsules 'welded' at contact points creating a new problem (Figure 3-7). The solution to this was to lightly 'flour' the outer surface of the inner capsule with ZrO_2 powder, which was sufficient to prevent contact and welding. This was successful, and prompted a change to the buffer set-up used that omitted the extra Pt capsule. The bottom of the Pt outer capsule was filled with ZrO_2 powder in which a depression was formed, which was in turn filled with the buffer assemblage. An aliquot of distilled water was added (see Table 3-4), more ZrO_2 was added, the inner capsule was inserted into the loose powder, and a final measure of ZrO_2 was added before freezing and welding as described above. This method separated the capsules and the buffer assemblage, and resulted in a more predictable and less severe deformation of the outer capsule under hydrostatic pressure due to the reduction of unfilled volume. The less-deformed capsule survived intact more frequently. The additional mass may also have helped the capsule to fall during quench.

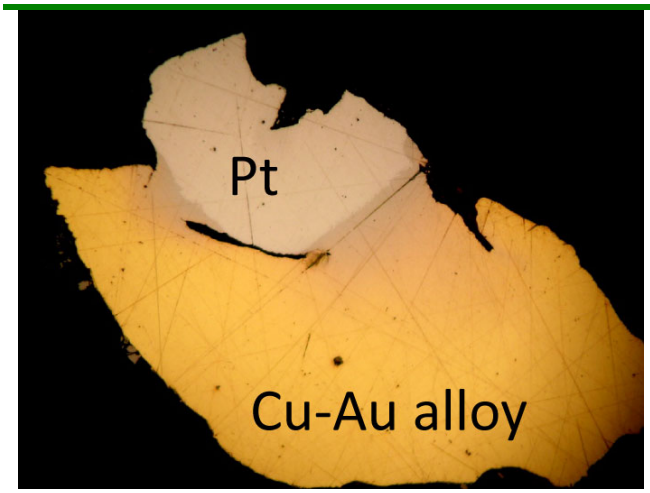

Figure 3-7 Spot welding during an experiment
In this photomicrograph of a section of capsule material from run 80 (view approximately 1 mm) the Cu–Au alloy inner capsule has spot-welded to the Pt outer capsule. This did not cause a failure, but made removal of the inner capsule difficult. Note that where there is any separation of the metals, there is no welding. In order to prevent contact between the metals in later runs powdered ZrO_2 was added first as a thin coating on the surfaces of the metals and later packed around the inner Cu–Au alloy capsule.

Initial consideration of the Cu–Fe–S phase diagram (Kullerud 1968) suggested ~6 wt % Cu might be expected in pyrrhotite in equilibrium with CFSL. Concentrations of copper in pyrrhotite from early experiments were approximately 3–5 wt %. Since the pyrrhotite starting material has 0.04 wt % Cu, it is reasonable to question whether there had been sufficient time for copper to fully diffuse into pyrrhotite from the CFSL and reach equilibrium. A reversal experiment, run 103, was designed to test this. Rather than starting with pyrrhotite and CFSL, run 103 started with pyrrhotite with 6 wt % Cu, which then formed pyrrhotite with ~4.5 % Cu and CFSL during the experiment (Figure 3-8). In most other respects, run 103 replicated run 85, with the exception of the sulfide starting materials (Run 103 was also performed at fO_2 equal to the NNO buffer, while run 85 was performed at fO_2 equal to the CCO buffer, but that was not a factor in this comparison). Prior to being used in run 103, the sulfide starting materials (pyrrhotite and bornite) were loaded into a silica tube, sealed under vacuum, and heated to 1000°C. Multiple replicate charges were prepared in the same silica tube, similar to the arrangement in Figure 3-4. One of the prepared charges was examined for evaluation of the phase assemblage

and major element chemistry. Another prepared charge was used in a hydrothermal experiment, which otherwise adhered to the experimental protocol described above.

Run products from experiment 103 (6 hour run duration) are compared to runs 85 and 86 (4 hour run durations) in Figure 3-8. Following heating in the silica tube, the starting materials had formed a single sulfide phase—pyrrhotite—with ~ 6 wt % Cu as expected. Pyrrhotite is anisotropic and shows extinction with rotation of the stage under cross-polarized light, while quenched liquids would not show a preferred alignment of crystalline phases formed on quench. Examination of the run products under cross-polarized light revealed only pyrrhotite. After subsequently being run in a hydrothermal experiment (run duration 6 hours), the sulfide run products consisted of pyrrhotite with ~4.5 wt % Cu and CFSL. As the phase compositions in the run products of this reversal experiment were identical to those in the previous hydrothermal experiments (Figure 3-8), I conclude that those must have reached equilibrium as well. Although the initial design was found to be satisfactory, the preparation step was added to subsequent runs to reduce dispersion of the sulfide charge within the silicate melt during the experiment. This is indicated by 'silica prep' in Table 3-4.

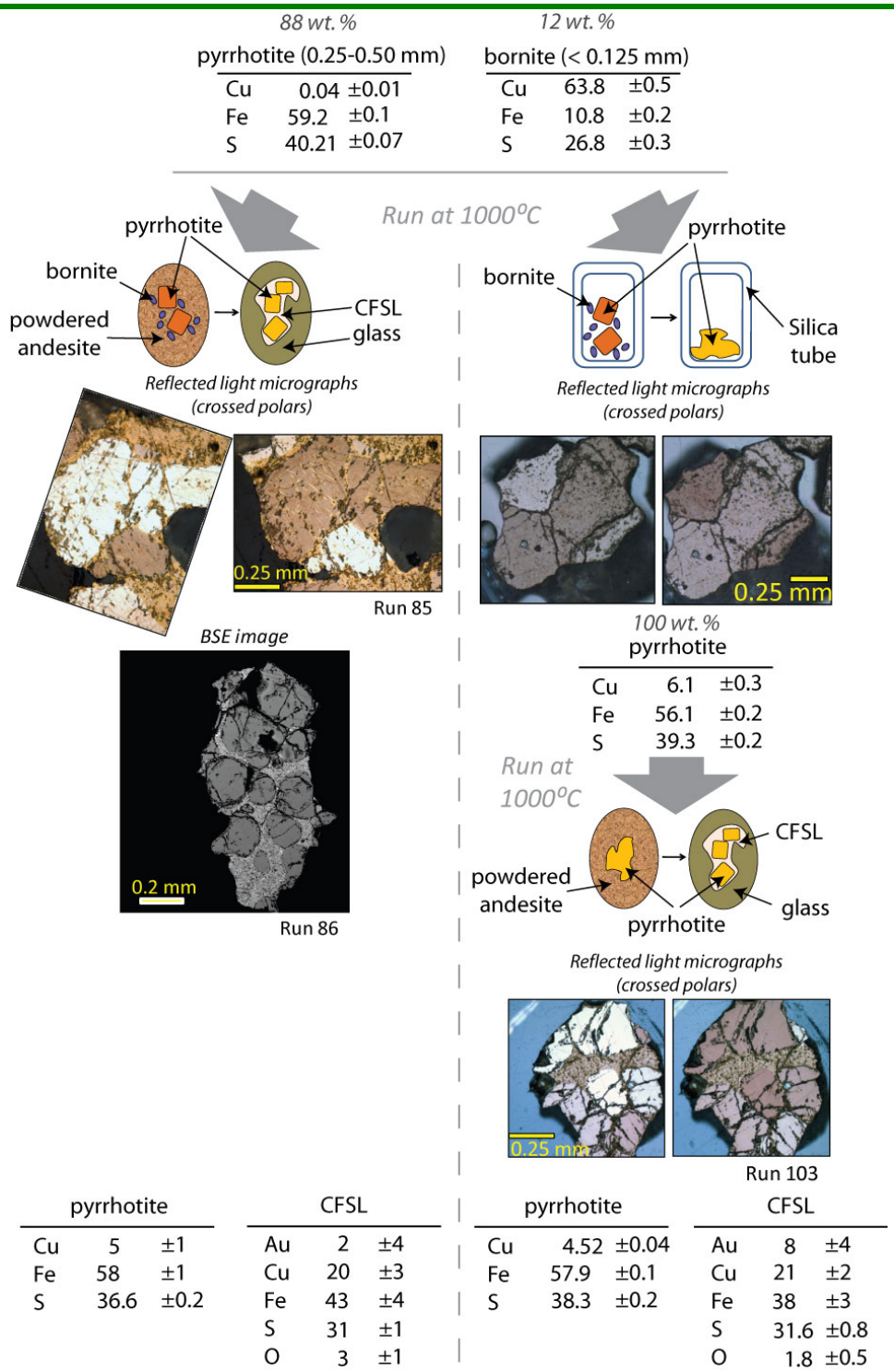

Figure 3-8 Reversal experiment
Comparison of run products from runs 85 (left) and 103 (right). Backscatter electron image is from run 86, which was similar to run 85. Pyrrhotite and bornite were added to run 85—the concentration of copper in pyrrhotite rose to 4.3 %, and the bornite transformed into CFSL (4 hour duration). Only pyrrhotite with 6 wt % Cu (prepared in a separate silica tube experiment) was added to run 103—pyrrhotite with 4.5 wt % Cu and CFSL was produced (6 hour duration).

3.3.4 Furnace assembly

The experiments performed using sealed evacuated silica tubes (runs 116a–b, 117a–b, and 118a–b) were wired together and suspended next to two type–K thermocouples in a vertical tube Deltech furnace (Figure 3-9) and brought to 1000°C. The tips of the thermocouples were offset such that one was at the base of the silica tubes, and the other was 20 mm higher. The difference in temperature between the two thermocouples was 5°C. Temperature variation due to heating cycles was ± 3°C. The silica tubes were held at temperature for >20 hours and drop-quenched in a water bath.

Figure 3-9 Laboratory equipment
(Top–this page) The silica tube experiments were heated in a vertical tube furnace (left) and drop- quenched into a water bath (not shown).

Figure 3-9 (middle) For hydrothermal experiments, an inner capsule of Au or Cu–Au alloy was placed inside a platinum capsule (30 mm length in picture). The combined capsule was placed inside a TZM or MHC (lower grey tube in picture) pressure vessel which was placed within an Inconel alloy sheath (top tube) which was flushed with argon to prevent oxidation of the pressure vessel. Water cooling kept the Al–Ni Bronze fitting and Cu–Al connector at ~20°C for a rapid quench.

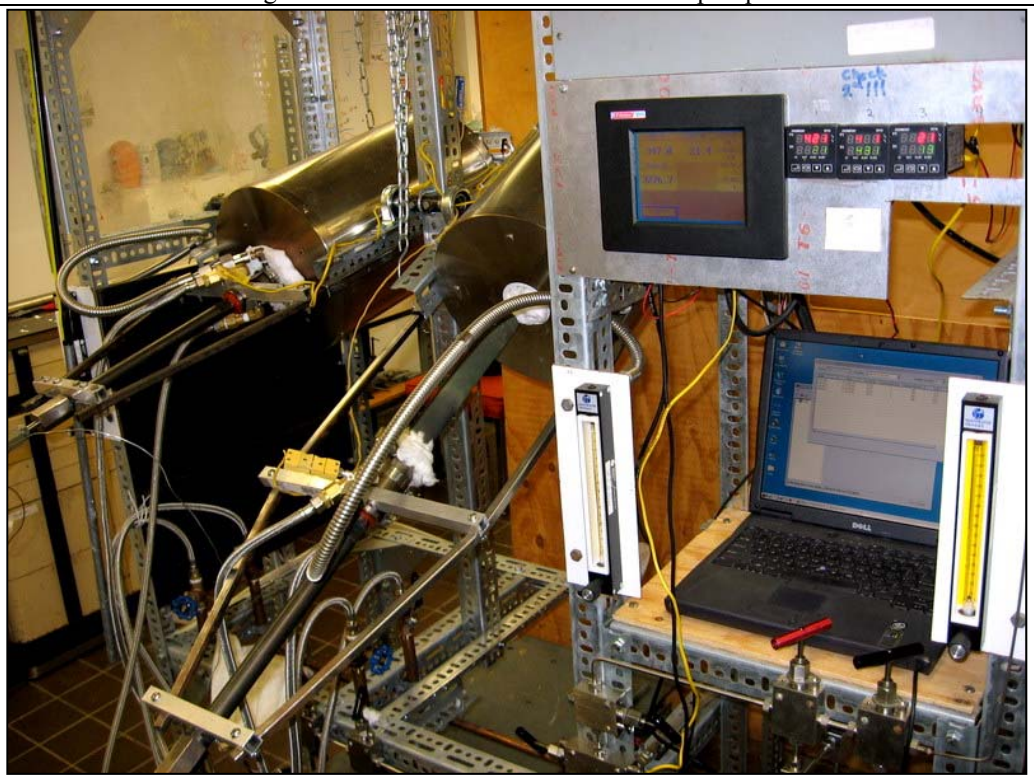

Figure 3-9 (bottom) Pressure vessels are shown inserted into furnace for heating (left) and retracted for loading and inspection (right). Furnace and pressure vessels rotate together to allow the capsule to fall to the water-cooled end of the vessel for rapid quenching. Also shown: temperature controllers, the monitoring and recording system for temperature and pressure sensors, tubing for low-pressure argon flushing, tubing for high-pressure Ar–H_2 pressure medium, and connectors for water cooling system. Power control system not shown.

Experiments 85 and 86 were run in a TZM (Titanium–Zirconium–Molybdenum) cold-seal pressure vessel equipped with a water-cooled rapid-quench extension, using argon as a pressure medium (Figure 3-9, middle). The remaining experiments were run in a MHC (Molybdenum–Hafnium-Carbide) vessel, using an Ar–H_2 pressure medium. The Ar–H_2 mixture was calibrated to extend the life of the solid oxygen fugacity buffers. A nickel alloy sheath (Inconel 600), flushed with argon, prevented oxidation of the pressure vessels under run conditions (Figure 3-9, bottom). The vessels were placed in a tube-type furnace at an angle of 12 degrees from horizontal to suppress convection within the pressure medium. The thermal gradient over the length of the inner capsule was measured with internal thermocouples to be ≤ 10°C for all samples. Quench was performed for experiments in the TZM by withdrawing the vessel from the furnace, raising it to vertical, and agitating it to help the capsule to fall. For experiments in the MHC vessels, the entire vessel and furnace assembly was rotated to a vertical position and agitated, allowing quench without first removing the vessel (Figure 3-9, bottom). Furnaces used either wire-coil type (Kanthal wire) or silicon-carbide heating elements. Except for some early runs, pressure during quench was monitored. A successful quench was accompanied by a small spike in pressure (~500–1000 psi).

It was found to be useful to add very small amount of zirconia 'flour' to the outer surface of the capsule prior to loading in the pressure vessel to help insure a rapid quench at the termination of the experiment. The capsule fell only partway to the cold end of the vessel in some early experiments requiring longer (approximately 3 minutes, as opposed to ~1–5 second) for the contents of the experiment to cool.

The use of 'flour' to prevent the two capsule metals from interacting (section 3.2.3) suggested a similar benefit here. $ZrSiO_4$ powder was dusted onto the outside of the capsule before insertion into the MHC pressure vessel to prevent any interaction between the capsule and the wall of the pressure vessel. Ultimately, the problem of the capsule failing to fall and properly quench at the termination of the experiments was eliminated by employing the new buffer design, a more massive capsule, and the $ZrSiO_4$ powder.

3.3.5 Sample processing

Following quench, the silica tubes were dried and examined for signs of failure (e.g., cracks, discoloration, distortion of light, or frosting on the interior). The capsules were scored with a thin diamond cutting blade on a Dremel multi-purpose tool, partially through the wall but not fully into the central chamber. A thin piece of metal was inserted into the cut and gently tapped. This propagated a crack through the remainder of the thickness of the tube without potentially disturbing the contents, which were removed and the process repeated for each chamber.

The run products were then mounted in epoxy and polished for analysis. In an attempt to reduce potential attenuation of X-rays during analysis of oxygen, the samples were mounted in a conductive epoxy (and not subsequently coated with carbon). Struers 'EPOES Epofix Resin' and 'EPOAP Epofix Hardener' were used with a Buehler Ni based conductive filler (208500S). Run products were placed in holes in a small aluminum disc at the bottom of a 1" rubber mould and covered with the epoxy mixture.

Capsules from the hydrothermal experiments were removed from the pressure vessel following quench. The surface of the Pt outer capsule was examined for defects, cleaned, and weighed. Due to the gain or loss of hydrogen during the experiment, changes in weight on the order of 0.1 mg were expected, and common. Significantly larger changes would be an indication of failure. The outer capsule was then punctured, and the presence of fluid was noted, along with any sulfurous smell that would indicate failure of the inner capsule. The buffer assemblage, now in the form of a compressed pellet, was removed along with the inner capsule. The inner capsule was cleaned and weighted. The capsule was punctured and opened, and the contents removed. In general, the glass largely or completely enveloped the sulfide contents. The glass bead was carefully cracked open. Sulfides were loaded into a mold and mounted in epoxy. Some sulfides were mounted in conductive epoxy, as described above. Pieces of the glass were mounted separately, in an effort to limit potential transfer of metals from the sulfides to the glass during polishing.

Polishing was performed with 400 and 600 grit sandpaper, followed by 15 μm, 6 μm, 3 μm, 1 μm, and ¼ μm diamond pastes (from Buehler or MTI Corporation). Samples were washed and placed in an ultrasonic bath between each polishing step.

3.4 Analytical methods

3.4.1 Reflected light microscopy

Photomicrographs of samples were taken with a binocular microscope, and a reflected light petrographic microscope in the microscopy lab of Aaron Martin and Sarah Penniston–Dorland at the University of Maryland. Images were used as maps for further analysis, and as a record of the surface appearance. Cross-polarized light images help in these samples to distinguish crystalline solids such as pyrrhotite, which is anisotropic, from quenched sulfide liquids where the fine-grained mixture of minerals formed on quench (pyrrhotite and chalcopyrite or chalcopyrite and bornite) do not share a common optical alignment.

3.4.2 EPMA

Electron probe microanalysis (EPMA) was performed at the University of Maryland Nanoscale Imaging Spectroscopy and Properties laboratory (NISP), using a JEOL JXA–8900 Superprobe. Samples were examined with backscatter electron (BSE) imaging. Phase identification was aided by energy dispersive spectroscopy (EDS) and semi-quantitative EDS. Wavelength dispersive spectrometry (WDS) was used to determine major, minor, and trace element concentrations.

3.4.2.1 Glass

Run-product glasses (quenched silicate melt) were analyzed first for major oxides using an accelerating voltage of 15 kV, and a beam current (cup) of 5 nA. The beam was defocused to a 20 μm diameter spot size. The ZAF algorithm was used in the conversion of raw X-ray fluxes to concentrations. The following standards were

utilized: Peninsula Albite CA (USGS FSTA); Kakanui hornblende, New Zealand (USNM 143965); Yellowstone rhyolite, WY (USNM 72854 VG–568); MPI–Ding Mt. St. Helens andesite (6/80); Indian-Ocean basalt (USNM 113716); and Scapolite (Meionite), Brazil (USNM R–6600–1(4)). Subsequent analysis for S and Cl was performed at 15 kV, 50 nA, and a 20 μm spot size using scapolite (Meionite), Brazil (USNM R–6600–1(4)) as a S and Cl standard, with the PRZ algorithm. It has been well demonstrated (e.g., Carroll and Rutherford 1985) that the sulfur peak position shifts with oxidation state of the sulfur. During standardization, sulfur peak positions were determined for scapolite (oxidized sulfur) and pyrrhotite (reduced sulfur). The peak position for sulfur from pyrrhotite was used for the analysis of the run products to prevent undercounting due to the dominance of S^{2-} in the sample glasses.

3.4.2.2 Sulfides

Run-product pyrrhotite, CFSL, and bornite were analyzed by electron probe microanalysis generally following the protocol defined by Mengason et al. (2010). An accelerating voltage of 20 kV, beam current (cup) of 50 nA, and a 20 μm spot size, were utilized. Concentrations were calculated using the ZAF algorithm. Standards used for X-ray intensities included: SRM–482E Au–Cu wire (20 % Au, 80 % Cu by weight); Astimex chalcopyrite; Santa Eulalia pyrrhotite, Mexico (USNM R7570); and magnetite from Essex NY. For pyrrhotite analyses, the pyrrhotite standard was used for iron and sulfur. For all other analyses, the chalcopyrite standard was used for iron and sulfur. Magnetite was used as the oxygen standard.

It has been noted previously (e.g., Naldrett 1969, Mengason 2007) that sulfide liquids do not quench to a glass, but rather to a mixture of intergrown solid phases.

The grain size of this mixture is related to the rapidity of the quench, and may also be affected by the identity of the apparent low-temperature phases involved. In these samples the diameters of the grains in the quenched phases were on the order of 1–5 microns. The quenched sulfide products from samples 117a–b appeared slightly coarser, which may be related to the construction of the experiment. To a lesser extent, pyrrhotite may also exsolve bands of chalcopyrite during quench. Individual analytical volumes contain a mixture of phases. As an estimate of the CFSL, the average and standard deviation of multiple analyses are reported. The uncertainty reported is strongly influenced by quench processes, and may considerably overestimate heterogeneity present in the phases at run conditions.

3.4.3 LA–ICP–MS

LA–ICP–MS was performed at the Plasma Mass Spectrometry Laboratory at the University of Maryland, using a New-Wave solid-state Nd:YAG laser with a wavelength of 213 nm for sample ablation, and an Element 2 single collector magnetic sector ICP–MS for analysis. For analysis of glass run-products, ^{43}Ca (total Ca determined by EPMA) was used as an internal standard with NIST 610. For analyses of sulfide run products, ^{63}Cu was used as an internal standard with NIST 610.

Analysis of sulfides by LA–ICP–MS is complicated by the lack of availability of quality sulfide standards. The method chosen for these analyses compared well to the use of ^{57}Fe with NIST 610, or ^{63}Cu with a sample of the iron meteorite Filomena. Concentrations presented in this study were calculated using NIST 610, with ^{63}Cu

(Cu in sulfides determined by EPMA) as the internal standard. A sample of pyrrhotite was synthesized with elevated Cu, Ag, Au and Mo in order to compare the effectiveness of these methods for this and future studies. Analysis of the new pyrrhotite standard, as well as a sulfide standard provided by James Brennan, yielded consistent concentrations between methods for Cu, Fe, Mo, Ag, and Au. In a review of a subset of analyses of run products, variation among individual laser spots from the same material was generally greater than the difference between the quantification methods.

Analysis of the sulfide run products was also complicated by variation in the size of pyrrhotite grains and quenched sulfide liquid globules. Spot size was tailored to available areas for analysis. The minimum spot size used was 8 μm, and the maximum was 50 μm. Laser repetition rate and power output were adjusted accordingly. Power density ranged from 1 to 3 joules per cm^2. As noted for EPMA analyses, the uncertainties reported for the sulfide phases are strongly influenced by exsolution during quench in pyrrhotite, and the formation of a mixture of phases during quench of the CFSL.

Many of the glasses analyzed had small sulfides distributed throughout the glass. Sulfides apparent in BSE images were small, generally on the order of 1–2 microns. Others were identifiable by LA–ICP–MS signal, but too small to be visible in BSE images. Apparent sulfides were avoided. And, as determined on the time resolved spectra, regions of clear sulfide signal were removed from glass analyses. The presence of sulfide in the analytical volume generally elevated copper and gold together, with gold signal intensity increasing two or more orders of magnitude. This

is greater that would be expected by gold 'nugget' formation, and in that case, copper would not be expected to co-vary. Spot size was adjusted to reduce the frequency of signals with inclusions, as a smaller diameter beam is less likely to intercept sulfides. Spot sizes ranged from 15 μm to 50 μm, though analyses were generally conducted in the range of 25–45 um. A test performed using the basalt standard BIR–1 showed that accurate values could be determined across a range of spot sizes while the external standard is measured with a single spot size.

3.5 Results

3.5.1 Silica tube experiments

Run products from the silica tube experiments have been examined and analyzed to determine the phase assemblage, sulfur and oxygen fugacity, major and trace element concentrations, and to calculate partition coefficients among the phases present. Upon completion of the experiment, inspection of the silica tubes did not reveal cracks or other signs that the tubes failed to isolate the experimental charge. In general, all of the experiments appear to have survived intact.

In outward appearance, the starting materials from chambers 1 and 3 (which initially contained pyrrhotite and bornite) had fused into a single mass with a smooth, rounded appearance. In places, the surface of the charge followed the curvature of the inner surface of the tube. In polished section they revealed crystalline pyrrhotite surrounded by CFSL. The Cu–Au alloy remained intact in samples 117a and 117b, and was also surrounded by CFSL. The alloy was found as globules throughout the

charges of the other experiments. The composition of the 'sensor' pyrrhotite (table 3-6), was used to calculate sulfur fugacity (Toulmin and Barton 1964) for all experiments, and oxygen fugacity (Whitney 1984) for experiments 117a–b where the sensor pyrrhotite was in contact with magnetite. Trace concentrations of Cu and Au in the pyrrhotite were treated in the manner of Mengason et al. (2010). Propagated uncertainty from microprobe analyses gives an uncertainty in log fS_2 of ~0.3 (bar). This is comparable to, but slightly smaller than, the overall uncertainty of the Toulmin and Barton (1964) technique in log fS_2 of ~0.35 (bar).

Table 3-6 Compositions of sensor pyrrhotite from silica tube experiments

	Cu			Fe			S			Au				
	wt %	*1σ*	*n*	wt %	*1σ*	*n*	wt %	*1σ*	*n*	ppm	*1σ*	*n*	log fS_2	log fO_2
r116a	0.07	*0.02*	*8*	61.3	*0.3*	*8*	39.5	*0.1*	*8*	600	*200*	*8*	0.0	-
r116b	0.43	*0.01*	*8*	61.3	*0.2*	*8*	39.3	*0.2*	*8*	400	*100*	*8*	-0.3	-
r118a	0.01	*0.01*	*7*	61.7	*0.3*	*7*	38.7	*0.1*	*7*	100	*100*	*7*	-0.9	-
r118b	0.02	*0.01*	*8*	62.0	*0.2*	*8*	38.5	*0.2*	*8*	200	*200*	*8*	-1.3	-
r117a	0.14	*0.01*	*8*	61.8	*0.2*	*8*	38.6	*0.1*	*8*	100	*100*	*8*	-1.1	-10.1
r117b	0.05	*0.01*	*10*	62.6	*0.2*	*10*	38.0	*0.2*	*10*	100	*100*	*10*	-2.4	-11.1

Analysis by EMPA. fS_2 calculated from pyrrhotite composition following Toulmin and Barton (1964) and Mengason et al. (2010). fO_2 calculated following Whitney (1984).

The primary goal of these silica tube experiments was to investigate differences in major element concentrations in pyrrhotite and CFSL in the Cu–Fe–S system versus the Cu–Fe–S–O system under both alloy-undersaturated, and alloy-saturated, conditions. Concentrations of major and trace elements in pyrrhotite and CFSL run products are listed in Table 3-7. In terms of this goal, a few first-order observations are apparent. In the alloy-undersaturated experiments, the concentrations of copper in pyrrhotite from the Cu–Fe–S system (116a–b and 118a–b: average 5.5 ± 0.4 wt %) were greater than in those from the Cu–Fe–S–O system (117a–b: average 3.7 ± 0.3 wt %). In the alloy-saturated experiments, the concentrations of copper in pyrrhotite for both systems were, on average, approximately 20% lower and following the same relationship as in the undersaturated experiments (116a–b and 118a–b: average 4.5 ± 0.3 wt %; 117a–b: average 2.9 ± 0.3 wt %). These results suggest that the concentration of copper in the pyrrhotite from the Cu–Au alloy saturated hydrothermal experiments should be somewhat lower than those indicated in the Cu–Fe–S phase diagrams constructed based on metal-absent experiments.

In a manner similar to pyrrhotite, the average concentration of copper in the CFSL in the system Cu–Fe–S (32 ± 4 wt %) is greater than in the system Cu–Fe–S–O (18 ± 4 wt %) in alloy-undersaturated samples. Average concentration of copper in CFSL in the system Cu–Fe–S (26 ± 3wt %) is greater than in the system Cu–Fe–S–O (1 sample = 5 wt %) in alloy-saturated samples. The lower concentration of copper in CFSL (alloy-undersaturated, Cu–Fe–S–O system), was accompanied by the addition

of ~4 wt % oxygen. An inverse relationship between copper and oxygen concentrations in sulfide liquids was also reported by Ripley (2002).

The majority of the hydrothermal experiments in this study are not magnetite-saturated and have concentrations of FeO in the silicate melt less than that of magnetite saturated experiments. It is likely that these magnetite-undersaturated hydrothermal systems are intermediate in terms of a_{FeO}^{CFSL} between the two extremes investigated in the silica tube series of experiments (oxygen-free and magnetite saturated) and might therefore be expected to have intermediate behavior in characteristics related to a_{FeO}^{CFSL} such as partition coefficients.

Another goal of the silica-tube experiments was to evaluate the range of gold concentrations that should be expected in the CFSL in experiments performed in gold alloy capsules. It is clear from inspection of the data in Table 3-7 that the concentration of gold in copper–gold alloy-saturated experiments varied greatly, from 800 ppm to 14 wt %. It should be noted that wt % can be a misleading representation of a phase consisting largely of Au, Cu, and Fe, given the difference in their atomic weights. The fraction of gold in CFSL in these experiments is much less than copper on a per-mole basis. It is also apparent that gold concentration directly correlates with sulfur fugacity (Au decreases by ~500 ppm as log fS_2 is reduced by ~3.0 – Figure 3-12). A thermodynamic explanation for this trend is presented in section 3.5.7.

Table 3-7 Compositions of pyrrhotite and CFSL run products from silica tube experiments

	Cu			Fe			S			O			Mo			Ag			Au			Total
	wt %	*1σ*	*n*	wt %	*1σ*	*n*	wt %	1σ	n	wt %	1σ	n	ppm	1σ	n	ppm	1σ	n	ppm	1σ	n	
												Pyrrhotite										
r116a	5.3	*0.2*	*10*	56.9	*0.3*	*10*	38.6	*0.2*	*10*	-	-	-	70	*10*	*4*	94	*9*	*4*	56	*9*	*4*	100.9
r116b	6.09	*0.07*	*9*	56.4	*0.2*	*9*	38.4	*0.1*	*9*	-	-	-	90	*30*	*6*	40	*20*	*5*	31	*9*	*6*	101.0
r118a	5.6	*0.2*	*7*	57.5	*0.2*	*7*	37.7	*0.2*	*7*	-	-	-	58	*3*	*6*	51	*4*	*6*	14	*3*	*6*	100.9
r118b	5.10	*0.07*	*10*	57.8	*0.4*	*10*	37.8	*0.2*	*10*	-	-	-	67	*5*	*6*	42	*7*	*6*	9	*1*	*6*	100.7
r117a	3.9	*0.2*	*8*	59.7	*0.3*	*8*	37.4	*0.2*	*8*	-	-	-	60	*10*	*5*	30	*20*	*5*	7	*2*	*5*	101.0
r117b	3.6	*0.1*	*7*	59.7	*0.1*	*7*	37.2	*0.1*	*7*	-	-	-	92	*9*	*6*	50	*20*	*6*	13	*3*	*6*	100.5
												Pyrrhotite (Cu–Au alloy saturated)										
r116a	4.1	*0.1*	*8*	57.4	*0.4*	*8*	38.9	*0.2*	*8*	-	-	-	-	-	-	-	-	-	1400	*500*	*8*	100.6
r116b	4.25	*0.08*	*7*	57.7	*0.2*	*7*	38.69	*0.06*	*7*	-	-	-	-	-	-	-	-	-	1600	*300*	*7*	100.8
r118a	4.65	*0.04*	*8*	58.1	*0.2*	*8*	38.17	*0.08*	*8*	-	-	-	-	-	-	-	-	-	400	*200*	*8*	101.0
r118b	4.8	*0.3*	*7*	58.1	*0.2*	*7*	37.9	*0.1*	*7*	-	-	-	-	-	-	-	-	-	300	*200*	*7*	101.0
r117a	2.8	*0.8*	*12*	60.0	*0.8*	*12*	37.9	*0.2*	*12*	-	-	-	-	-	-	-	-	-	200	*300*	*12*	100.6
r117b	3.1	*0.2*	*8*	59.8	*0.7*	*8*	37	*2*	*8*	-	-	-	-	-	-	-	-	-	200	*100*	*8*	99.9
												Quenched Cu–Fe–S–(O) liquid										
r116a	29.2	*0.8*	*7*	35.5	*0.6*	*7*	32.6	*0.4*	*11*	-	-	-	18	*8*	*4*	9000	*2000*	*4*	12000	*2000*	*2*	99.4
r116b	33	*2*	*11*	34	*1*	*11*	35	*1*	*11*	-	-	-	40	*40*	*2*	3000	*1000*	*4*	4000	*2000*	*4*	102.6
r118a	30	*2*	*7*	36	*2*	*7*	32.9	*0*	*7*	-	-	-	11	*4*	*5*	4300	*400*	*5*	2700	*300*	*5*	99.4
r118b	37	*6*	*12*	32	*4*	*12*	31	*1*	*12*	-	-	-	13	*3*	*6*	3300	*900*	*6*	1700	*600*	*6*	100.0
r117a	20	*10*	*9*	47	*9*	*9*	31.0	*1*	*9*	3	*2*	*9*	10	*10*	*4*	1700	*900*	*4*	700	*200*	*4*	101.9
r117b	15	*8*	*10*	50	*8*	*10*	29.2	*1*	*10*	5	*2*	*10*	31	-	*1*	2100	*300*	*4*	1300	*900*	*4*	99.7
												Quenched Cu–Fe–S–(O) liquid (Cu–Au alloy saturated)										
r116a	23	*4*	*12*	33	*1*	*12*	32.3	*1*	*12*	-	-	-	-	-	-	-	-	-	130000	*50000*	*12*	101.8
r116b	25	*1*	*7*	32	*3*	*7*	31	*2*	*7*	-	-	-	-	-	-	-	-	-	140000	*70000*	*7*	102.3
r118a	25	*1*	*12*	36	*3*	*12*	32	*1*	*12*	-	-	-	-	-	-	-	-	-	80000	*50000*	*12*	101.9
r118b	31	*5*	*7*	34	*2*	*7*	31.5	*0*	*7*	-	-	-	-	-	-	-	-	-	40000	*40000*	*7*	100.5
r117a	-	-	-	-	-	-	-	-	-	-	-	-	-	-	-	-	-	-	-	-	-	
r117b	5	*2*	*8*	59	*2*	*8*	29	*1*	*8*	7	*1*	*8*	-	-	-	-	-	-	800	*600*	*8*	99.6

Cu, Fe, S, and O by WDS. * indicates analysis by WDS, all other values for Mo, Ag, and Au by LA–ICP–MS.

3.5.2 Hydrothermal experiments

Run products from the hydrothermal experiments have also been inspected and analyzed as described above. Run times, oxygen and sulfur fugacities, and the sulfur concentrations of the run-products are listed in Table 3-8. Pyrrhotite, and quenched CFSL and silicate melt were recovered for all experiments except 114. Experiment 114 was designed to have pyrrhotite as the only stable sulfide phase for comparison. Experiment 124 was run at lower temperature (900°C) than the other experiments, also for comparison. Although pyrrhotite and intermediate-solid-solution (*iss,* $CuFeS_2$) were expected as sulfide run products based on previous work in the Cu–Fe–S system, the Cu-rich sulfide contained ~ 2 wt % oxygen, and was likely a liquid at run temperatures. Bell (2009) report forming a CFSL at NNO, 150 MPa, and 800°C, which is a temperature even lower than used here. Sulfur concentration at sulfide saturation (SCSS) in quenched silicate melt varies, but in general increases with fS_2, and fO_2 as expected based on previous data (e.g., Carroll and Rutherford 1985, Mavrogenes and O'Neill 1999, Wallace and Carmichael 1994, Jugo et al. 2005, Li and Ripley 2005, 2009, Liu et al. 2007, Jugo 2009).

Table 3-8 Run conditions of hydrothermal experiments

		Run	log fS_2		log fO_2		silicate melt		pyrrhotite		CFSL			
Run #	Buffer	time (h)	(bar)	*1σ*	(bar)	ΔNNO	**S ppm**	*1σ*	**S wt %**	*1σ*	**S wt %**	*1σ*	**O wt %**	*1σ*
85	CCO	4	-3	*2*	-11.8	-1.6	**340**	*80*	**36.6**	*0.2*	**31**	*1*	**3**	*1.2*
86	CCO	4	-1.8	*0.6*	-11.8	-1.6	**330**	*60*	**37.1**	*0.2*	**31.7**	*0.7*	**2.4**	*0.4*
109	CCO	6	-1.4	*0.2*	-11.8	-1.6	**210**	*40*	**37.5**	*0.1*	**29.4**	*0.8*	**2.9**	*0.5*
121	CCO	24	-1.4	*0.4*	-11.8	-1.6	**220**	*20*	**37.1**	*0.2*	**30.1**	*0.6*	**2.1**	*0.2*
124*	CCO+ (mt)	19	-1.9	*0.4*	-9.5‡	2.4	**160**	*40*	**36.4**	*0.2*	**29.2**	*0.4*	**2.4**	*0.3*
92	NNO	18+6	0.	*1*	-10.2	0	**360**	*20*	**38.0**	*0.6*	**32.2**	*0.8*	**1.6**	*0.3*
94	NNO	18.5	-0.1	*0.8*	-10.2	0	**790**	*90*	**38.2**	*0.4*	**33.8**	*0.4*	**2**	-
100	NNO (mt)	6	-0.2	*0.3*	-10.2	0	**370**	*30*	**38.1**	*0.1*	**31.0**	*0.9*	**4.5**	*0.7*
102	NNO	6	-0.6	*0.3*	-10.2	0	**330**	*30*	**38.2**	*0.3*	**30.7**	*0.9*	**2.5**	*0.2*
103	NNO	6	-0.3	*0.2*	-10.2	0	**200**	*40*	**38.3**	*0.2*	**31.6**	*0.8*	**1.8**	*0.5*
108	NNO	6	-0.2	*0.4*	-10.2	0	**400**	*10*	**38.3**	*0.1*	**31**	*2*	**2.2**	*0.7*
114	NNO	24	0.2	*0.3*	-10.2	0	**750**	*90*	**39.3**	*0.1*	**n/a**	*n/a*	**n/a**	*n/a*
120	NNO	24	-0.3	*0.2*	-10.2	0	**180**	*10*	**38.1**	*0.1*	**29.7**	*0.8*	**2.4**	*0.2*
125	NNO+	28	0.2	*0.2*	> -10.2	> 0	**590**	*50*	**38.5**	*0.1*	**29.3**	*0.6*	**2.1**	*0.4*
127	NNO+ (mt)	46	1.1	*0.3*	-8.2‡	2.0	**1800**	*200*	**39.2**	*0.1*	**29**	*1*	**0.6**	*0.2*

Log fS_2 determined from pyrrhotite composition (Toulmin and Barton 1964, Mengason et al. 2010). Log fO_2 determined from buffer assemblage, except ‡ where log fO_2 was determined following Whitney (1984). CCO= Cobalt–Cobalt Oxide buffer used. NNO = Nickel–Nickel Oxide buffer used. + indicates that the buffer was fully oxidized, and that fO_2 was > the buffer assemblage. (mt) indicates magnetite present in the run.
* indicates 900°C instead of 1000°C. All concentrations measured using WDS.

Pyrrhotite composition has been used to calculate log fS_2 (Toulmin and Barton 1964, Mengason et al. 2010) and log fO_2 (Whitney 1984) for run 127 and 124, in which magnetite crystals grew during the experiment. Magnetite was not analyzed for titanium content, which can somewhat affect calculated fO_2. For all other experiments, fO_2 is based on the buffer assemblage. The presence of H_2S and SO_2 in the inner capsule lowers the fugacity of H_2O relative to the outer capsule which houses the buffer. The effect of H_2S and SO_2 on fO_2 calculated from buffer equilibria was investigated and found to be minimal based on thermodynamic data from Chase (1985). Calculations yielded a difference of <0.1 log units fO_2 between the inner and outer capsules. The post-run buffer charge for 124, 125, and 127 appears to be completely oxidized, by visual inspection and lack of attraction to a magnet. Full oxidation indicates that fO_2 in the experiment was greater than that of the metal/metal–oxide assemblage. The use of an Ar–H_2 pressure medium provides some constraint on this, and suggests that 125 was slightly above the buffer fO_2. The long run-time of 127 allowed greater hydrogen loss from the vessel, and therefore a substantially higher fO_2. The fO_2 of the buffer in run 124 (CCO) was lower than in runs with NNO buffers, which requires a higher partial pressure of hydrogen in the pressure medium, which induces a steeper gradient across the pressure vessel and therefore a greater rate of permeation and loss of hydrogen. As a result, the fO_2 of run 124 (19-hour run duration) is calculated to have risen to -9.5 log units (bar). Also listed in Table 3-8 are concentrations of sulfur in all of the phases studied, as well as the concentration of oxygen in the CFSL, for comparison.

It was initially considered desirable to have experiments at two or more sulfur fugacities for each oxygen fugacity buffer, to independently assess their effects on partitioning and solubility. However, the system responded to these conditions by changing the concentration of FeO in the silicate melt from the starting composition, and altering the composition and masses of the sulfide phases. In these experiments, fO_2 and fS_2 of run products are roughly correlated. The assemblage pyrrhotite + CFSL prevents fO_2 and fS_2 from varying independently to a significant degree in a manner similar to pyrrhotite + magnetite (Whitney 1984). Among the experiments, run 85 has the lowest fO_2 and fS_2, although the uncertainty on fS_2 for run 85 is high. Experiments 114, 125, and 127 have the highest fO_2 and fS_2. The other experiments fall roughly into two groups, NNO with log fS_2 ~ -0.5, and CCO with log fS_2 ~ -1.5. This experimental design only allowed fO_2 to be fixed. It would be interesting, in future experiments, to better model a system where the ongoing incorporation of reduced sulfur-bearing component forces the system to other conditions.

3.5.3 Equilibrium

In experiments of this type, it is important to consider whether or not sufficient time has elapsed for the aspects of the experiment under study to approach equilibrium. That includes the phase assemblage, the major element compositions of the phases, distribution of trace elements among the phases, as well as fO_2 and fS_2.

With regard to the overall duration of the experiments, it is useful to compare the current experiments with a similar system studied in Mengason 2007 (data from which are published in Simon et al. 2008 and Mengason et al. 2011). In that study, time series experiments were performed which contained pyrrhotite, magnetite, an

immiscible Fe–S–O liquid, a low water-content rhyolitic melt, and volatile phase at ~1040°C. Experiments were performed as series of replicates for 20-, 200-, or 2000-minute run durations. The effect of run duration on $D_i^{pyrrhotite\ /\ silicate-melt}$, $D_i^{Fe-S-O-liq\ /\ silicate-melt}$, and $D_i^{pyrrhotite\ /\ Fe-S-O-liq}$ for Cu, Mo, Ag, and Au was evaluated. All partition coefficients changed from initial ratios in the starting materials (duration = zero) to those of experiments of 20-minute run duration. All partition coefficients changed, but less so, between 20-minute duration and 200-minute duration experiments. Partition coefficients for Cu, Mo, Ag, and Au then remained constant between 200- and 2000-minute duration series. The fO_2 and fS_2 were determined from the composition of pyrrhotite in the presence of magnetite (Toulmin and Barton 1964, Whitney 1984) and remained constant between 200- and 2000-minute duration experiments. It was concluded that equilibrium had been closely approached in less than 200 minutes. Durations in the current study span from 240 minutes (4 hours) to 2940 minutes (49 hours).

Relative to Mengason (2007), there were several factors in the current study that made it difficult to perform replicate experiments as a time series. The experiments in this study were conducted close to the melting point of the Cu–Au alloy capsules. The capsules could be thinned in places by the loss of mass to sulfides in the experiment. The capsules were also deformed when placed under pressure. Longer run duration experiments were more therefore more likely to fail than shorter run duration experiments. In addition, the longest duration experiments (28 and 49 hours) exceeded the buffering capacity of the oxygen fugacity buffers due to loss of hydrogen from the pressure medium through the MHC vessel. However,

over the course of the study, runs were completed at similar conditions but different durations. Runs 86 (4 hours), 109 (6 hours), and 121 (24 hours) were performed at the same fO_2 (CCO) and fS_2 (~ -1.5: within uncertainty). Runs 102 (6 hours), 103 (6 hours), 108 (6 hours), 94 (18.5 hours), 92 (18 hours + 6 hours due to equipment failure), and 120 (24 hours) were performed at the same fO_2 (NNO) and fS_2 ~ -0.5: within uncertainty). In these two groups of experiments, partition coefficients changed significantly from initial ratios in starting materials, but correlations with duration were not identified. This was consistent with the finding of Mengason (2007).

As discussed previously, the equilibrium concentration of copper in pyrrhotite was studied in a reversal experiment which showed that a concentration of copper in pyrrhotite of ~4.5 % was arrived at from low- (0.04 wt %) and high-Cu (6 wt % Cu) bearing pyrrhotite, and pyrrhotite in runs of 4 and 6 hour durations, respectively. As a result of the adoption of the silica tube preparation step, approximately half of the experiments utilized pyrrhotite and bornite starting materials, and half had Cu-rich pyrrhotite formed by pre-reacting pyrrhotite and bornite in silicate tubes. Concentrations of copper in pyrrhotite reached homogeneity regardless which of these two methods was used. Relative standard deviations (RSD) of concentrations of copper in pyrrhotite among experiments in which pyrrhotite and bornite were added directly to the capsule fall into two groups: runs 85, 92, and 94 (average RSD of the concentration of copper in pyrrhotite = 28%, possibly due to slower quench times); and runs 86, 100, 102, and 104 (average RSD = 4%). In experiments in which pyrrhotite and bornite were allowed time to begin equilibrating at temperature in a

silica tube prior to the hydrothermal experiments, the RSD of concentrations of copper in pyrrhotite averaged 2.6%.

As a further test to determine if sufficient time was allowed for equilibration, a tracer was added to the volatile phase that then diffused into the melt during the experiment. Relative to other elements (e.g., Na, log D ~ -6 at 1000°C, Mungall 2002b), cesium diffuses slowly through silicate melts (log D ~ -10 at 1000°C, Mungall 2002b). Copper diffusion in silicate melts is not well known, but is likely intermediate between sodium and cesium. If cesium has reached homogeneity in the silicate melt within the durations of the experiments, then it is likely that sufficient time has elapsed for copper to do so as well. The concentration of cesium in the starting glass was < 1 ppm. The concentration of cesium in the aqueous solution that formed the volatile phase was 100 ppm. Cesium concentration in the run product glasses (quenched melt) averaged 35 ppm, and was homogenous within the silicate melt in all experiments, for all run durations (see values in Table 3.9). The greatest relative standard deviation (RSD) among concentrations of cesium in the run product glasses was only 19% (in an experiment conducted at 900°C), and the average was 10%. Again, if a slowly diffusing element such as cesium has had sufficient time to diffuse into the melt and reach homogeneous concentrations, it is likely that copper and the other ore metals studied here have as well.

3.5.4 Run product glasses

The compositions of run product glasses are listed in Table 3-9. All of the quenched melts are andesitic, and have changed little from the composition of the starting material with the exception of $FeO_{(total)}$, which varies among the samples.

The run product glasses from most experiments are nearly or completely crystal-free, with the exception of experiment 124, which was run at a lower temperature (900°C) than the other experiments detailed here. One additional observation of physical state of the run-product glasses worthy of note was dimpling on the surface of the glass where melt was in contact with the capsule wall, which has been interpreted in past studies as an indication of water-saturation. The H_2O content of the glasses is consistent with saturation by a water-rich phase. The concentration of water was determined by difference from the analytical totals and ranged from 4.1 % to 6.2 %, with an average of 5.6%.

Table 3-9 Compositions of glass run products from hydrothermal experiments

	CCO (1000°C, 150MPa)												CCO mt sat. (900°C)			NNO mt sat. (1000°C, 150MPa)					
	85			**86**			**109**			**121**			**124**			**100**			**127**		
	wt %	*1σ*	*n*	**wt %**	*1σ*	*n*	**wt %**	*1σ*	*n*	**wt %**	*1σ*	*n*	**wt %**	*1σ*	*n*	**wt %**	*1σ*	*n*	**wt %**	*1σ*	n
SiO_2	**56.9**	*0.3*	*12*	**57.6**	*0.3*	*10*	**58.0**	*0.5*	*16*	**58.8**	*0.4*	*11*	**58**	*2*	*6*	**54.5**	*0.5*	*14*	**59.0**	*0.4*	*11*
TiO_2	**0.56**	*0.02*	*4*	**0.55**	*0.03*	*4*	**0.55**	*0.02*	*6*	**0.57**	*0.05*	*15*	**0.4**	*0.2*	*9*	**0.49**	*0.02*	*5*	**0.36**	*0.05*	*10*
Al_2O_3	**16.3**	*0.2*	*12*	**16.6**	*0.2*	*10*	**17.5**	*0.4*	*16*	**16.2**	*0.5*	*11*	**16.9**	*0.5*	*6*	**15.9**	*0.3*	*14*	**16.7**	*0.2*	*11*
FeO	**5.9**	*0.2*	*12*	**5.1**	*0.2*	*10*	**5.3**	*0.1*	*16*	**5.2**	*0.3*	*11*	**8**	*1.2*	*6*	**9.7**	*0.9*	*14*	**7.1**	*0.3*	*11*
MnO	**0.098**	*0.002*	*4*	**0.10**	*0.01*	*4*	**0.113**	*0.005*	*6*	**0.109**	*0.009*	*15*	**0.08**	*0.02*	*9*	**0.116**	*0.005*	*5*	**0.134**	*0.007*	*10*
MgO	**2.79**	*0.06*	*12*	**2.87**	*0.06*	*10*	**2.8**	*0.1*	*16*	**2.36**	*0.07*	*11*	**1.8**	*1.0*	*6*	**2.72**	*0.09*	*14*	**3.0**	*0.1*	*11*
CaO	**7.2**	*0.1*	*12*	**7.06**	*0.06*	*10*	**6.9**	*0.3*	*16*	**6.2**	*0.3*	*11*	**6.5**	*0.7*	*6*	**6.6**	*0.2*	*14*	**5.4**	*0.2*	*11*
Na_2O	**2.88**	*0.07*	*12*	**3.01**	*0.05*	*10*	**3.1**	*0.1*	*16*	**3.5**	*0.1*	*11*	**3.5**	*0.2*	*6*	**3.2**	*0.1*	*14*	**3.15**	*0.09*	*11*
K_2O	**0.94**	*0.09*	*12*	**0.77**	*0.04*	*10*	**0.86**	*0.03*	*16*	**0.94**	*0.04*	*11*	**1.0**	*0.1*	*6*	**0.81**	*0.02*	*14*	**0.77**	*0.03*	*11*
S (ppm)	**340**	*80*	*7*	**330**	*60*	*10*	**210**	*40*	*7*	**220**	*20*	*9*	**160**	*40*	*4*	**370**	*30*	*10*	**1800**	*200*	*10*
Cl (ppm)	**1520**	*50*	*7*	**1390**	*60*	*10*	**1370**	*90*	*7*	**1800**	*100*	*9*	**1100**	*80*	*4*	**1550**	*40*	*10*	**1830**	*60*	*10*
Total	**93.8**			**93.8**			**95.2**			**94.0**			**96.2**			**94.2**			**95.9**		
H_2O	**6.2**			**6.2**			**4.8**			**6.0**			**3.8**			**5.8**			**4.1**		
	ppm	*1σ*	*n*	**ppm**	*1σ*	*n*	**ppm**	*1σ*	*n*	**ppm**	*1σ*	*n*	**ppm**	*1σ*	*n*	**ppm**	*1σ*	*n*	**ppm**	*1σ*	*n*
V	**-**	-	-	**-**	-	-	**-**	-	-	**130**	*10*	*15*	**60**	*40*	*9*	**-**	-	-	**40**	*10*	*10*
Co	**-**	-	-	**-**	-	-	**30**	*10*	*6*	**140**	*30*	*12*	**40**	*20*	*7*	**2.3**	*0.2*	*3*	**2.3**	*0.2*	*10*
Cu	**28**	*7*	*4*	**46**	*5*	*4*	**10**	*10*	*4*	**53**	*8*	*15*	**36**	*9*	*9*	**120**	*10*	*5*	**150**	*10*	*10*
Zn	**-**	-	-	**-**	-	-	**19**	3	5	**29**	5	15	**12**	2	7	**41**	8	5	**21**	2	10
Mo	**4**	*2*	*4*	**17**	*4*	*4*	**9**	*1*	*6*	**15**	*4*	*15*	**19**	*5*	*9*	**50**	*6*	*5*	**52**	*5*	*10*
Ag	**-**	-	-	**-**	-	-	**-**	-	-	**0.15**	*0.03*	*4*	**<0.4**	-	-	**-**	-	-	**0.35**	*0.04*	*10*
Cs	**-**	-	-	**35**	*2*	*4*	**48**	*4*	*6*	**23**	*2*	*15*	**38**	*7*	*9*	**38**	*4*	*5*	**30**	*3*	*10*
Au	**0.9**	*0.2*	*2*	**0.8**	*0.2*	*2*	**0.5**	*0.1*	*6*	**0.61**	*0.07*	*9*	**<=0.6**	-	-	**1.4**	*0.1*	*5*	**0.5**	*0.1*	*7*

Top: EPMA analyses, except for TiO_2 and MnO (LA–ICP–MS). H_2O content calculated by difference. Bottom: LA–ICP–MS analyses.

	NNO (1000°C, 150MPa)																							
	92			**94**			**102**			**103**			**108**			**114**			**120**			**125**		
	wt %	*1σ*	*n*	**wt %**	*1σ*	*n*	**wt %**	*1σ*	*n*	**wt %**	*1σ*	*n*	**wt %**	*1σ*	*n*	**wt %**	*1σ*	*n*	**wt %**	*1σ*	*n*	**wt %**	*1σ*	*n*
SiO_2	**57.1**	*0.3*	*10*	**55.9**	*0.4*	*10*	**56.7**	*0.7*	*14*	**58.1**	*0.4*	*13*	**56.2**	*0.3*	*15*	**57.5**	*0.6*	*12*	**58.6**	*0.3*	*9*	**55.2**	*0.3*	*11*
TiO_2	**0.53**	*0.03*	*6*	**0.53**	*0.03*	*5*	**0.53**	*0.05*	*7*	**0.51**	*0.01*	*9*	**0.51**	*0.01*	*6*	**0.52**	*0.04*	*22*	**0.60**	*0.07*	*16*	**0.49**	*0.03*	*16*
Al_2O_3	**16.4**	*0.2*	*10*	**16.1**	*0.3*	*10*	**16.1**	*0.6*	*14*	**16.3**	*0.3*	*13*	**17.0**	*0.2*	*15*	**16.0**	*0.1*	*12*	**16.0**	*0.8*	*9*	**16.0**	*0.1*	*11*
FeO	**5.9**	*0.2*	*10*	**7.4**	*0.2*	*10*	**7.0**	*0.7*	*14*	**5.1**	*0.2*	*13*	**7.5**	*0.3*	*15*	**6.5**	*0.5*	*12*	**6.4**	*0.5*	*9*	**8.4**	*0.2*	*11*
MnO	**0.103**	*0.006*	*6*	**0.111**	*0.004*	*5*	**0.103**	*0.009*	*7*	**0.102**	*0.003*	*9*	**0.114**	*0.004*	*6*	**0.10**	*0.01*	*22*	**0.11**	*0.03*	*16*	**0.114**	*0.007*	*16*
MgO	**2.59**	*0.09*	*10*	**2.5**	*0.1*	*10*	**2.53**	*0.07*	*14*	**2.77**	*0.07*	*13*	**2.90**	*0.05*	*15*	**2.62**	*0.06*	*12*	**2.1**	*0.6*	*9*	**2.79**	*0.06*	*11*
CaO	**7.17**	*0.08*	*10*	**7.0**	*0.1*	*10*	**6.5**	*0.3*	*14*	**6.8**	*0.1*	*13*	**6.86**	*0.08*	*15*	**6.3**	*0.1*	*12*	**6.4**	*0.4*	*9*	**6.65**	*0.06*	*11*
Na_2O	**2.96**	*0.08*	*10*	**2.9**	*0.2*	*10*	**3.3**	*0.1*	*14*	**3.31**	*0.07*	*13*	**3.1**	*0.1*	*15*	**3.37**	*0.09*	*12*	**3.4**	*0.1*	*9*	**3.19**	*0.07*	*11*
K_2O	**0.89**	*0.08*	*10*	**0.78**	*0.07*	*10*	**0.86**	*0.04*	*14*	**0.88**	*0.02*	*13*	**0.81**	*0.02*	*15*	**0.90**	*0.04*	*12*	**0.96**	*0.05*	*9*	**0.80**	*0.02*	*11*
S (ppm)	**360**	*20*	*10*	**790**	*90*	*6*	**330**	*30*	*11*	**200**	*40*	*12*	**400**	*10*	*7*	**750**	*90*	*10*	**180**	*10*	*8*	**590**	*60*	*10*
Cl (ppm)	**1620**	*50*	*10*	**1720**	*80*	*6*	**1450**	*80*	*11*	**1410**	*50*	*12*	**1360**	*60*	*7*	**1800**	*100*	*10*	**1670**	*90*	*8*	**1680**	*40*	*10*
Total	93.8			93.4			93.7			94.0			95.1			94.0			94.8			93.9		
H_2O	6.2			6.6			6.3			6.0			4.9			6.0			5.2			6.1		
	ppm	*1σ*	*n*	**ppm**	*1σ*	*n*	**ppm**	*1σ*	*n*	**ppm**	*1σ*	*n*	**ppm**	*1σ*	*n*	**ppm**	*1σ*	*n*	**ppm**	*1σ*	*n*	**ppm**	*1σ*	*n*
V	**-**	-	-	**-**	-	-	**-**	-	-	**-**	-	-	**-**	-	-	**140**	*20*	*22*	**140**	*30*	*16*	**133**	*8*	*16*
Co	**-**	-	-	**-**	-	-	**3**	-	*1*	**0.9**	*0.2*	*2*	**1.1**	*0.2*	*3*	**8**	*4*	*21*	**2**	*2*	*16*	**1.6**	*0.5*	*16*
Cu	**32**	*5*	*6*	**20**	*10*	*5*	**30**	*20*	*7*	**29**	*7*	*7*	**20**	*10*	*6*	**24**	*7*	*22*	**46**	*7*	*16*	**60**	*10*	*16*
Zn	**-**	-	-	**-**	-	-	**29**	4	7	**35**	3	7	**35**	7	6	**50**	10	22	**30**	6	16	**23**	2	16
Mo	**58**	*7*	*6*	**70**	*20*	*5*	**31**	*7*	*7*	**20**	*6*	*9*	**29**	*7*	*6*	**20**	*10*	*22*	**30**	*10*	*16*	**46**	*3*	*16*
Ag	**-**	-	-	**-**	-	-	**0.19**	*0.06*	*3*	**0.19**	*0.03*	*4*	**0.09**	*0.02*	*2*	**0.13**	*0.04*	*5*	**-**	-	-	**0.16**	*0.03*	*12*
Cs	**22**	*2*	*6*	**23**	*4*	*5*	**47**	*3*	*7*	**44**	*2*	*9*	**46**	*3*	*6*	**34**	*5*	*22*	**36**	*5*	*16*	**28**	*1*	*16*
Au	**1.5**	*0.2*	*6*	**2.4**	*0.2*	*4*	**0.9**	*0.3*	*7*	**0.7**	*0.1*	*7*	**1.5**	*0.1*	*6*	**1.4**	*0.5*	*22*	**0.6**	*0.1*	*7*	**2.3**	*0.3*	*16*

Top: EPMA analyses, except for TiO_2 and MnO (LA–ICP–MS). H_2O content calculated by difference. Bottom: LA–ICP–MS analyses.

3.5.5 Solubility of Au in the silicate melt

Gold solubility in Au-saturated silicate melts has long been sought by modelers of ore-forming systems as a limit on the ability of silicate melts to transport gold. Gold solubility in the current study ranged from 0.5 ± 0.1 ppm to 2.4 ± 0.2 ppm. Gold solubility for reduced samples averaged 0.7 ± 0.2 ppm (log fO_2=CCO, log fS_2 = -1.8 ±0.5, samples 85, 86, 109, 121) and in moderately oxidized samples averaged 1.3 ± 0.6 ppm (log fO_2=NNO, log fS_2 = -0.3±0.2, samples 92, 94, 100, 102, 103, 108, 120). A recent review of the available data on gold solubility in Bell et al. (2011, and references therein) highlights the influence of fO_2 on gold solubility in the melt and emphasizes the need to quantify that influence. The solubility of gold in Au-saturated S-free systems was proposed by Borisov and Palme (1996) to follow: $Au + \frac{1}{4}O_2^{Env.} = AuO_{0.5}^{silicate-melt}$; which implies a direct correlation between fO_2 and gold solubility. In addition to oxygen, sulfur may also complex gold at reduced fO_2 in hydrous melts (e.g., Bell et al. 2009, Jugo et al. 1999 and 2005, and Simon et al. 2006).

Comparisons of Au solubility between melts of different compositions, formed under different conditions of temperature and pressure, are difficult to make. However, available data on the solubility of gold in silicate melts of intermediate composition has recently expanded. Botcharnikov et al. (2010) report Au-solubility of 0.45±0.20 ppm to 2.47±0.42 ppm in H_2O- and S-bearing melts of andesitic composition at 1050°C, 200 MPa, and log fO_2 = NNO. Zajacz et al. (2011) report Au-solubility 0.73 ± 0.17 ppm in an H_2O- and S-bearing melt of andesitic composition at 1000°C, 200 MPa, and at log fO_2 0.4 log units below NNO. Jégo et al. (2010) report Au-solubility of 1.209 ± 0.228 ppm to 4.253 ± 0.356 ppm in H_2O and S-bearing, and sulfide-saturated, melts of andesitic composition at 1000°C, 400 MPa, and log fO_2 at one log unit

below the NNO fO_2 buffer. In each study, the authors report increased gold solubility in S-bearing versus S-free andesitic silicate melts, supporting a dependence on fS_2 as well as fO_2.

Complexing of gold by chlorine in a S-free silicate melt is discussed in Botcharnikov et al. (2010). The apparent activity of chlorine, which varied linearly with concentration in their calculations, correlated with gold concentration suggesting that Cl-complexing is important to gold solubility. But in these experiments, there is no trend of increasing gold solubility with chlorine concentration in the melt. Zajacz et al. (2011) report a weak correlation between gold and chlorine concentration.

With regard to sulfur, however, these data show a direct correlation between sulfur and gold concentrations. Individual experiments from the CCO-buffer (average 280 ± 70 ppm S) and NNO-buffer (average 400 ±200 ppm S) experiments are plotted in Figure 3-10, and show a strong relationship between concentrations in the silicate melt of S and Au. Also plotted are the results of experiments from Botcharnikov et al. (2010) and Jégo et al. (2010) which show positive correlations between Au and S concentration in their reduced S-bearing melts. Data from Jégo et al. (2010), in particular, fit well with a regression of the data from the current study. Together, these studies provide additional supporting evidence of the chalcophile behavior of Au in hydrous glasses with fO_2 at and below NNO. These results are consistent with, at least within the P, T, X conditions of these experiments that sulfur in the melt is a limiting factor on the gold transport ability of silicate melts.

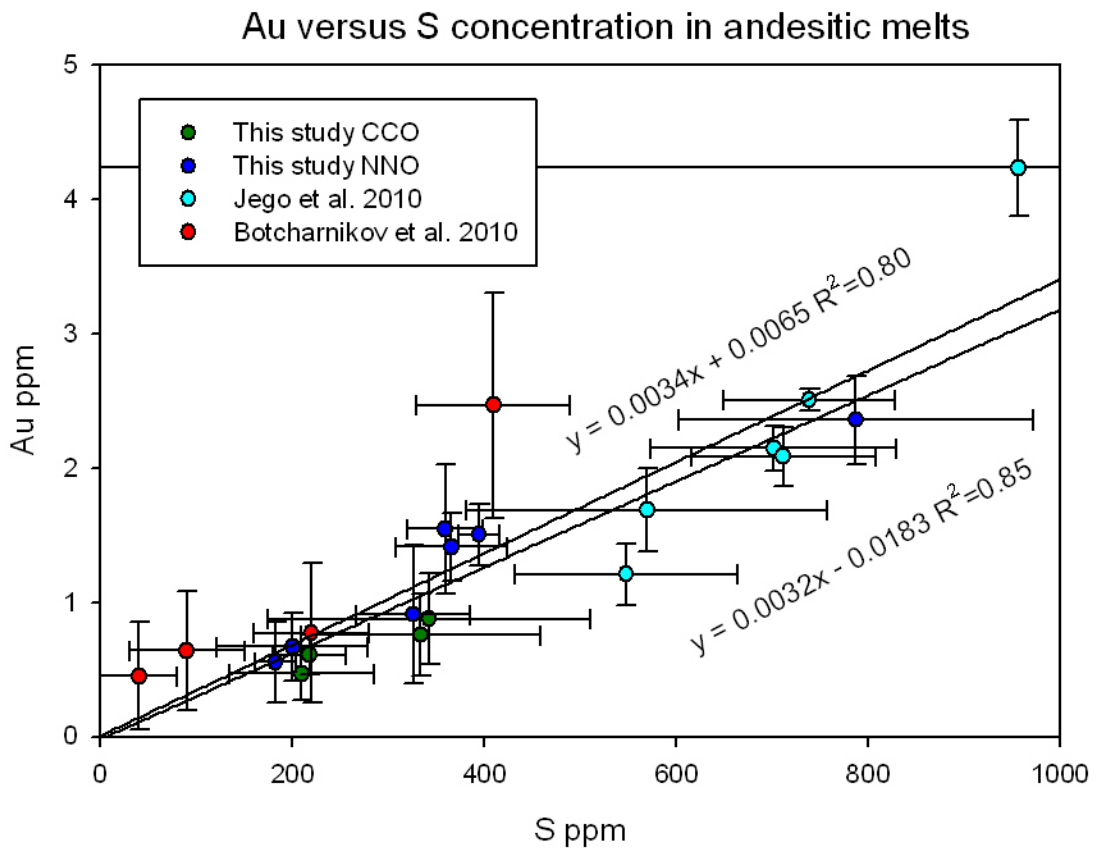

Figure 3-10 Concentrations of Au and S in the silicate melt.
Au concentrations determined by LA–ICP–MS. S concentrations determined by EMPA. Uncertainties are 2σ. Regression line for data from these experiments (bottom) and all data (top) show correlation between Au and S concentration in hydrous andesitic silicate melts from 1000°C to 1050°C, 150 MPa to 400 MPa, and NNO to NNO - 1.6. This correlation supports S-complexing of Au at relatively low oxygen fugacities.

3.5.6 Run product sulfides

The compositions of run product sulfides are listed in Table 3-10. Pyrrhotite and CFSL were recovered from all samples with the exception of run #114. In that experiment, the starting bulk sulfide composition was lower in copper than other experiments, and produced a pyrrhotite with only ~ 2 wt % Cu. In run products from experiments where the sulfides had been pre-reacted in silica tubes, pyrrhotite grains were smaller and the CFSL was present as thin bands among the pyrrhotite. In many of the experiments, sulfides were also found on the surface of

volatile-phase inclusions in the glass. Those sulfides were much smaller, and were present as well-formed 6-pointed stars, which would be consistent with rapid growth of hexagonal pyrrhotite from the volatile phase during quench. Other quench-related sulfide growth was identified by discoloration of the inner surface of the capsule where the capsule was in contact with the volatile phase, but not where the capsule was in contact with the silicate melt. The sulfides that were formed solely on quench could not be analyzed.

The CFSL in all samples contained oxygen. Although concentrations of oxygen in CFSL in this study should be considered semi-quantitative, they are broadly systematic. The concentration of oxygen is inversely related to concentration of sulfur and averages 2.3 ± 0.9 wt %. The concentration of oxygen is less than that found in Fe–S–O melts (Naldrett 1969, Mengason 2007, Simon et al. 2008, Mengason et al. 2011), 8–10 wt %, but similar to CFSL reported by Mungall (2005), 1.3–1.6 wt %.

Table 3-10 Compositions of pyrrhotite and CFSL run products from hydrothermal experiments

	Au capsule CCO (1000°C, 150 MPa)												Au capsule CCO (900°C, 150 MPa)			Au capsule NNO mt sat. (1000°C, 150 MPa)					
	85			**86**			**109**			**121**			**124**			**100**			**127**		
	wt %	*1σ*	*n*	**wt %**	*1σ*	*n*	**wt %**	*1σ*	*n*	**wt %**	*1σ*	*n*	**wt %**	*1σ*	*n*	**wt %**	*1σ*	*n*	**wt %**	*1σ*	*n*
Cu	**5**	*1*	*9*	**4.3**	*0.2*	*9*	**3.9**	*0.1*	*9*	**4.71**	*0.07*	*9*	**5.4**	*0.3*	*9*	**4.0**	*0.3*	*9*	**3.4**	*0.1*	*9*
Fe	**58**	*1*	*9*	**58.4**	*0.5*	*9*	**58.7**	*0.2*	*9*	**57.7**	*0.4*	*9*	**58.4**	*0.2*	*9*	**57.6**	*0.2*	*9*	**56.6**	*0.3*	*9*
S	**36.6**	*0.2*	*9*	**37.1**	*0.2*	*9*	**37.52**	*0.09*	*9*	**37.1**	*0.2*	*9*	**36.4**	*0.2*	*9*	**38.1**	*0.1*	*9*	**39.2**	*0.1*	*9*
total	**99.7**			**99.8**			**100.1**			**99.6**			**100.3**			**99.6**			**99.2**		
	ppm	*1σ*	*n*	**ppm**	*1σ*	*n*	**ppm**	*1σ*	*n*	**ppm**	*1σ*	*n*	**Ppm**	*1σ*	*n*	**ppm**	*1σ*	*n*	**ppm**	*1σ*	*n*
Ti	**-**	-	-	**6**	*1*	*3*	**-**	-	-	**35**	*7*	*10*	**40**	*10*	*10*	**40**	*10*	*16*	**38**	*7*	*16*
V	**-**	-	-	**-**	-	-	**-**	-	-	**15**	*2*	*10*	**2**	*1*	*8*	**3**	*1*	*12*	**1**	*0*	*4*
Mn	**310**	*50*	*3*	**420**	*20*	*3*	**340**	*30*	*5*	**500**	*100*	*10*	**250**	*50*	*10*	**260**	*50*	*20*	**240**	*40*	*16*
Co	**90**	*20*	*3*	**35**	*2*	*3*	**46**	*4*	*5*	**8000**	*1000*	*10*	**800**	*200*	*10*	**60**	*10*	*20*	**160**	*50*	*16*
Ni	**-**	-	-	**-**	-	-	**-**	-	-	**130**	*20*	*8*	**-**	-	-	**60**	*10*	*6*	**7000**	*2000*	*16*
Zn	**-**	-	-	**24**	*2*	*3*	**20**	*4*	*5*	**31**	*8*	*10*	**11**	*3*	*8*	**40**	*30*	*19*	**30**	*60*	*16*
Mo	**8**	*4*	*3*	**160**	*60*	*3*	**140**	*20*	*5*	**160**	*20*	*10*	**140**	*40*	*10*	**20**	*9*	*20*	**14**	*4*	*16*
Ag	**3**	*1*	*3*	**38**	*2*	*3*	**7.9**	*0.5*	*5*	**9**	*3*	*10*	**6**	*3*	*10*	**10**	*5*	*20*	**6**	*2*	*16*
Au	**67**	*65*	*4*	**260**	*30*	*3*	**180**	*10*	*5*	**290**	*50*	*10*	**13**	*2*	*10*	**400**	*200*	*18*	**1300**	*400*	*16*

Cu, Fe and S = EPMA analyses, all others by LA–ICP–MS.

Au capsule NNO (1000°C, 150 MPa)

	92			94			102			103			108			114			120			125		
	wt %	*1σ*	*n*	**wt %**	*1σ*	*n*	**wt %**	*1σ*	*n*	**wt %**	*1σ*	*n*	**wt %**	*1σ*	*n*	**wt %**	*1σ*	*n*	**wt %**	*1σ*	*n*	**wt %**	*1σ*	*n*
Cu	**3**	*1*	*11*	**2.8**	*0.6*	*11*	**5.09**	*0.08*	*11*	**4.52**	*0.04*	*11*	**3.75**	*0.04*	*9*	**1.56**	*0.05*	*9*	**5.35**	*0.04*	*6*	**3.7**	*0.1*	*9*
Fe	**58**	*1*	*11*	**58.2**	*0.6*	*11*	**58.0**	*0.1*	*11*	**57.9**	*0.1*	*11*	**58.0**	*0.4*	*9*	**59.6**	*0.3*	*9*	**57.0**	*0.2*	*6*	**57.5**	*0.2*	*9*
S	**38.0**	*0.6*	*11*	**38.2**	*0.4*	*11*	**38.2**	*0.3*	*11*	**38.3**	*0.2*	*11*	**38.28**	*0.05*	*9*	**39.3**	*0.1*	*9*	**38.07**	*0.09*	*6*	**38.5**	*0.1*	*9*
total	**99.0**			**99.2**			**101.3**			**100.7**			**100.0**			**100.5**			**100.5**			**99.7**		
	ppm	*1σ*	*n*	**ppm**	*1σ*	*n*	**ppm**	*1σ*	*n*	**ppm**	*1σ*	*n*	**ppm**	*1σ*	*n*	**ppm**	*1σ*	*n*	**ppm**	*1σ*	*n*	**ppm**	*1σ*	*n*
Ti	**10**	*1*	*4*	**11.6**	*0.3*	*3*	**40**	*20*	*14*	**32**	*7*	*16*	**-**	-	-	**34**	*5*	*12*	**30**	*10*	*14*	**30**	*10*	*16*
V	**-**	-	-	**-**	-	-	**8**	*2*	*14*	**10**	*2*	*16*	**-**	-	-	**1.9**	*0.5*	*11*	**3**	*1*	*14*	**2**	*1*	*16*
Mn	**390**	*80*	*4*	**340**	*30*	*3*	**500**	*100*	*14*	**500**	*100*	*16*	**300**	*40*	*5*	**340**	*50*	*12*	**290**	*80*	*14*	**310**	*70*	*16*
Co	**44**	*5*	*4*	**52**	*7*	*3*	**22**	*5*	*14*	**39**	*6*	*16*	**28**	*3*	*5*	**31**	*5*	*12*	**80**	*20*	*14*	**80**	*20*	*16*
Ni	**-**	-	-	**-**	-	-	**120**	*40*	*14*	**130**	*20*	*14*	**-**	-	-	**80**	*9*	*8*	**120**	*40*	*8*	**1200**	*200*	*16*
Zn	**11**	*4*	*4*	**21**	*5*	*3*	**50**	*30*	*14*	**60**	*10*	*16*	**30**	*5*	*5*	**43**	*7*	*12*	**26**	*8*	*14*	**30**	*10*	*16*
Mo	**84**	*5*	*4*	**40**	*10*	*3*	**50**	*20*	*14*	**46**	*7*	*16*	**100**	*20*	*5*	**40**	*20*	*12*	**90**	*30*	*14*	**19**	*8*	*16*
Ag	**3.2**	*0.8*	*4*	**4.0**	*0.6*	*3*	**27**	*9*	*14*	**22**	*6*	*16*	**8**	*2*	*5*	**6**	*1*	*12*	**21**	*6*	*14*	**7**	*2*	*16*
Au	**13**	*3*	*4*	**17**	*8*	*4*	**240**	*30*	*14*	**700**	*100*	*16*	**480**	*90*	*5*	**900**	*100*	*12*	**400**	*100*	*14*	**800**	*200*	*16*

Cu, Fe and S = EPMA analyses, all others by LA–ICP–MS.

Table 3-11 Analyses of CFSL run products from hydrothermal experiments

	CCO (1000°C, 150 MPa)												CCO mt. sat. (900°C, 150MPa)			NNO mt sat. (1000°C, 150 MPa)					
	85			**86**			**109**			**121**			**124**			**100**			**127**		
	wt %	*1σ*	*n*	**wt %**	*1σ*	*n*	**wt %**	*1σ*	*n*	**wt %**	*1σ*	*n*	**wt %**	*1σ*	*n*	**wt %**	*1σ*	*n*	**wt %**	*1σ*	*n*
Au	**2***	4	17	**4***	1	9	**6**	2	5	**5***	1	14	**0.4***	0.1	13	**4***	2	9	**15.6**	5.6	9
Cu	**20**	3	17	**21**	2	9	**23**	2	5	**28**	1	8	**31**	3	14	**16**	2	11	**33.8**	3.0	9
Fe	**43**	4	17	**41**	2	9	**37**	1	5	**34**	1	8	**37**	2	14	**47**	2	11	**22.2**	1.1	9
S	**31**	1	17	**31.7**	0.7	9	**29.4**	0.8	5	**30.1**	0.6	8	**29.2**	0.4	14	**31.0**	0.9	11	**29.5**	1.2	9
O	**3**	1	17	**2.4**	0.4	9	**2.9**	0.5	5	**2.1**	0.2	8	**2.4**	0.3	14	**4.5**	0.7	11	**0.6**	0.2	9
total	**97.8**			**96.1**			**97.9**			**94.2**			**99.4**			**98.9**			**101.7**		
	ppm	*1σ*	*n*	**ppm**	*1σ*	*n*	**ppm**	*1σ*	*n*	**ppm**	*1σ*	*n*	**Ppm**	*1σ*	*n*	**ppm**	*1σ*	*n*	**ppm**	*1σ*	*n*
Ti	**-**	-	-	**40**	7	3	**60**	20	3	**40**	5	13	**60**	50	13	**210**	80	9	**60**	40	11
V	**-**	-	-	**-**	-	-	**16**	4	3	**27**	3	14	**2**	3	5	**30**	10	9	**<= 5**	-	-
Mn	**1000**	500	3	**670**	50	3	**880**	50	3	**860**	80	14	**400**	100	13	**600**	200	9	**300**	200	11
Co	**120**	50	3	**21**	2	3	**31**	6	3	**3000**	1000	14	**500**	200	13	**29**	9	9	**70**	20	11
Ni	**-**	-	-	**-**	-	-	**-**	-	-	**400**	1000	11	**200**	200	3	**<150**	-	-	**14000**	4000	11
Zn	**-**	-	-	**90**	10	3	**140**	20	3	**200**	100	14	**65**	9	13	**300**	100	9	**100**	200	11
Mo	**9**	2	3	**27**	5	3	**3**	1	3	**8**	6	14	**9**	3	13	**12**	6	9	**2**	2	10
Ag	**18**	8	3	**2200**	200	3	**700**	300	3	**800**	100	14	**500**	80	13	**600**	200	9	**600**	300	11

Au (without *), Cu, Fe, S, and O = EPMA analyses, all others by LA–ICP–MS.

	NNO (1000°C, 150 MPa)																				
	92			**94**			**102**			**103**			**108**			**120**			**125**		
	wt %	*1σ*	*n*	**wt %**	*1σ*	*n*	**wt %**	*1σ*	*n*	**wt %**	*1σ*	*n*	**wt %**	*1σ*	*n*	**wt %**	*1σ*	*n*	**wt %**	*1σ*	*n*
Au	**9**	4	4	**4***	4	7	**4**	2	11	**8**	4	8	**5**	3	9	**10**	2	8	**13**	3	6
Cu	**21.8**	0.5	4	**22.7**	0.8	3	**24.7**	0.8	11	**21**	2	8	**21**	7	9	**25.5**	0.9	8	**22.6**	0.7	6
Fe	**37**	2	8	**40**	1	3	**38**	1	11	**38**	3	8	**39**	8	9	**34.2**	0.9	8	**35**	2	6
S	**32.2**	0.8	8	**33.8**	0.4	3	**30.7**	0.9	11	**31.6**	0.8	8	**31**	2	9	**29.7**	0.8	8	**29.3**	0.6	6
O	**1.6**	0.3	4	**1.5**	na	na	**2.5**	0.2	11	**1.8**	0.5	8	**2.2**	0.7	9	**2.4**	0.2	8	**2.1**	0.4	6
total	**102.1**			**98.2**			**100.1**			**101.0**			**97.9**			**101.8**			**101.9**		
	ppm	*1σ*	*n*	**ppm**	*1σ*	*n*	**ppm**	*1σ*	*n*	**ppm**	*1σ*	*n*	**ppm**	*1σ*	*n*	**ppm**	*1σ*	*n*	**ppm**	*1σ*	*n*
Ti	**30**	20	15	**60**	30	7	**60**	30	13	**80**	30	10	**70**	20	14	**50**	20	16	**60**	40	14
V	**20**	20	8	**10**	10	4	**21**	7	13	**23**	8	10	**40**	20	14	**22**	4	16	**8**	2	14
Mn	**500**	300	15	**300**	100	7	**700**	200	13	**1000**	200	10	**1000**	200	14	**700**	70	16	**500**	90	14
Co	**20**	10	15	**20**	10	7	**13**	4	6	**19**	8	5	**30**	10	14	**28**	7	16	**52**	6	13
Ni	**120**	70	6	**200**	200	7	**<150**	-	-	**-**	-	-	**300**	100	14	**100**	10	3	**4100**	600	14
Zn	**110**	60	15	**200**	70	7	**300**	100	12	**300**	200	10	**210**	50	14	**150**	30	16	**80**	20	14
Mo	**7**	6	14	**10**	10	7	**9**	3	13	**13**	5	10	**13**	4	14	**7**	3	16	**2**	1	9
Ag	**50**	70	15	**100**	100	7	**2000**	600	13	**1100**	300	10	**500**	100	14	**2100**	400	16	**400**	70	14

Au (without *), Cu, Fe, S, and O = EPMA analyses, all others by LA–ICP–MS.

3.5.7 Solubility of Au in sulfide phase

Concentrations of Au in sulfide run products from Cu–Au alloy saturated experiments, both silica tube and hydrothermal, are positively correlated with sulfur fugacity (Figures 3-11 and 3-12). To understand this, consider a hypothetical statement of equilibrium between Au in the alloy (*metal*) and pyrrhotite (*po*):

$$\mu Au^{metal} + \tfrac{1}{4}\mu S_2^{gas} = \mu AuS_{0.5}^{po}$$

In terms of an equilibrium constant (K), the equation becomes:

$$K = \frac{a_{AuS_{0.5}}^{po}}{a_{Au}^{metal} \cdot \left(f_{S_2}^{gas}\right)^{1/4}}, \text{ or } X_{AuS_{0.5}}^{po} = \frac{K \cdot a_{Au}^{metal}}{\gamma_{AuS_{0.5}}^{po}} \cdot \left(f_{S_2}^{gas}\right)^{1/4}.$$

If this is an accurate description of the system, then the relationship between $\left(f_{S_2}^{gas}\right)^{1/4}$ and $X_{AuS_{0.5}}^{po}$ should be linear with a slope equal to $\frac{K \cdot a_{Au}^{metal}}{\gamma_{AuS_{0.5}}^{po}}$ (Figure 3-11).

The slope of the line plotted in Figure 3-11 was calculated using:

$$\frac{K}{\gamma_{AuS_{0.5}}^{po}} = K'(apparent) = \frac{X_{AuS_{0.5}}^{po}}{\left(f_{S_2}^{gas}\right)^{1/4} \cdot a_{Au}^{metal}}$$

The slope is 0.00028. For this calculation, the components $AuS_{0.5}$, $CuS_{0.5}$, FeS, and S were used. For the silicate tube experiments, samples of the alloy in each experiment were recovered and analyzed and the activity of Au and Cu were calculated with the FactSage 'SGnobl' database (http://www.factsage.com/) which uses the Cu–Au activity model from Sunderman et al. (1998) (table 3-11). For hydrothermal experiments, the activity of Au was approximated to be 1.

Table 3-11 Mole fractions and activities of Au and Cu in recovered metal alloy

	X_{Au}^{metal}	1σ	X_{Cu}^{metal}	1σ	n	a_{Au}^{metal}	a_{Cu}^{metal}
116a	0.9876	*0.0003*	0.0124	*0.0003*	*7*	0.9881	0.0049
116b	0.980	*0.003*	0.020	*0.003*	*6*	0.981	0.008
118a	0.9584	*0.0007*	0.0416	*0.0007*	*6*	0.9629	0.0141
118b	0.945	*0.001*	0.055	*0.001*	*6*	0.952	0.018
117a	0.969	*0.001*	0.031	*0.001*	*6*	0.972	0.011
117b	0.957	*0.001*	0.043	*0.001*	*6*	0.962	0.014

Activities of Cu and Au calculated using the Fact Sage SGnobl database (http://www.factsage.com/). Cu–Au activity model from Sunderman et al. (1998).

The fit of the line suggests that the data follow a power law relationship suggested by the statement of equilibrium ($x^{0.25}$), and further suggests that the activity coefficient (γ) does not vary significantly over the range of concentrations considered here.

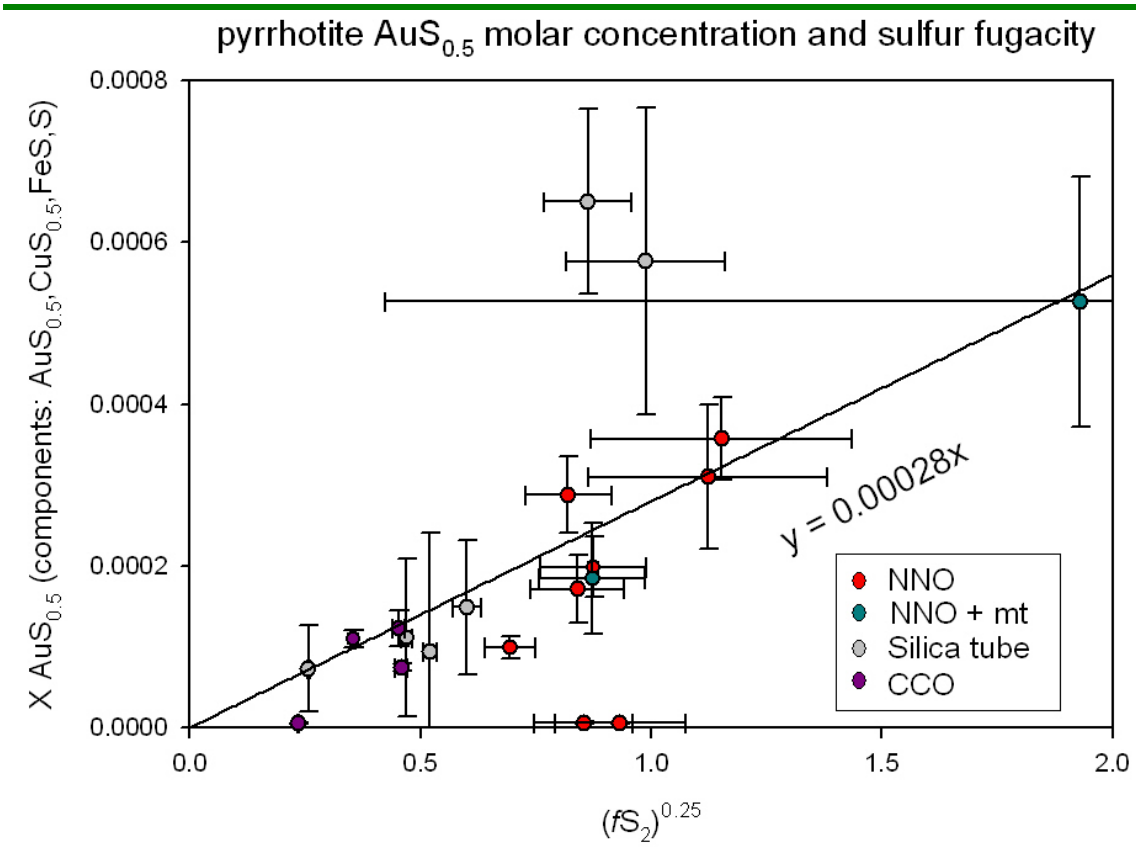

Figure 3-11 Au concentration in pyrrhotite as a function of $fS_2^{0.25}$.
Power law relationship ($x^{0.25}$) plots as a straight line. The majority of the data fall on a line with a slope equal to the average K' (see text for explanation). Two silica tube experiments (116a and 116b), and two hydrothermal experiments (92 and 94) were not included in the average. Uncertainties are 1 sigma for mole fraction and fS_2. Uncertainties for fS_2 are calculated in log units, and approximated here by symmetrical uncertainty bars.

This relationship gives a way to calculate the expected equilibrium concentration of Au in hydrothermal experiments performed in Au or Cu–Au alloy capsules from sulfur fugacity. A similar treatment can be applied to CFSL (Figure 3-12).

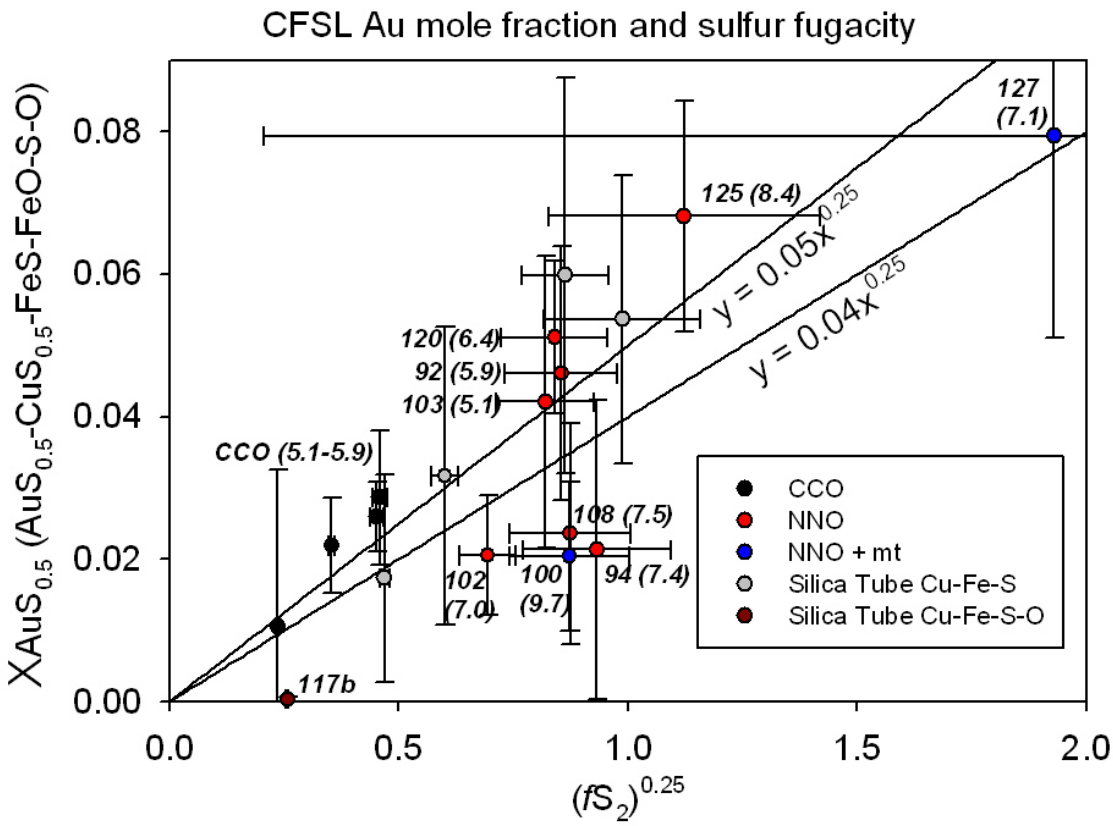

Figure 3-12 Au concentration in CFSL as a function of $fS_2^{0.25}$.
Power law relationship ($x^{0.25}$) plots as a straight line. The majority of the data fall on a line, with a slope equal to the average K' (see text for explanation). Uncertainties are 1 sigma mole fraction and fS_2. Uncertainties for fS_2 are calculated in log units, and approximated here by symmetrical uncertainty bars.

Interestingly, the concentrations of Au in the CFSL in the alloy-undersaturated silica tube experiments can also be correlated to sulfur fugacity. However, proportions of the phases present are not the same in all run products. Mass balance calculations for copper in the run product compared to starting materials were used to calculate pyrrhotite/CFSL ratios in the run products. Pyrrhotite/CFSL in the run products decreased with fS_2. In the Cu–Fe–S system, sulfur fugacity is broadly related to the sulfur fraction of the bulk sulfide composition. Considering the relevant portion of the Cu–Fe–S phase diagram, a shift in bulk

composition within the two-phase field toward the sulfur axis would predict a higher proportion of pyrrhotite. With less mass of CFSL acting as a reservoir for Ag and Au, and given constant partition coefficients over this range of concentrations, the concentrations of these elements in both pyrrhotite and CFSL will be greater.

3.5.8 Concentration of copper in a silicate melt saturated with pyrrhotite and CFSL

The concentration of copper in the andesitic silicate melt, among NNO and CCO experiments, averages 32 ± 13 ppm (± 4 ppm when calculated as the standard deviation of the mean). Based on analysis of Cu–Au alloys from the silica tube experiments, the activity of this concentration of copper is the apparent solubility with an activity of copper ~0.01. Ripley et al. (2002) report that copper solubility shows dependence on both oxygen and sulfur in their experiments with CFSL-saturated silicate melts of basaltic composition. Within the range of fS_2 and fO_2 of the two main groups of experiments in this study, a trend is not apparent beyond the limits of uncertainty. However, some trends are suggested when considering the data from experiments at other conditions of fS_2 and fO_2. Run 125 exhausted its fugacity buffer and had fO_2 > NNO, and fS_2 higher than other experiments performed with fO_2 = NNO. Run 125 had 60 ± 10 ppm Cu, higher than the range of experiments characterized by experiments performed at fO_2 = CCO (35 ± 18) and at fO_2 = NNO (29 ± 10 ppm). Run 100 was performed at fO_2 = NNO, but was magnetite saturated. Run 100 had 120 ± 10 ppm Cu. Run 127 exceeded its NNO oxygen fugacity buffer assemblage, had the highest fS_2, and was magnetite-saturated; the concentration of copper in the silicate melt was 150 ± 10 ppm. Higher fO_2 and fS_2 do appear to

increase the concentration of copper in andesitic melts saturated with pyrrhotite + CFSL, but not over the range fO_2 =CCO to fO_2 =NNO. Magnetite saturation appears to significantly raise the concentration of copper in the silicate melt under these conditions. Run 124 was run at 900°C with a CCO oxygen fugacity buffer, and was expected to have lower concentrations of copper in the silicate melt than other experiments with CCO buffers runs at 1000°C. However, at 36 ± 9 ppm Cu, it is close to the average for similar 1000°C runs. Although this run exceeded its buffer, it is likely that the relatively high concentration of copper is due to magnetite saturation and higher concentration of FeO in the silicate melt. Overall, in magnetite-undersaturated andesitic magmas at oxygen fugacities between fO_2 =CCO to fO_2 =NNO, there is no systematic change in the concentration of minimum Cu required for the silicate melt to saturate with CFSL vs. pyrrhotite.

3.5.9 Partition coefficients

Partition coefficients have been calculated for Cu, Mo, Ag, and Au among pyrrhotite, CFSL, and the silicate melt. Experiments are frequently performed to determine sulfide/sulfide partition coefficients at atmospheric pressure and H_2O-free which are then applied to hydrous magmas at crustal pressures. In Figure 3-13, results from silica tube experiments are compared to the results of the hydrothermal experiments, and those results support the application of partition coefficients (sulfide/sulfide) determined at atmospheric pressure to the higher P and T conditions within the crust.

Nernst-type partition coefficients ($D_i^{CFSL/pyrrhotite}$) for Cu, Mo, Ag, and Au between CFSL and pyrrhotite, are plotted against fS_2 in Figure 3-13. Copper is a major constituent of both phases, and cannot appropriately be called a partition coefficient, but is included here for the purpose of comparison. The fO_2 experiments were performed at is indicated by the data symbol. Mo, Ag and Au are bonded to sulfur in CFSL and pyrrhotite, therefore no trend is expected with sulfur fugacity, and none is seen here. This is important to establish, since it affects the applicability of the partition coefficients across systems at different fS_2. Unlike sulfide/silicate-melt partition coefficients, which are subject to the effects of sulfur and oxygen fugacity (Jugo et al. 1999, Mengason 2007), these sulfide/sulfide partition coefficients are more broadly applicable. Data from Mengason (2007) are plotted to illustrate the greater magnitude of the partition coefficients in this study. The sulfide liquids in Mengason (2007) had little copper, and significantly more oxygen (8–10 wt % oxygen) than sulfide liquids studied here (2.3 ± 0.9 wt % oxygen).

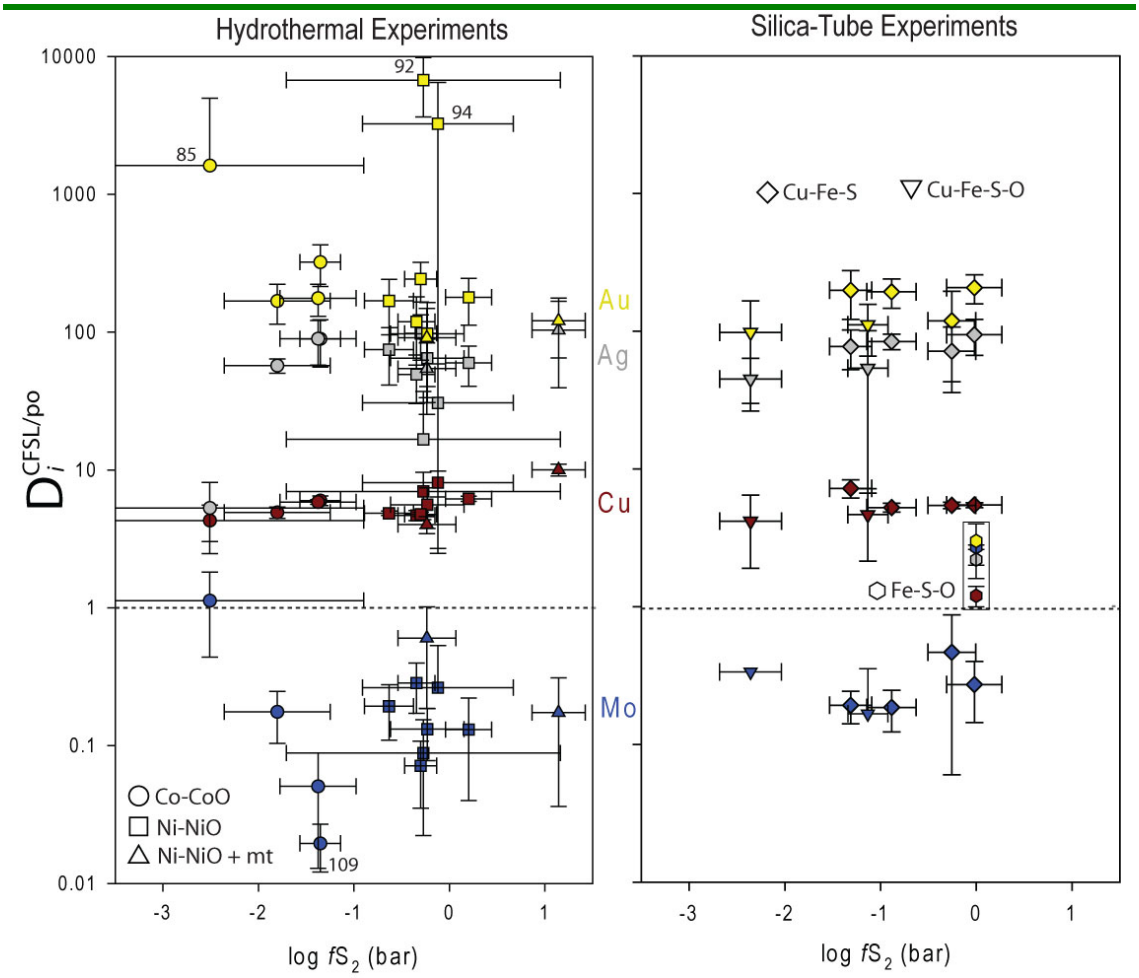

Figure 3-13 $D_i^{CFSL/pyrrhotite}$ **for Cu, Mo, Ag, and Au as a function of** fS_2**.**
Data in box from Mengason 2007 using Fe–S–O melts and pyrrhotite. Au and Ag show similar partitioning behavior and lack of trend with fS_2. Mo partitions more strongly into pyrrhotite. These data suggest that the behavior of Cu–Fe–S–O–liq. run products may be intermediate between the Cu–Fe–S–liq. run products of the silica tube experiments and Mengason 2007.

These data support one hypothesis of this research—that Au and Ag will strongly partition into a more Cu-rich iron-sulfide (CFSL in this case) realitve to pyrrhotite, as suggested by Jugo et al. (1999), who studied intermediate solid solution ($CuFeS_2$) and pyrrhotite. However, Mo partitions more strongly into pyrrhotite in contrast to Au and Ag, and in contrast to the behavior of Mo in Mengason (2007) and Mengason et al. (2011 – in press). This is contrary to the hypothesis that Mo would

favor the reduced long-range order of the sulfide liquid. The incorporation of ~3–5 wt % Cu in pyrrhotite may alter its crystal structure and allow sites that better fit the smaller (0.65) versus >0, more highly charged Mo ion. Alternately, Mo^{4+} and one or more Cu^{1+}, may be part of a coupled substitution for Fe^{3+} and/or Fe^{2+}. Of course, arguments based on ionic radii in sulfides, which possess significant covalent, and metallic bonding, may not fully explain the complexity of the relationships. Partition coefficients for other elements analyzed for in run products of the hydrothermal experiments are plotted in Figure 3-14. Partition coefficients (CFSL/po) increase from Co (<1) to Mn, Ti, V, and Zn.

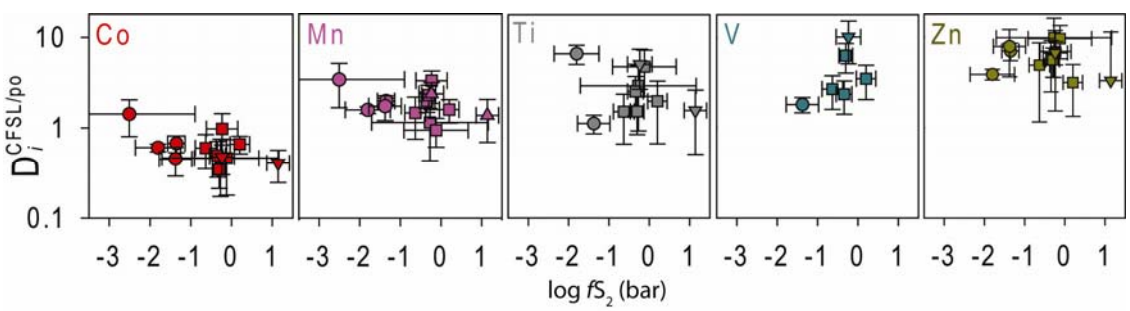

Figure 3-14 $D_i^{CFSL/pyrrhotite}$ **for Co, Mn, Ti, V, and Zn as a function of** fS_2**.**
Mn, Ti, V, and Zn favor CFSL with respect to pyrrhotite, as do Cu, Ag, and Au in the preceding figure. Only Co, like Mo in the preceding figure, favors pyrrhotite to CFSL.

3.5.10 Summary of partitioning coefficients

Overall partition coefficients ($D_i^{pyrrhotite/melt}$, $D_i^{CFSL/melt}$, and $D_i^{CFSL/pyrrhotite}$) for the experiments performed at CCO and NNO are presented in Table 3-12. An additional significant figure is included in the tables to prevent unnecessary rounding errors. I have chosen to present an overall partition coefficient including both groups

as they have significant overlap. Excluded from this average are: run 85 (lower calculated fS_2 than other experiments performed at fO_2 = CCO), runs 125 and 127 (higher fO_2 than NNO), and run 124 (performed at 900°C). Run 114 (no CFSL, pyrrhotite only) is included for $D_i^{pyrrhotite\ /\ melt}$ except for Cu. Ratios of copper among the phases are included as partition coefficients but are not appropriately termed partition coefficients, as they are essential constituents of the sulfide phases. For gold partition coefficients only, runs 92 and 94 are omitted due to heterogeneity evident in backscatter electron images. Partition coefficients among elements studied between pyrrhotite or CFSL have already been noted. With regard to the melt, Au partitions the most strongly into the sulfide phases among the elements here, followed by Ag (and Cu). Only Ti, V, and Mn partition preferentially into the silicate melt. Mo shows opposing behaviors for two sulfide phases.

Table 3-12 Overall partition coefficients from this study

	$D_i^{po\ /\ melt}$	$1\sigma_{\bar{X}}$	n	$D_i^{CFSL\ /\ melt}$	$1\sigma_{\bar{X}}$	n	$D_i^{CFSL\ /\ po}$	$1\sigma_{\bar{X}}$	n
Ti	0.0085	*0.0015*	*9*	0.0228	*0.0073*	*8*	3.27	*0.71*	*8*
V	0.05	-	*3*	0.2	-	*2*	4.7	*1.6*	*5*
Mn	0.463	*0.034*	*11*	0.856	*0.085*	*10*	1.91	*0.22*	*10*
Co	26.8	*7.1*	*7*	15.9	*3.7*	*6*	0.553	*0.056*	*10*
Cu	1320	*220*	*11*	7800	*1400*	*10*	5.57	*0.39*	*10*
Zn	1.14	*0.14*	*8*	7.43	*0.65*	*7*	6.85	*0.61*	*10*
Mo	1.73	*0.37*	*8*	0.45	*0.14*	*10*	0.188	*0.054*	*10*
Ag	90	*19*	*5*	6800	*1300*	*4*	62.4	*8.3*	*10*
Au	500	*87*	*9*	84000	*19000*	*8*	181	*26*	*8*

Uncertainty calculated as standard deviation of the mean. n = number of samples. Average not presented for sample size < 4 (indicated by -). An additional significant figure has been included to avoid introducing unwanted rounding errors in calculations; I do not imply a greater degree of precision. See text for details of experiments included in the averages.

Partition coefficients are calculated for trace elements between phases with the assumption that the behavior of the elements in each phase is consistent with

Henry's Law. The behavior of an element may deviate from Henry's Law when present at elevated concentrations. This deviation may lead to underestimation or overestimation of partition coefficients. In Figure 3-13, partition coefficients for gold between CFSL and pyrrhotite calculated from Cu–Au alloy saturated hydrothermal experiments (D = 180 ± 80, 1 sigma) agree with those calculated from alloy under-saturated experiments (D = 160 ± 50) performed using silica tubes. This is despite the deference in mean concentrations from the hydrothermal experiments for pyrrhotite (pyrrhotite = 400 ± 300 ppm, 1 sigma) and CFSL (6 ± 2 wt %), versus the mean concentrations from the silica tube experiments for pyrrhotite (20 ± 20 ppm) and CFSL (0.4 ± 0.4 wt %). This suggests that gold is not present in these examples at concentrations sufficient to exhibit non-Henrian behavior. In general, caution should be exercised in the application of any partition coefficients to geologic problems where concentrations differ from the conditions under which the partition coefficients were determined.

Some partition coefficients from this study can be compared to partition coefficients determined from experimental studies at other conditions. Most studies related to pyrrhotite involve more felsic melts than used here. $D_{Cu}^{pyrrhotite/melt}$ from this study (1320±220) falls between the value of 500±200 reported by Lynton et al. (1993) (fO_2 = 1/2 log unit above NNO buffer, 800°C, 100 MPa, rhyolitic melt) and 2600±300 reported by Jugo et al. (1999) (NNO, 850°C, 100 MPa, synthetic haplogranite melt). $D_{Au}^{pyrrhotite/melt}$ from this study (500±87) is somewhat greater than the 140±40 reported by Jugo et al. (1999) and the 120±50 reported by Simon et al. (2008) (~NNO, 1040°C, ~1 bar, rhyolitic melt). Most studies related to sulfide liquids

involve more mafic melts than used here, as well as more Ni-rich sulfide liquids. A useful starting point is to note the similarity between $D_{Au}^{CFSL/pyrrhotite}$ from this study (181±26) and the value of 100 reported by Mungall (2005) at similar conditions using a Ni–Cu–Fe sulfide liquid (~0.7 log units below NNO, 1000°C, ~1 bar). However, $D_{Au}^{CFSL/melt}$ from this study (84000±19000) is considerably higher than the value of 1000±900 reported by Stone et al. (1990) using a Ni–Fe sulfide liquid and basaltic melt (fO_2 ~ wustite–magnetite buffer, ~ 1 bar, 1200ºC), and higher than the range of values 1210±950 to 13600±10100 reported by Crocket et al. (1997) also using a Ni–Fe sulfide liquid and basaltic melt at high temperature (1250ºC). Ultimately, there is little data in this range of composition and temperature with which to compare. In the next section, modeling is performed using the partition coefficients determined in this study.

3.6 Discussion

3.6.1 Origins of andesitic magmas and sulfide–silicate interactions

Several models have been proposed to explain the generation of igneous rock types in volcanic arcs, which may bear on the production of any given magma. Sulfides present in the source region will affect the abundance of ore metals in the melts produced. Again, any ore metal that is removed from the magma by partitioning into magmatic sulfides (or other non-buoyant phases), may be unavailable for later magmatic–hydrothermal ore formation toward the termination of magmatic activity in the Earth's epizone.

Potential sources of magma in arc settings include the subducting slab, mantle wedge, and the lithosphere of the overriding plate. Melting of the subducted slab may be limited to very young lithosphere (Defant and Drummand 1990) and will therefore only rarely be a factor in magmas related to later, shallow-level, hydrothermal ore formation. Partial melting of the mantle wedge due to the depression of its solidus by the presence of water, and possibly by corner-flow related decompression, results in the formation of basalt and possible primary andesite, which are buoyantly transferred to the crust (e.g., Tatsumi and Eggins 1995, Schmidt and Poli 1998, Grove et al. 2002). Island arc construction is dominated by this process, with differentiation by fractional crystallization leading to the formation of intermediate and felsic intrusive and extrusive rocks (Hasse et al. 2006). Continental arc construction is complicated by the possibility of magma pooling at and within the lower-crust (Herzberg et al. 1983), resulting in the partial melting of previously emplaced igneous rock or metamorphic basement (Annen et al. 2006). The likely origins of intermediate rock in continental arcs encompass primary mantle melts undergoing crystallization, remelted (or remobilized) mantle derived-basalts with varied degrees of crystallization, and partial-melting of metamorphic basement, with associated assimilation–crystallization. Simplified scenarios of sulfide–melt interactions during partial melting and fractional crystallization and their implications for potential magma-sourced ore-genesis are considered in the following sections.

3.6.2 Sulfide separation and ore metal ratios in arc magmas: partial melting

The effect of sulfides present in the source region of mantle-derived basaltic magmas on the potential for porphyry Cu and Au deposit formation has been

examined by several authors (e.g., Campbell and Naldrett 1979, Peach et al. 1990, Mungall 2002). Melting within the mantle may occur at temperatures as high as 1350°C (Schmidt and Poli 1998, Tatsumi 2003). Only sulfide liquids may be stable in the system Cu–Fe–S–O at temperatures in excess of 1200°C. In contrast, partial melting within the lower crust that produces andesitic (or more felsic) magmas will occur at temperatures below 1200ºC. Pyrrhotite as well as sulfide liquids may be stable lower temperatures. A schematic cross-section of continental arc crust in Figure 3-15 shows the potential relationship between source region and temperature in magmatic systems that ultimately produce porphyry and related ore deposits. An andesitic silicate melt, such as that formed in this study, may be produced at a range of temperatures depending on the composition of the source rock, pressure, and the availability of water and other volatiles.

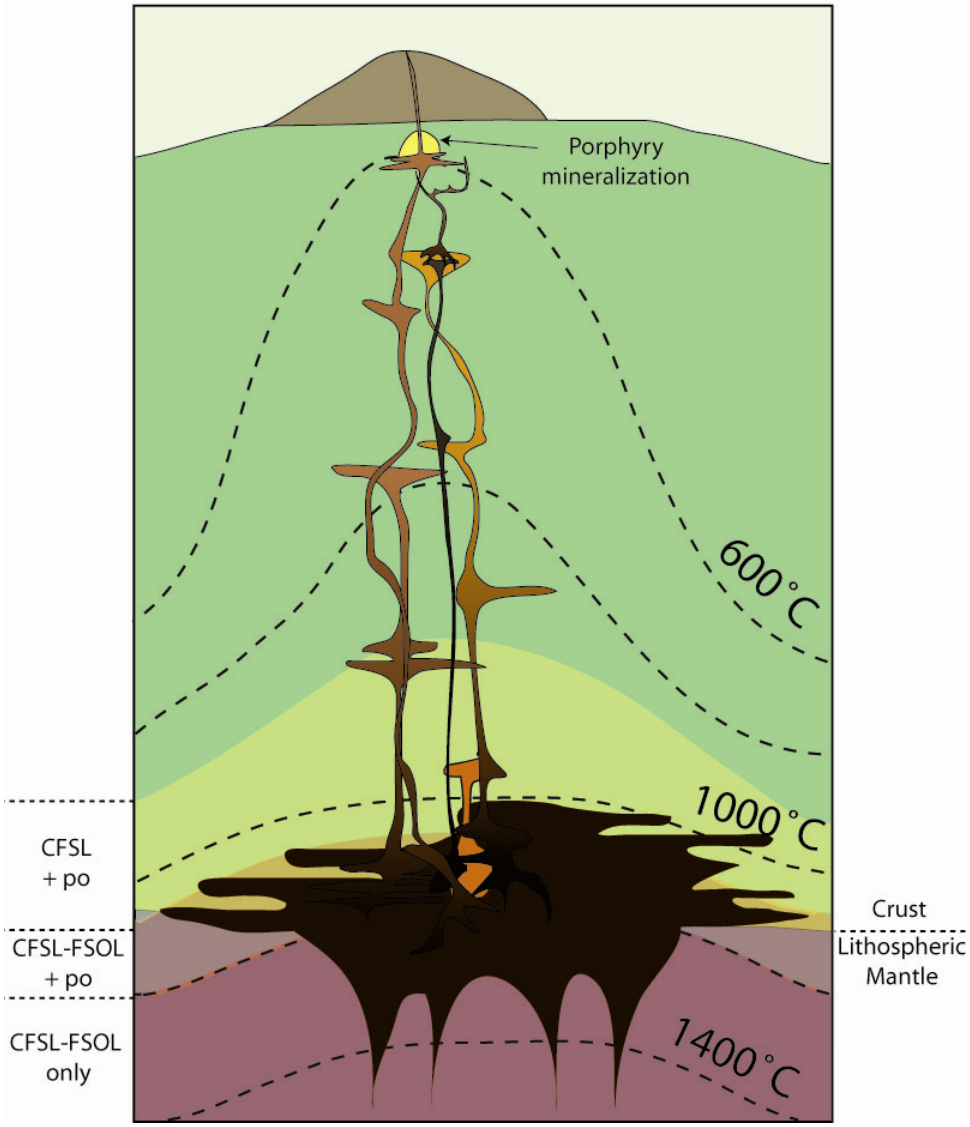

Figure 3-15 Schematic diagram of a section of arc crust
Melting in the mantle wedge (not shown) results in basaltic melts that can be emplaced in the lower crust. Repeated intrusions generate melting in the lower crust in an area of MASH (Hildreth and Moorbath 1998) or "hot zone" (Annen et al. 2006). Thermal gradients within that zone (modeled after Richards 2011) will dictate the stability of sulfide phase assemblages stable during partial melting. At temperatures > ~1200°C a sulfide liquid alone will be stable (CFSL to FSOL in composition)—red field. Between ~1200°C and ~1050°C (depending on fS_2 and fO_2) pyrrhotite and a sulfide liquid (CFSL–FSOL) can be stable—orange field. From ~1050°C down to poorly constrained temperature, pyrrhotite and CFSL may be stable—yellow field. Silicate melts produced during partial melting within the mantle wedge and partial melting at the base of the crust will be in equilibrium with sulfide liquids. Melts formed at lower temperatures, i.e. higher within the crust and/or of a more felsic compositions, may be in equilibrium with pyrrhotite and a sulfide liquid, depending on the availability of Cu. Cu is, effectively, an essential constituent of the sulfide liquid in experiments in this study at 1000°C—below 1050°C sulfide liquids will not form in Cu-poor systems. Metals left behind in sulfide phases will be unavailable during later mineralization events. Fractional crystallization will take place throughout the thickness of the crust, and sulfide stability will be based on the temperature of the melt at the point of crystallization.

Based on the melting experiments of Müntener et al. (2001) and Sisson et al. (2005), Annen et al. (2006) define the compositions and melt fractions produced by melting of gabbro in the lower crust as a function of water content and temperature. In their model, at pressures appropriate to the lower crust, (1.2 GPa for the experiments of Müntener et al. 2001 and 0.7 GPa for the experiments of Sisson et al. 2005), an andesitic melt with 3.8 to 5 wt % H_2O may be produced by partial melting of gabbro at 1000°C. Cu–Fe sulfides that may be present during this melting include CFSL, CFSL and pyrrhotite, or pyrrhotite only (bornite solid-solution is also possible at higher concentrations of Cu in low fS_2 systems). This sulfide assemblage would also be applicable to the generation of dacitic melt at lower temperature. Partial melting at temperatures of 1050°C and above, where the sulfide assemblage may include a sulfide liquid with composition ranging from CFSL to FSOL and pyrrhotite, would result in the production of andesitic melt with low H_2O content, basaltic-andesitic melts, or basaltic melts. At any temperature, sulfides that equilibrate with the silicate melt and then remain with other residual phases in the source region may sequester metals reducing the likelihood of porphyry deposit formation.

A simple mass–balance model has been used here to evaluate the effect of Cu-rich sulfide phases on the potential loss of metals during the generation of an andesitic melt of 3.8 to 5 wt % H_2O at 1000°C, by ~ 40 wt % partial melting of gabbro. Cu, Mo, Ag, and Au were distributed among the silicate melt and sulfide phases present based on partition coefficients calculated from the run products of this study, the masses of the phases, and total concentrations of the metals. Other residual phases are assumed to play little role in the distribution of these elements and are

excluded from calculations. Models of two initial bulk concentrations of copper are described, one with an initial concentration 10 ppm Cu, and one with an initial concentration 40 ppm Cu. These values were chosen to illustrate trends in the loss of copper to the sulfide phases.

In the first case, a low initial bulk concentration for copper of 10 ppm was used. If no sulfide were present during melting, then all of the copper would be concentrated in the silicate melt at 25 ppm. In this model, with no sulfide present, the silicate melt would also contain Mo (10 ppm), Ag (5 ppm), and Au (80 ppb). Concentrations of Mo, Ag, and Au were also chosen to illustrate trends in metal loss to sulfides. From this simplest example with no sulfide, the mass balance calculations were done with successively greater proportions of sulfide. The results are plotted in Figure 3-16 (top left). The concentration of copper in the silicate melt as well as Mo, Ag, and Au are plotted as a function of the proportion of sulfide present among the residual phases. In the figure, as an increasing proportion of sulfides are included in the calculation, Cu and Au are reduced relative to Ag and Mo. Results from the same calculations are also plotted in the top right graph in Figure 3-16. In this graph, the percentage of the total metal that is contained within the silicate melt is plotted as a function of the sulfide proportion in the residual phases. The proportion of the total metal in the silicate melt is a measure of the efficiency, or lack thereof, of the transfer of metals from the source region to the silicate melt. The efficiency of this transfer better expresses the effect of sulfide separation from the silicate melt (in this case by remaining along with other residual phases in the source region) on the likelihood of porphyry deposit formation, or on the relative

concentrations of ore metals within a deposit. At 0.05 % (by weight) sulfide in the cumulate phases (in order of increasing depletion by sulfide separation), ~5% of the Ag, 25% of the Au, and 50% of the Cu have been left in the source region. At 0.10 % sulfide, ~10% of the Ag, 40% of the Au and 65% of the Cu have been left in the source region. The trends of these losses proceed smoothly to higher sulfide proportions.

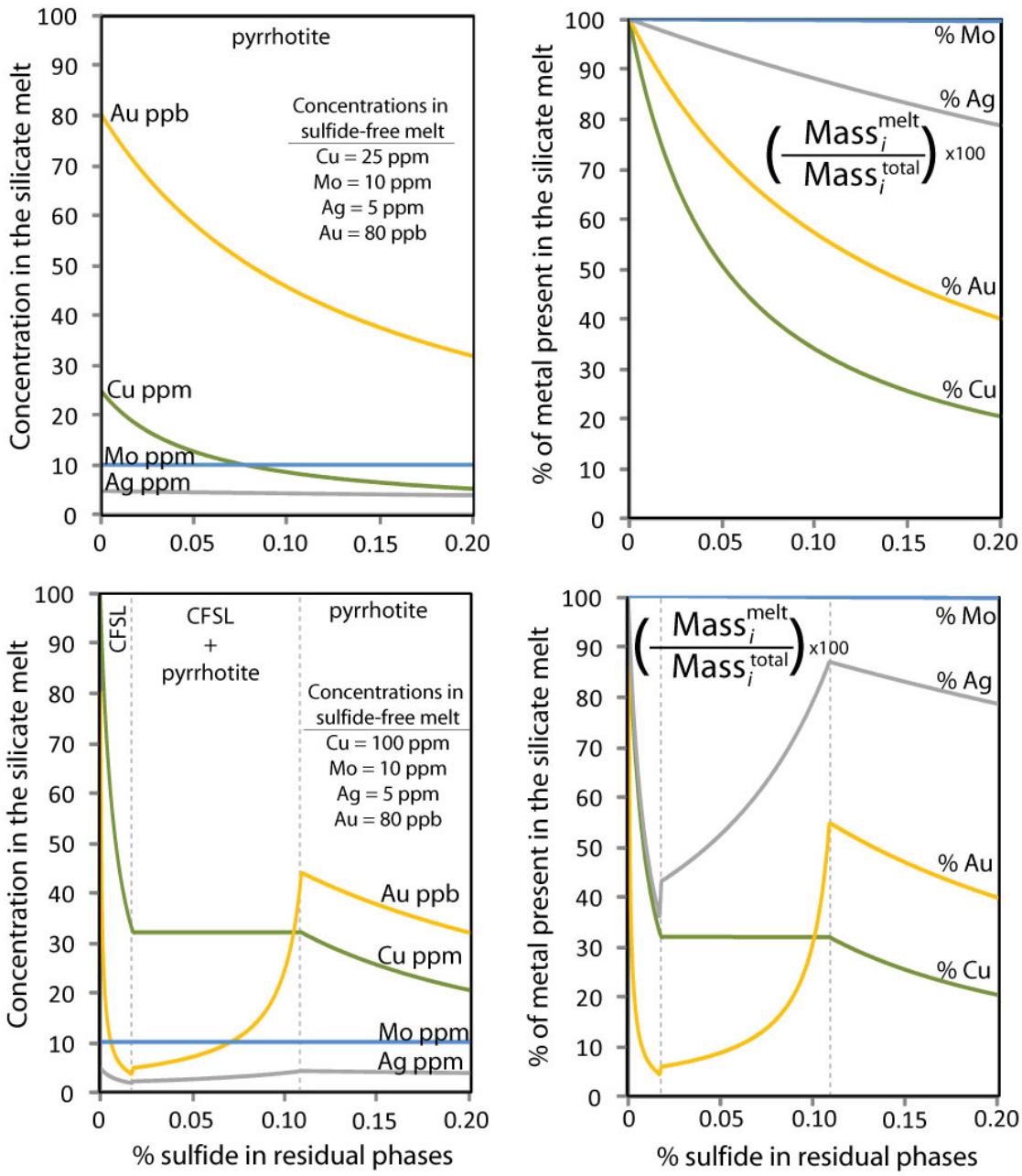

Figure 3-16 Modeling partial melting in the presence of sulfides
See text for details. X-axis is the percent by weight of sulfide among residual phases. Maximum concentrations in the melt occur in a sulfide-free melt. Top Left: Cu and Au partition strongly into pyrrhotite, and are depleted in models run with larger percentages of pyrrhotite, while concentrations of Mo and Ag change little. Top Right: loss of metals to the sulfide phases smoothly increases with increasing sulfide %. Bottom Left: at low sulfide %, CFSL depletes Cu and Au in the melt. Where CFSL and pyrrhotite are stable, Cu concentration is buffered in the melt and Au concentration increases as the ratio of pyrrhotite/CFSL increases. Bottom Right: Note differences in relative losses among metals. In models with < 0.1 % sulfide, Au has been significantly more depleted than Cu compared to Top Right.

In contrast, models with a higher initial bulk concentration of copper result in markedly different sulfide assemblages and different behavior with regard to the relative losses of the ore metals to the sulfide phases. A model with an initial bulk concentration of 40 ppm Cu results in a concentration of 100 ppm Cu in the silicate melt with no sulfides present. In Figure 3-16 (bottom left and right) the results of calculations similar to those above are plotted. An additional step is added to calculations in this case, to determine which sulfides will be stable. At this temperature (1000°C), fS_2, and fO_2, copper is an essential constituent of CFSL and the sulfide liquid must have a minimum concentration of copper to be stable. That minimum concentration in the sulfide liquid has a corresponding concentration in the silicate melt, and in the coexisting pyrrhotite, all of which are known for the conditions of the hydrothermal experiments. The average concentration of copper in the silicate melt in the hydrothermal experiments (32 ± 4 ppm) is used as a cutoff for scenarios involving the presence of CFSL vs. pyrrhotite + CFSL vs. pyrrhotite alone. Mass balance calculations are made for each of these three scenarios. When performing these calculations, if the concentration of copper in the silicate melt saturated with CFSL was greater than 32 ppm, then the 'CFSL only' scenario was used. If the calculated concentration of copper in the silicate melt saturated with pyrrhotite was less than 32 ppm, then the 'pyrrhotite only' scenario was used instead. If calculations based on the CFSL-only scenario did not result in a concentration greater than 32 ppm Cu in the melt and the calculations of the pyrrhotite-only scenario did not result in a concentration less than 32 ppm Cu in the melt, then a value of exactly 32 ppm Cu in the silicate melt is used along with the mass of the

silicate melt, the total mass of the sulfide phases, and the concentrations of copper in all three of the phases at equilibrium to determine the masses of CFSL and pyrrhotite. The three scenarios are labeled in Figure 3-16, bottom left, for models with a maximum concentration of 100 ppm Cu in the silicate melt. Lastly, having calculated the masses of the sulfide phase or phases present, mass balance calculations are performed for Mo, Ag, and Au.

Trends among the concentrations of Cu, Mo, Ag, and Au vary considerably between the three different scenarios in Figure 3-16 (bottom left). In the CFSL-only field, Au and Cu are both sharply reduced relative to Ag and Mo with increasing sulfide composition. The Cu:Au ratio in the silicate melt is also increased. At ~0.02 wt % sulfide in the residual phases, for this particular starting concentration of copper, the copper has been diluted by the total amount of sulfide, and therefore both CFSL and pyrrhotite must be stable. Note that if the initial concentration of copper had been higher the location of the boundary between CFSL-only and CFSL + pyrrhotite would be shifted to the right in the graph to a higher sulfide percentage in the residual phases. In the next field, the concentration of copper in the silicate melt is buffered by the presence of pyrrhotite and CFSL, whereas the concentration of Au in the silicate melt increases along with the ratio of pyrrhotite to CFSL. In the last field, pyrrhotite alone is present, and the trends resemble those of the low initial Cu concentration model. In Figure 3-16 (bottom right) the percentage of the total metal in the silicate melt plotted, to illustrate the efficiency of transfer to the silicate melt. At 0.02 wt % sulfide, ~ 60 wt % of the Ag, 70 wt % of the Cu, and 95 wt % of the Au remains in the residual phases. Again, these are listed in increasing sequestration by

the sulfide phases; note the change in the order of the elements from above. At 0.05 wt % sulfide, ~ 50 wt % of the Ag, 60 wt % of the Cu, and 90 wt % of the Au remains in the residual phases. Despite an increase in the percentage of sulfide in the residual phases, less metal is sequestered because the relatively Cu-poor phase (pyrrhotite) is less effective than CFSL at sequestering Cu, Ag, and Au. At 0.1 % sulfide among the residual phases, ~20% of the Ag, 60% of the Cu, and 70% of the Au are sequestered.

In comparison to these models, one can consider partial melting under other conditions. Melting within the mantle to produce a basaltic melt may take place with only sulfide liquids stable regardless of copper concentration. Trends in the retention of metals by the sulfide liquid would be similar to the CFSL field in the bottom of Figure 3-16. Melting within the crust at temperatures over ~1050°C may have FSOL coexisting with pyrrhotite, again despite low concentrations of copper in each phase as in Mengason 2007 (see also Simon et al. 2008). Trends in the retention of metals by the FSOL and pyrrhotite would be similar to the CFSL + pyrrhotite field in the bottom of Figure 3-16, as opposed to models plotted in the top of Figure 3-16. Also notable is the contrasting behavior of molybdenum in the models presented here, relative to the other elements. In these models, the ratio of Mo to Cu, Ag, or Au will increase with the presence of sulfides in the source region, as Cu, Ag and Au are sequestered.

In general, in the temperature range within which this modeling and these experiments fall, a higher bulk concentration of copper will result in more effective sequestering of Cu, Ag and Au during partial melting. The relative degree of this sequestration among these elements will result in higher Cu:Au and Cu:Ag ratios.

Although the total reduction in metals reduces the likelihood of porphyry deposit formation, if one were created, this would favor a porphyry Cu as opposed to porphyry Cu+(Ag,Au) deposit. The effects on the metal budgets of Cu, Mo, Ag, and Au of sulfide separated from silicate melt during fractional crystallization, are considered in the next section.

3.6.3 Sulfide separation and ore metal ratios in arc magmas: fractional crystallization

Fractional crystallization is a ubiquitous process in magmatic systems, operating on small and large scales. Crystallization can be induced by loss of heat to surrounding rocks as silicate melts move through the crust. Decreasing temperature also lowers the sulfur concentration at sulfide saturation (SCSS) (Jugo et al. 2005, Jugo 2009, Li and Ripley 2005, 2009, Liu et al. 2007, Mavrogenes and O'Neil 1999), resulting in the formation of sulfides. These sulfides may be isolated from the melt, along with silicate and oxide crystal separates. As in the discussion of partial melting, sulfides resulting from fractional crystallization may sequester chalcophile metals, metals that might otherwise be available for later ore formation (Candela and Piccoli 2005, Jugo et al. 1999). Sulfide sequestration will be most effective in the absence of a water-rich volatile phase, which could host a significant portion of the metal budget in its own right. Magma may become volatile-saturated in the lower-middle crust, but the vapor phase would likely be CO_2-rich rather than water rich (Lowenstern 2001, Witter et al. 2004, 2005). Saturation with respect to a water-rich vapor phase is more likely to occur in upper-crustal magma chambers (Lowenstern 2001, Shishkina et al. 2010). Sulfide deposition in the lower to middle crust may

therefore significantly impact the metal budget of magmas. In order to model sulfide formation during a particular crystallization interval, it is necessary to specify the sulfide phases present throughout that interval.

Nearly all of the experiments in this study were designed to constrain the silicate melt to a composition where pyrrhotite and CFSL were both stable. Experiment 114 was designed to have insufficient copper to form CFSL. Pyrrhotite with 1.56 ±0.05 wt % Cu was the only sulfide run product in that experiment. This observation confirms that a high activity of Cu is required to form a sulfide liquid under the conditions of temperature, pressure, fO_2, and fS_2 of these experiments. Formation of CFSL from components of the silicate melt will drive the composition of the silicate melt towards the CFSL/pyrrhotite boundary (Figure 3-17). At this cotectic, CFSL and pyrrhotite would both form on cooling and the concentration of copper in the silicate melt would be buffered until CFSL was no longer stable. However, on consideration of the data from these experiments, it is reasonable to suggest that there is a reaction boundary, not a cotectic-like boundary, between CFSL and pyrrhotite analogous to the enstatite–forsterite reaction boundary in the system enstatite–forsterite–anorthite. Arguments in support of that position are presented below.

Along a cotectic-like boundary, two phases separate out from the melt phase upon cooling. Along a reaction boundary, one phase converts to another upon cooling. Under this assumption (see Figure 3-17), in the case of fractionation, as CFSL is fractionated from the hypothetical magma, its high copper concentration causes the composition of the silicate liquid to move toward the CFSL + pyrrhotite

reaction curve; however, because the CFSL is steadily removed as the magma cools during fractionation, there is no CFSL to convert to pyrrhotite. The liquid composition would then pass through, the CFSL/pyrrhotite boundary, the melt would saturate with respect to pyrrhotite, and the melt composition would move to progressively lower concentrations of copper in both the pyrrhotite and silicate melt with decreasing temperature.

A schematic representation is shown in Figure 3-17 of the system Q (quartz, H_2O, plagioclase, pyroxene), Cu, and $Fe_{1-x}S$ (representing the composition of pyrrhotite at a given fS_2). The upper left inset diagram shows the system Cu–Fe–S–O (as in the inset in Figure 3-3) to show how sulfide and oxide compositions map onto the base of the ternary diagram. Compositions of phases are projected onto a plane that is orientated with respect to the fS_2 and fO_2 of the system. fS_2 is reflected in the composition of pyrrhotite (one apex of the yellow triangular plane), and fO_2 is reflected in the chosen composition between oxygen and iron (in this case at the composition of magnetite). The dimension Q is added to the plane Cu, $Fe_{1-x}S$, $FeO_{1.5}$ in the upper right inset quaternary diagram. The central figure is a projection of that quaternary from $FeO_{1.5}$ down to the ternary Q, Cu, $Fe_{1-x}S$ diagram. Note that the diagram is greatly exaggerated in the Q direction to focus on compositions otherwise close to the base. Approximate compositions of bornite, CFSL, and pyrrhotite are included for 1000°C. Within the diagram, fields in which chalcopyrite, pyrrhotite and CFSL will be stable are shown. The proposed boundary between CFSL and pyrrhotite is shown with a double arrow, indicating it is a reaction, or "odd" (Ricci 1951) boundary. If it were a cotectic boundary, a tangent from the line (in this case

actually a plane in the Q–Cu–$Fe_{1-x}S$–mt quaternary) would intersect the bounding join of the phase diagram between the compositions of pyrrhotite and CFSL, indicating that both would be formed on cooling (Ricci 1951). However, in these experiments, the tangent from the curve projects from the Cu/$Fe_{1-x}S$ ratio in the silicate melt to the composition of pyrrhotite. That is, the tangent appears, within error, to intersect the pyrrhotite field, and pyrrhotite alone can be formed on cooling by the example reaction 0.005Cu + $Fe_{0.9}S$ => $Cu_{0.005}Fe_{0.9}S$, indicating that it is a reaction boundary.

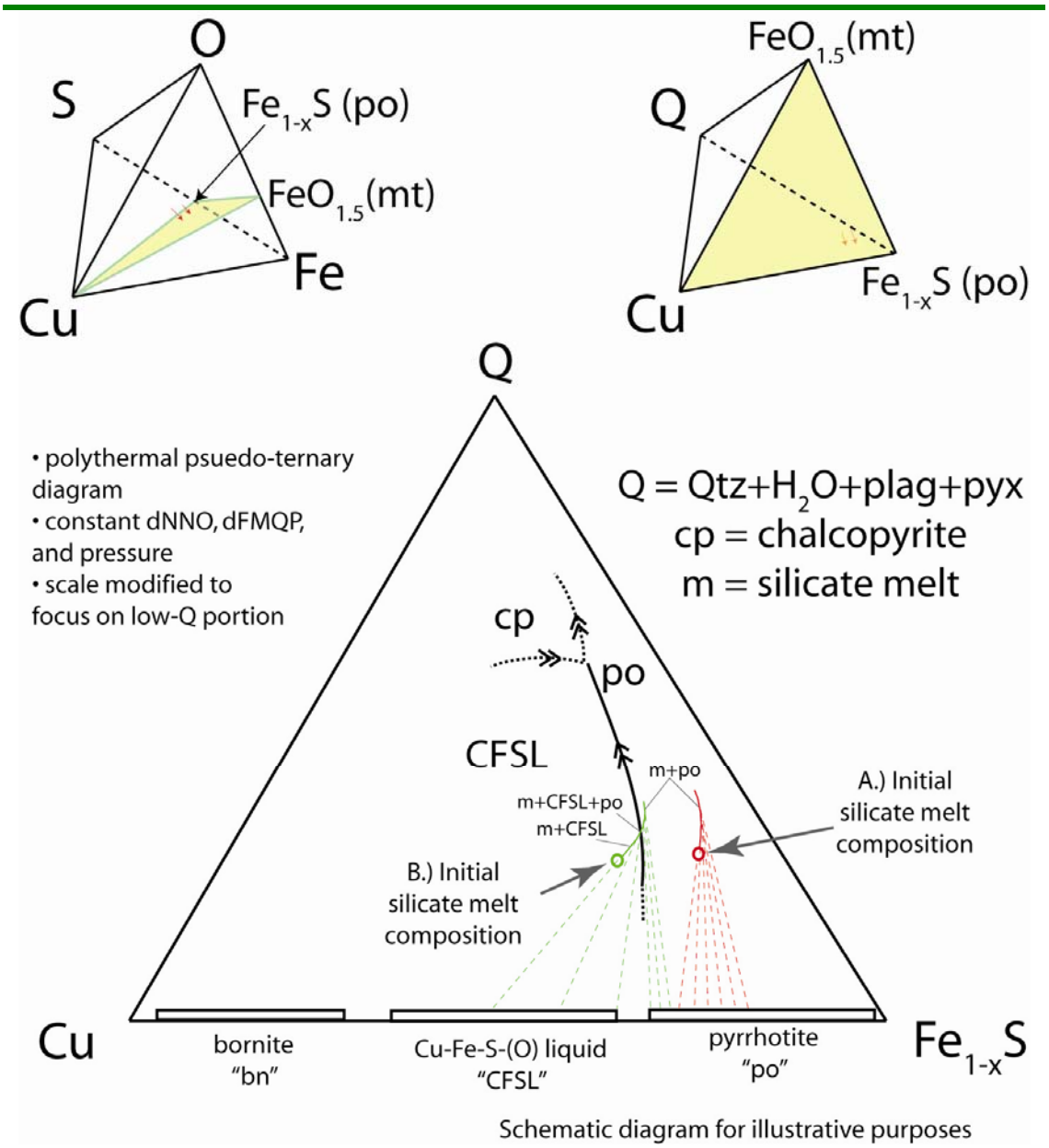

Figure 3-17 Schematic diagram of the system Q–Cu–$Fe_{1-x}S$.
Not to scale. Diagram greatly exaggerated in the Q direction to aid discussion. Composition of the sulfide phases project onto the base, here representative of compositions at ~1000°C, and fS_2 and fO_2 similar to experiments. Inset diagrams provided to orient the reader with respect to other sulfide and oxide compositions. A and B are example starting silicate melt compositions of a magma undergoing fractional crystallization. On cooling, silicate melt A will reach saturation with pyrrhotite, which then drives the composition of the melt away from pyrrhotite. The melt and pyrrhotite produced become less Cu-rich. Silicate melt B, on cooling, will form CFSL driving the composition of the silicate melt towards, and then through, the reaction boundary to form pyrrhotite. The effect of fractional crystallization of A and B on Cu, Mo, Ag, and Au budgets plotted in Figure 3-18.

Two hypothetical cases are shown in Figure 3-17 to illustrate the potential effect on sulfide phase assemblages and the evolution of the silicate melt composition of this reaction boundary. The two cases are also used in the following section to model the effect on ore metal budgets of sulfide separation during fractional crystallization (Figure 3-18). Point A (red circle in Figure 3-17) represents a starting silicate melt composition that forms pyrrhotite on cooling. Compositions of the silicate melt during continued cooling are indicated by the solid red line and compositions of the pyrrhotite are indicated by red dashed tie-lines. Both have decreasing concentrations of copper with decreasing temperature (increasing % crystallization of the melt). Point B (green circle in Figure 3-17) represents a more copper-rich starting silicate melt composition. CFSL is initially produced on cooling until the composition of the silicate melt reaches the reaction boundary, after which pyrrhotite is produced. All three phases have decreasing concentrations of copper with decreasing temperature

The effect of these two hypothetical cases on the metal budgets of Cu, Mo, Ag, and Au have been modeled (Figure 3-18). Modeling was conducted for an interval of 30% Rayleigh fractional crystallization. The hypothetical starting composition would be more mafic and at a higher temperature than conditions of these experiments, such that after 10% crystallization the melt would be at the conditions of these experiments. Partition coefficients determined in this study were used, with the partial exception of $D_{Cu}^{CFSL/melt}$. In Ripley et al. (2002), $D_{Cu}^{CFSL/melt}$ systematically decreased from 1200 to 800 with increasing Cu wt % in the CFSL from 30 to 50 wt %. Partition coefficients in Ripley et al. (2002) were smaller than

those calculated in the current study, likely an effect of the increased polymerization in intermediate silicate melts. A partition coefficient intermediate between the values of Ripley et al. (2002) and those determined here at 0% crystallization. The partition coefficient is increased with increasing crystallization until it reaches the partition coefficient from this study at 10% crystallization.

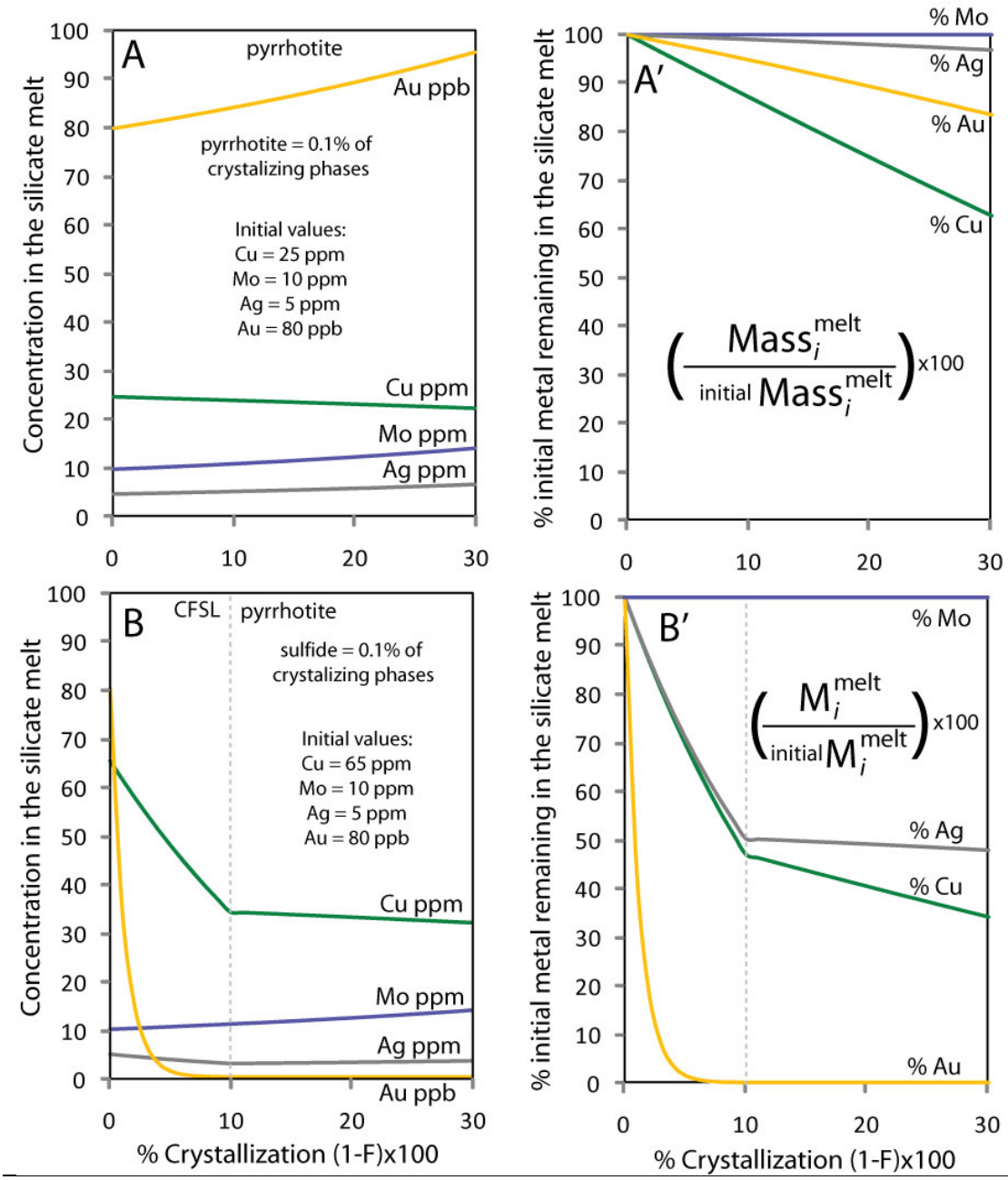

Figure 3-18 Modeling fractional crystallization with loss of sulfides

A.) Concentrations in the silicate melt vs. percent Rayleigh fractional crystallization. Decreasing temperature causes sulfide loss to crystal separates due to decreased sulfide content at sulfide saturation. Sulfide formation based on path A in Figure 3-17. See text for details of partition coefficients used. Initial concentrations were chosen to illustrate trends. Concentrations of ore metals are not strongly affected by this degree of pyrrhotite loss. A'.) Although some concentrations have risen, approximately 5% of the Ag, 15% of the Au, and 40 % of the Cu have been sequestered and will be unavailable for potential porphyry deposit formation. B.) Initial saturation by CFSL (path B in Figure 3-17) causes near-complete loss of Au from the silicate melt, and lowers Cu; values change little with pyrrhotite crystallization. B'.) Approximately 50% Ag, 60% Cu, and greater than 99% Au are sequestered in the sulfide phases.

In Figure 3-18, crystallization of a composition of point A (red path from Figure 3-17) is shown at the top, and B (green path from Figure 3-17) is shown on the bottom. Sulfides make up 0.1 wt % of the fractionating phases. This is comparable to the 0.1 wt % sulfide determined by Luhr et al. (1984) samples from the andesitic El Chichón volcano. In case A, the concentration of copper in the melt decreases while Mo, Ag, and Au increase. However, a potentially more important consideration is the overall loss of metal to the sulfide phases. As a percent of the initial mass, Cu, Ag, and Au all decrease over this interval. The new melt composition produced by this process has lost approximately 3% of its initial abundance of Ag, 15% of its Au, and 35% of its Cu. In B, the initial concentration of copper is higher but the models are otherwise the same. Gold concentration in the silicate melt is almost completely depleted within the first 10% of crystallization. The concentration of copper is reduced by half, whereas molybdenum and silver concentrations rise. In terms of metal lost, approximately 50% Ag, 60% Cu, and on the order of 99.9% Au has been removed. As in the partial melting diagrams, the model can be calculated for alternate sulfide fractions. However the trends in the diagrams for total metal loss should remain the same.

3.7 Conclusions

The effect of sulfides on the potential of magmatic arc systems to yield porphyry or other magmatic–hydrothermal deposits has been a subject of study for several decades. In this study it has been found that an andesitic melt at 1000°C, 150 MPa, with oxygen fugacity between CCO and NNO, and sulfur fugacity between -1.6

and -0.25 log units fS_2, will be saturated with CFSL at 32 ± 4 ppm Cu. In the context of the data presented from the NAVDAT database, the average bulk composition of rocks with a similar range of SiO_2, was 34 ± 29 ppm Cu, with outliers extending up to a weight percent Cu. This, along with the large fraction of Cu-rich sulfides among those detailed by Hattori (1996) from Mt St. Helens suggests that saturation of arc magma by CFSL is a common phenomenon.

In this study, the direct correlation between the concentration of gold in the silicate melt, and the concentration of sulfur is consistent with results reported by researchers, suggesting that at fO_2 less than that of the NNO buffer, sulfur in the silicate melt is the limiting factor in the ability of the melt to transport gold. It was also found that the solubility of gold in CFSL and pyrrhotite in Au-metal saturated systems is a function of sulfur fugacity. This suggests that small amounts of sulfide left behind under conditions of relatively high sulfur fugacity may have high concentrations of gold, which may then result in high concentrations of gold in silicate melts during a subsequent re-melting event, particularly if the sulfides are completely absorbed during melting.

Partition coefficients among the phases in this study range widely. Zn, Co, Cu, Ag, and Au partition into CFSL and pyrrhotite relative to the silicate melt, while Ti, V, and Mn prefer the melt. Molybdenum prefers pyrrhotite to the silicate melt, but the melt to CFSL. All of the elements studied except Co and Mo partition into CFSL to a greater degree than into pyrrhotite. $D_{Au}^{CFSL/pyrrhotite}$ in this study is greater than $D_{Au}^{FSOL/pyrrhotite}$ in Simon et al. (2008). This is similar to the findings of Jugo et al. (1999), where Au favored the more Cu-rich intermediate-solid-solution ($CuFeS_2$)

over pyrrhotite ($Fe_{1-x}S$). Sulfide/silicate melt partition coefficients for both pyrrhotite and CFSL are greater than in Simon et al. (2008), which is likely related to the differences in the silicate melt composition, *i.e.* hydrous andesitic melt versus dry rhyolitic melt. Molybdenum showed less chalcophile behavior than in Mengason et al. (2011), again likely due to the more depolymerized structure of the silicate melt. On the other hand, it partitioned preferentially into pyrrhotite over CFSL, despite the lower long-range order of the liquid phase. This may indicate coupled substitution of Cu and Mo for Fe in pyrrhotite.

The effect of sulfides present in the source region during partial melting on the likelihood of porphyry deposit formation is highly variable. The fraction of sulfide remaining in the residual phases and the initial bulk concentration of copper control the stability of CFSL, and all of the ore metals, except molybdenum, partition more strongly into CFSL. Models with low initial bulk concentrations of copper suggest a steady decrease in the likelihood of porphyry deposit formation, as higher sulfide fractions are considered. However in models with a higher initial concentration of copper, a low fraction of sulfide produced CFSL and reduces the likelihood of porphyry Cu, and in particular porphyry Cu–Au deposits. With a higher residual sulfide fraction, the effect on the potential for ore genesis is reduced as dilution of the copper favors the stability of pyrrhotite over CFSL. Variation in the loss of individual elements is complex, but in general, Cu:Au ratios will be higher in the forming silicate melt if CFSL is present, will decrease with increasing mass fraction of pyrrhotite over CFSL, and be the lowest if pyrrhotite alone is present.

Consideration of phase relations of the Cu–Fe–S–O system, and analysis of the silicate melt and sulfide phases in the experiments presented here, has led me to postulate that the boundary between pyrrhotite and CFSL is a reaction boundary. During crystallization, CFSL would be produced followed by pyrrhotite, rather than have a period in which both CFSL and pyrrhotite form together. Two scenarios of fractional crystallization were modeled by using partition coefficients determined in this study. For both scenarios, sulfides made up only 0.1 wt % of the crystalizing phases. Starting with 25 ppm Cu, ~ 15% of the initial Au and ~ 35% of the initial Cu is lost to sulfide phases. Starting with 65 ppm Cu, ~ 50% of the Ag, ~60% of the Cu, and greater than 99% of the Au is lost to the sulfide phases.

The trends in copper concentration with increasing silica concentration in the Bonanza and Talkeetna arc sections detailed in section 3.2.3 are broadly representative of the two models of fractional crystallization presented here. The plot in Figure 3-2 of the concentration of copper in rocks from the Bonanza arc section shows a steady decline with increasing SiO_2 wt %, consistent with the model of a relatively low initial copper concentration preventing the formation of CFSL during fractional crystallization, resulting in a smooth function of copper loss with crystallization. In contrast, the plot of the concentration of copper in rocks from the Talkeetna arc section shows a rapid initial drop in copper concentration with increasing SiO_2, followed by a more steady decline, which would be more consistent with the model of a higher initial concentration of copper and the presence of CFSL during early stages of fractional crystallization, followed by a slow removal of copper by pyrrhotite. The rocks of these arc sections are not quenched melts, and they have

undergone alteration, but the trends recorded suggest the plausibility of the model scenarios. A more direct example of a trend in copper concentration with SiO_2 concentration consistent with early saturation by CFSL followed by pyrrhotite is found in the silicate melt inclusions from Santa Rita, New Mexico, reported by Audetat and Pettke (2006), who further report the compositions of sulfide inclusions with 46 wt % copper from basaltic andesites, while sulfide inclusions are primarily limited to pyrrhotite with 1–6 wt % copper in more evolved diorites and rhyodacites.

Porphyry deposits are associated with intrusions varying in silica content, with porphyry Cu–Au and Au deposits associated with intrusions with SiO_2 in the range of 45–65 %, and porphyry Cu deposits associated with intrusions with SiO_2 in the range of 60–72% SiO_2 (Sinclair 2007). Speculating based on the modeling performed here, the lack of gold recovery from porphyry deposits that are potentially associated with a greater degree of crystallization (higher SiO_2) would be consistent with a history of sequestration of gold by CFSL separated from the melt along with other cumulate phases. The likelihood of porphyry Cu–Au deposit formation would not be greatly reduced at only small degrees of fractional crystallization (lower SiO_2) if pyrrhotite but not CFSL were removed.

There are a range of potential outcomes from sulfide–silicate melt interactions in subduction zone magmatism, in terms of the likelihood for magmatic hydrothermal ore-deposit genesis, as well as the ratio of metals in any deposit created. The saturation of a silicate melt by pyrrhotite and/or CFSL studied here has been applied to limited cases of partial melting and fractional crystallization. Future evaluation of the solubility of Cu-rich sulfides at other temperatures, fO_2, and fS_2, may allow for

more detailed modeling of sulfide–silicate melt interactions during the differentiation of magmas in subduction zones, which in turn may allow for better identification of regions for exploration based on ore metal ratios in surveyed intrusions.

Chapter 4: Conclusions

Sulfides have been shown to have the capacity to host a significant portion of metals associated with porphyry deposits with magma due to the chalcophile nature of those elements. The separation of sulfides from the magma removes a portion of the total metal that would have been available for later ore-forming processes. This may occur when sulfides are retained in the source region during partial melting, or when sulfides are trapped with other cumulate phases during fractional crystallization. In either case, the loss of metals sequestered in those sulfides reduces the likelyhood of porphyry or related magmatic–hydrothermal deposit formation, or may alter the ratio of metals within such deposits.

One goal of this research was to evaluate whether the loss of Cu-rich sulfide liquids (CFSL) had the capacity to significantly reduce the availability of Cu, Mo, Ag, and Au for deposit formation. Of particular interest was how the effect of CFSL separation from magma would differ from the separation of other sulfide phases (i.e., pyrrhotite). Another important goal was to quantify the conditions in intermediate silicic magmas that would permit CFSL saturation, from partial melting to ultimate plutonic consolidation. Summaries of my findings in the pursuit of this goal are presented here.

4.1 Summary of Cu–Fe sulfide phase assemblages as a function of temperature

The work began with consideration of phase diagrams in the system Cu–Fe–S and later with consideration of experiments designed to expand those diagrams detailed in chapter 3. Individual sulfide phases have a limited range of temperatures over which they are stable. For a given temperature, only a subset of possible sulfides may be stable. If a silicate melt is saturated with respect to a sulfide phase, then of those possible sulfide phases, the concentration of copper in the silicate melt will control which will be present ranging from Cu-poor (e.g., pyrrhotite, $Fe_{1-x}S$) to very Cu-rich (e.g., bornite, Cu_5FeS_4). The following discussion is restricted to sulfides in the system Cu–Fe–S–O with concentrations of Cu less than ~40%.

At temperatures greater than approximately 1200ºC, a liquid sulfide phase is the only sulfide phase stable in the magma. The liquid would have a composition between end members FSOL and CFSL (in the simple systems studied in this paper). Sulfide liquids in the experiments by Ripley et al. (2002) and Holzheid and Lodders (2002) fall into this range at the copper-rich end of the spectrum. These temperatures (~1200ºC) are most relevant to partial melting in the mantle wedge, and to crystallization of basalts pooling near the base of the crust. Although pyrrhotite is not stable at these temperatures, it can provide a common reference between experiments in this study and those of Mengason (2007), Simon et al. (2008) and Mengason et al. 2011). Comparing $D_i^{CFSL/po}$ and $D_i^{FSOL/po}$ between the studies suggests that Au and Ag will partition more strongly into liquids close to the CFSL end member than the FSOL end member.

At temperatures below less than approximately 850ºC (poorly defined in the complex Cu–S–Fe–O system), the pertinent copper-bearing phases are all crystalline (e.g., intermediate solid solution *(iss),* $CuFeS_2$). For example, experiments reported in Jugo et al. (1999) performed at 850ºC contained a rhyolitic melt saturated with pyrrhotite and iss, and experiments reported in Bell et al. (2009) performed at 800ºC and contained a haplogranitic melt saturated with pyrrhotite and iss. However, also reported in Bell et al. (2009) were experiments at the same T, P conditions but with greater bulk concentration of copper which produced a sulfide liquid suggesting that sulfide liquids can persist in special cases to even lower temperatures.

In between these temperatures (~ 850ºC to ~1200ºC), between a region of all liquid sulfides, and one of all crystalline sulfides (at least at the lower concentrations of copper discussed here) there is a range of temperatures dominated by the coexistence of liquid and crystalline sulfides. And within this range, there are two distinct sulfide assemblages, the boundary between which is defined by temperature, fS_2, and fO_2.

On the higher-temperature side of the boundary (which decreases at lower, fS_2, and fO_2), the stable sulfide phases include pyrrhotite and a sulfide liquid with a composition ranging from CFSL to FSOL. In this case, both phases can be stable with concentrations of copper at or near zero (Simon et al. 2008). Below the boundary (~1050ºC at the fS_2, and fO_2 of experiments here), the stable sulfide phases include pyrrhotite and a sulfide liquid restricted to compositions close to CFSL. In this case, copper acts as an essential constituent of CFSL, and there is a minimum concentration of copper below which it is not stable. Run products from the

experiments in chapter 3 are examples this range of possible phase assemblages. Given the greater affinity of chalcophile elements for sulfide liquids over pyrrhotite, subtleties of phase relationships in this range of temperatures may strongly influence the potential for ore formation.

Within this temperature range fall silicate melts of intermediate compositions. This study was conducted with one nominal melt composition of melt (andesitic, see Table 3-5) at one temperature (1000ºC) and at water saturation. Commonly the run product glasses from these experiments contain a very small fraction of crystals, and only a few of the experiments are wholly crystal-free, indicating that the silicate melts in were near-liquidus. This has implications for the range of melt compositions to which the sulfide assemblages studied here apply.

For more mafic bulk rock/magma compositions at similar temperatures, the sulfide assemblages examined in this study would be in equilibrium with melts of andesitic composition, but with a high proportion of silicate crystals. The results of these experiments are generally applicable to such magmas. Likewise, because the melt is already water-saturated, the addition of more water to the starting materials would have no direct effect on the silicate melt composition. Starting with a less mafic source material, a less mafic (more felsic) melt is generated. Likewise, starting with less water in the starting materials could lead to a less mafic (more felsic) melt. Considering the formation of silicate melts by partial melting in the lower crust, this temperature (1000ºC) and sulfide phase assemblage (CFSL + pyrrhotite) is applicable to andesitic to felsic compositions, the same range of compositions of shallow intrusions associated with porphyry and related magmatic–hydrothermal deposits.

In the case of silicate melts produced by the polythermal fractional crystallization of primary, mantle-derived basalt, the results of this study could be applied to a range of the compositions that are sequentially produced including intermediate (andesitic) to more felsic (dacitic) melt compositions. The temperature range of this study could likely encompass the transition from sulfide liquid to crystalline sulfide saturation in such a magma, and may therefore be accompanied by a sharp change in the trend of the concentration of copper in the silicate melt as a function of SiO_2 (or other measure of magma evolution).

Although more information on the stability of these sulfide phases (and the attendant partition coefficients for ore metals among these phases and the silicate melt) is needed across temperatures in the range 1200ºC to ~850ºC to fully understand the effects of sulfide porphyry and related deposits, the experiments described above are sited at an important point within that range.

4.2 Tools and observations

This research effort included the development of a number of tools en route, including revised analytical methods, or data from simplified systems with which to compare results from more complex experiments.

The research in chapter two is a case in point. That project was undertaken to provide a tool that would allow evaluation of sulfur fugacity in experiments from the Cu-rich pyrrhotite present among the run products. The proportion of $CuS_{0.5}$ + FeS in the system $CuS_{0.5}$–FeS–S_2 should be used to calculate sulfur fugacity in pyrrhotite

with appreciable copper content. Mathematically, in this method, log fS_2 is related to $2[(X_{Cu}+X_{Fe})/(1.5X_{Cu}+X_{Fe}+X_S)]$. This simple equation permits the application of the equation of Toulmin and Barton (1964) to pyrrhotites with elevated concentrations of copper. Accounting for the effect of copper on the thermodynamic properties of pyrrhotite also allows for the calculation of fS_2 from fO_2 in copper-bearing systems saturated with both pyrrhotite and magnetite following Whitney (1984).

The new furnaces and vessels designed and built in our laboratory made these experiments possible. The final design of the furnaces allowed the pressure vessels to attain experimental temperatures rapidly and to be maintained at the run temperature with only a small temperature gradient over the length of the capsule (<10º C over the length of the capsule).

Ar–H_2 mixed-gas pressure medium control of H_2 fugacity in the pressure vessel was included in the design, and implemented by myself and Zoltan Zajacz (currently at ETH). The solid-state oxygen fugacity buffers in these experiments were supplemented by this method, which prolonged their useful lifetime. In addition to data presented here, experiments have also been performed on pressure loss as a function of time using hydrogen gas, and that loss has been modeled to calculate the effective permeability of the MHC alloy. Along with oxygen fugacity sensor experiments run by Zoltan Zajacz in TZM vessels, we plan to provide a useful and well-calibrated tool to the experimental community for external control of oxygen fugacity in TZM and MHC cold-seal pressure vessels.

Experiments in chapter 3 that were performed with silica tubes were designed to yield data on the systems: Cu–Fe–S, Au–Cu–Fe–S, Cu–Fe–S–O, and Au–Cu–Fe–

S–O. These experiments were performed to place the results of the hydrothermal experiments into context, as phase relationships in existing Cu–Fe–S phase diagrams were found to differ significantly from the more complex system in experiments presented here, and magmatic systems in general.

Data from the silicate tube experiments in chapter 3 reveal the effect of oxygen and gold on the compositions of coexisting CFSL and pyrrhotite. In both cases, the concentration of copper in the CFSL and in coexisting pyrrhotite decrease with increasing oxygen and/or gold activity in the system. In these experiments, the addition of oxygen alone decreased the concentration of copper in pyrrhotite by ~30%, gold-saturation alone by ~20%, and oxygen- and gold-saturation by ~50%.

I also identified a systematic relationship between sulfur fugacity and gold concentration in gold-saturated CFSL and pyrrhotite. The mole fraction of $AuS_{0.5}$ in both CFSL and pyrrhotite follows a power law relationship $X_{AuS0.5}=(K')(fS_2^{0.25})$, where K' is the effective equilibrium constant (See Figures 3-11 and 3-12 in chapter 3). K' calculated from both silica tube and hydrothermal experiment is 0.05 for CFSL, and 0.00028 for pyrrhotite.

Analyzing the Cu–Au alloy recovered from the run products of the silica tubes allowed the activity of Cu to be calculated in the system ($a_{Cu}^{Cu-Au-alloy} \sim 0.01$) with coexisting pyrrhotite and CFSL, as well as the activity of Au ($a_{Au}^{Cu-Au-alloy} \sim 0.97$). This also yielded the equilibrium Cu/Au ratio for the capsules of the hydrothermal experiments, which was less than initially expected. This dovetails with findings from the hydrothermal experiments in which the concentration of Cu in the silicate melt in equilibrium with CFSL is lower than what many researchers might expect.

Supporting evidence is also provided for the application of partition coefficients ($D_i^{sulfide/sulfide}$) that were calculated at atmospheric conditions to questions of geologic interest within the crust by demonstrating the similarity of partition coefficients calculated from experiments performed at low pressure (silica tube) to similar experiments at 150 MPa in a hydrous system (cold-seal pressure vessel).

One of the fundamental goals of this study was to determine the equilibrium concentration of Cu in the silicate melt among the experiments saturated with pyrrhotite and CFSL. A value of this parameter is calculated in chapter 3 for experiments across a range of log fS_2 of approximately -0.15 to -0.5 (bar), and a range of fO_2 from the CCO fO_2 buffer to the NNO fO_2 buffer, in an andesitic melt with 5–7 wt % FeO at 1000ºC, 150 MPa, and water saturation. Based on a comparison of the values across the experiments, I suggest one value for this range: 32±4 ppm (based on 10 experiments, uncertainty calculated as the standard deviation of the mean). This parameter represents a major divide among magmas, separating those that can include a silicate melt and pyrrhotite, and those that can include a silicate melt and CFSL. In an experiment with magnetite saturation, fO_2 = NNO, and FeO in the silicate melt = 9.7 wt %, the value was much higher: 120±10 ppm (standard deviation of individual analyses).

Partition coefficients determined from this study emphasize the potential difference between having pyrrhotite or CFSL separated from the silicate melt. The full list of recommended partition coefficients from this study is presented in chapter 3, Table 3-12. One of the hypotheses of this research was that $D_{Au}^{CFSL/melt}$ would be significantly greater than $D_{Au}^{po/melt}$ based on comparison with previous studies of Au

partitioning in sulfides (Jugo et al. 1999, Bell et al. 2009). $D_{Au}^{CFSL/melt}$ is approximately two orders of magnitude greater than $D_{Au}^{po/melt}$. Data from previous experimental studies suggested that Ag would behave in a manner similar to Au, and $D_{Ag}^{CFSL/melt}$ is approximately two orders of magnitude greater than $D_{Ag}^{po/melt}$. In contrast to Mengason et al. (2011) in which $D_{Mo}^{FSOL/melt}$ is greater than $D_{Mo}^{pyrrhotite/melt}$, $D_{Mo}^{CFSL/melt}$ is about ¼ $D_{Mo}^{po/melt}$ in the current study.

Data from the hydrothermal experiments also support the solubility of gold in the silicate melt as a function of the solubility of sulfur at low fO_2 (less than the NNO buffer), adding to the growing body of evidence from Jégo et al. (2010) and Botcharnikov et al. (2010, 2011), also working with andesitic silicate melts.

Together, the tools needed to run the experiments, and the observations from the experiments, represent the raw output of this study.

4.3 Effect of Cu–Fe sulfide on metal budgets

Partial melting and fractional crystallization will both apply to some degree to the generation of intermediate to felsic silicate melts in magmatic systems in subduction zones. It is useful, however, to consider the effect of the presence of sulfides on one or the other process to produce limiting cases.

In the case of andesitic melts produced by partial melting in the lower crust, those produced at 1000ºC may form in the presence of pyrrhotite alone, pyrrhotite and CFSL, or CFSL alone, depending on the proportion of sulfide to silicate melt and the concentration of copper in the total volume undergoing partial melting. Sulfides

retained in the source region will sequester metals and reduce the likelihood of magmatic–hydrothermal deposit generation. The effect of 40% partial melting of gabbro in the lower crust was modeled to evaluate differences in the loss of ore metals. With a low initial bulk concentration of copper, pyrrhotite alone is formed. A small fraction of sulfide retained in the source region will have little effect on the formation of deposits. Calculations performed with a higher fraction of sulfide suggest that 0.2 wt % sulfide will decrease the likelihood of porphyry copper or to a lesser extent porphyry Cu–Au deposit formation. With a higher initial concentration of copper, a very different scenario evolves. At a low sulfide fraction, CFSL is stable which can sequester a large percentage of the Cu, Ag, and Au. At very low sulfide fractions, it is noteworthy that gold is removed to a greater extent than copper. However, calculations performed with a larger fraction of sulfide in the source region dilute the copper, resulting in a mix of pyrrhotite and CFSL in which case the effects are complex and alter greater the metal ratios, or pyrrhotite only in which case the results are similar to the lower initial copper model. In general, the effects of sulfide retention during partial melting are very depending on the ratio of copper to sulfide in the source region.

Significant to the case of fractional crystallization, based on analysis of the sulfide phases and the silicate melt, I propose that there is a reaction boundary between CFSL and pyrrhotite. Fractional crystallization can result if heat is lost by the magma during the passage through the crust. Sulfur concentration at sulfide saturation decreases with decreasing temperature and increasing SiO_2 concentration of the silicate melt, resulting in the formation of sulfide phases. During fractional

crystallization of a silicate melt with a concentration of copper greater than the value characteristic of cosaturation with pyrrhotite + CFSL, CFSL will form first, followed by pyrrhotite, upon cooling. There will not be a period where both are produced, as would be the case along a cotectic boundary, or in the case of batch crystallization. The effects of saturation with sulfides on the concentrations of ore metals are illustrated in chapter 3 in Figure 3-18. Starting with a concentration of copper in the silicate melt greater than the critical value of cosaturation, the concentrations copper steeply decreases and levels off, and the concentration of gold is greatly reduced. The total amount of Ag and Au remaining compared to the initial amount has decreased by 50% (Ag) and > 99 % (Au). Starting with a concentration of copper in the silicate melt less than the critical value, the concentrations of Mo, Ag, and Au do not decrease. The total amount of Ag and Au remaining compared to the initial amount has decreased by 3% (Ag) and 15% (Au). In general, the trend of the loss of copper is consistent. Also as noted in chapter 3, porphyry Cu–Au and Au deposits are associated with less evolved (lower SiO_2) intrusions than porphyry Cu deposits. The lack of gold mineralization (i.e., porphyry Cu as opposed to porphyry Cu–Au deposits) in systems with higher SiO_2 wt % would be consistent with the loss of gold to CFSL, while the likelihood of porphyry Cu–Au deposits would not be reduced by low degrees of crystallization if pyrrhotite, but not CFSL, was stable.

These cases are examples of how sulfide phase assemblages predicted from the concentrations of copper in the silicate melt of these experiments combined with the partition coefficients from this study can be applied to arc-magmatic systems. Further examples of the necessary conditions for the saturation of Cu-rich sulfides at

different temperatures will allow for modeling across a range of temperatures and conditions.

Bibliography

Ague, J. J., and Brimhall, G. H. (1988) Regional variations in bulk chemistry, mineralogy, and the compositions of mafic and accessory minerals in the batholiths of California. Geological Society of America Bulletin; **100**:891–911.

Annen, C., Blundy, J.D., Sparks, R.S.J. (2006) The genesis of intermediate and silicic magmas in deep crustal hot zones. Journal of Petrology; **47**(3):505–539.

Arnold, R. G. (1967) Range in composition and structure of 82 natural terrestrial pyrrhotites. The Canadian Mineralogist; **9**:31–50.

Audétat, A. and Pettke, T. (2006) Evolution of a Porphyry-Cu Mineralized Magma System at Santa Rita, New Mexico (USA). Journal of Petrology; **47**(10): 2021–2046.

Audétat, A., Dolejs, D., and Lowenstern, J. (2011) Molybdenite Saturation in Silicic Magmas: Occurrence and Petrological Implications. Journal of Petrology; **52**(5):891–904.

Ballhaus, C., Tredoux, M. and Spath, A. (2001) Phase relations in the Fe–Ni–Cu–PGE–S system at magmatic temperature and application to massive sulphide ores of the Sudbury Igneous Complex. Journal of Petrology; **42**(10):1911–1926.

Barnes, S. J., Cox, R. A. and Zientek, M. L. (2006). Platinum-group element, gold, silver and base metal distribution in compositionally zoned sulfide droplets from the Medvezky Creek Mine, Noril'sk, Russia. Contributions to Mineralogy and Petrology; **152**(2):187–200.

Bell, A. S., Simon, A., and Guillong, M. (2009) Experimental constraints on Pt, Pd and Au partitioning and fractionation in silicate melt–sulfide–oxide–aqueous fluid systems at 800 degrees C,150 MPa and variable sulfur fugacity. Geochimica et Cosmochimica Acta; **73**:5778–5792.

Bell, A.S., Simon, A., and Guillong, M. (2011) Gold solubility in oxidized and reduced, water-saturated mafic melt. Geochimica et Cosmochimica Acta; **75**(7): 1718–1732.

Berger, B.R., Ayuso, R.A., Wynn, J.C., and Seal, R.R. (2008) Preliminary model of porphyry copper deposits. U.S. Geological Survey Open-File Report; 2008–1321.

Blundy, J., Cashman, K. and Humphreys, M. (2006). Magma heating by decompression-driven crystallization beneath andesite volcanoes. Nature; **443**(7107):76–80.

Borisov, A., and Palme, H. (1996) Experimental determination of the solubility of Au in silicate melts. Mineralogy and Petrology; **56**:297–312.

Botcharnikov, R.E., Linnen, R.L., Holtz, F. (2010) Solubility of Au in Cl- and S-bearing hydrous silicate melts. Geochimica et Cosmochimica Acta; **74**(8):2396–2411.

Botcharnikov, R.E., Linnen, R.L., Wilke, M., Holtz, F., Jugo, P.J., and Berndt, J. (2010) High gold concentrations in sulphide-bearing magma under oxidizing conditions. Nature Geoscience; **4**:112–115.

Brenan, J. M. (2002) Re–Os fractionation in magmatic sulfide melt by monosulfide solid solution. Earth and Planetary Science Letters; **199**(3–4):257–268.

Buddington, A. F., and Lindsley, D. H. (1964) Iron-titanium oxide minerals and synthetic equivalents. Journal of Petrology; **5**:310–357.

Burnham, C.W. and Jahns, R.H. (1962) A method for determining the solubility of water in silicate melts. American Journal of Science; **260**:721–745.

Calvache, M. L. and Williams, S. N. (1997). Emplacement and petrological evolution of the andesitic dome of Galeras volcano, 1990–1992. Journal of Volcanology and Geothermal Research; **77**(1–4):57–69.

Campbell, I.H., Naldrett, A.J. (1979) The influence of silicate:sulfide ratios on the geochemistry of magmatic sulfides. Economic Geology; **74**:1503–1506.

Candela, P. A. (1989) Magmas, Volatiles and Metallogenesis. In Naldrett, A., and Whitney, J., eds., Ore Deposition Associated with Magmas. Reviews in Economic Geology, Society of Economic Geologists, 223–233.

Candela, P. A. and Holland, H. D. (1986) A Mass-Transfer Model for Copper and Molybdenum in Magmatic Hydrothermal Systems – the Origin of Porphyry-Type Ore-Deposits. Economic Geology and the Bulletin of the Society of Economic Geologists; **81**(1):1–19.

Candela, P.A., and Piccoli, P.M. (2005) Magmatic Proceses in the Development of Porphyry Type Ore Systems. In: Economic Geology 100th Anniversary Volume (Eds: J.W. Hedenquist, J.F.H. Thompson, R.J., Goldfarb, J.P. Richards); **100**(5):25–38.

Carroll, M.R., and Rutherford, M.J. (1985) Sulfide and sulfate saturation in hydrous silicate melts. Journal of Geophysical Research; **90**: C601–C612.

Chang, Y.A., Neuman, J.P., Choudary, U.V. (1979) Phase Diagrams and Thermodynamic Properties of Ternary Copper–Sulfur–Metal Systems. In: INCRA Rep; PP 191; Report No INCRA Monograph VII; The Metallurgy of Copper. Feb. 1.

Chase, M.W. (1998) NIST–JANAF Thermochemical Tables, Fourth edition. NIST–JANAF Thermochemical Tables 2 Volume–Set (Journal of Physical and Chemical Reference Data Monographs). American Institute of Physics.

Core, D.P., Kesler, S.E, Essene, E.J. (2006) Unusually Cu-rich magmas associated with giant porphyry copper deposits: Evidence from Bingham, Utah. Geology; **34**(1):41–44.

Crocket, J.H, Fleet, M.E., S, W. E. (1997) Implications of composition for experimental partitioning of platinum-group elements and gold between sulfide liquid and basalt melt: The significance of nickel content. Geochimica et Cosmochimica Acta; **61**(19):4139–4149.

de Hoog, J.C.M., Mason, P.R.D., van Bergen, M.J. (2001) Sulfur and chalcophile elements in subduction zones: constraints from a laser ablation ICP–MS study of melt inclusions from Galunggung Volcano, Indonesia. Geochimica et Cosmochimica Acta; **65**:3147–3164.

DeBari, S.M., Anderson, R.G., Mortensen, J.K. (1999) Correlation among lower to upper crustal components in an island arc: the Jurassic Bonanza arc, Vancouver Island, Canada. Canadian Journal of Earth Science; **36**:1371–1413.

Defant, M.J., Drummond, M.S. (1990) Derivation of some modern arc magmas by melting of young subducted lithosphere. Nature; **347**:662–665.

Drexler, J. W. (1984) Magmatic conditions from vitric units of the Julcani district, Peru. PhD. dissertation, PhD.: Houghton, Michigan Technological University.

Englander, L. (2005) An Experimental Study of Silver Partitioning in Sulfide–Oxide–Melt Systems at 800°C. Geology Department. College Park, University of Maryland. M.S. Thesis:134.

FactSage (http://www.factsage.com/) FSnobl database: http://www.crct.polymtl.ca/fact/phase_diagram.php?file=Au-Cu.jpg&dir=FSnobl.

Fleet, M.E. (2006) Phase Equilibria at High Temperatures. In: Reviews in Mineralogy and Geochemistry. David J. Vaughn, Editor. Vol. **61**: 365–419.

Fleet, M. E., Chryssoulis, S. L., Stone, W. E., and Weisener, C. G. (1993) Partitioning of Platinum-Group Elements and Au in the Fe–Ni–Cu–S System – Experiments

on the Fractional Crystallization of Sulfide Melt. Contributions to Mineralogy and Petrology; **115**(1): 36–44.

Francis, R.D. (1990) Sulfide globules in mid-ocean ridge basalts (MORB), and the effect of oxygen abundance in Fe–S–O liquids on the ability of those liquids to partition metals from MORB and komatiite magmas. Chemical Geology; **85**(3–4):199–213.

Gaetani, G. A., and Grove, T. L. (1997) Partitioning of moderately siderophile elements among olivine, silicate melt, and sulfide melt: Constraints on core formation in the Earth and Mars: Geochimica et Cosmochimica Acta; **61**:1829–1846.

Greene, A. R., DeBari, S. M., Kelemen, P. B., Blusztajn, J. and Clift, P. D. (2006) A detailed geochemical study of island arc crust: the Talkeetna Arc section, south-central Alaska. Journal of Petrology; **47**(6):1051–1093.

Grove, T. L., Parman, S. W., Bowring, S. A., Price, R. C. & Baker, M. B. (2002) The role of an H_2O-rich fluid component in the generation of primitive basaltic andesites and andesites from Mt. Shasta region, N California. Contributions to Mineralogy and Petrology; **142**: 375–396.

Halter, W.E., Heinrich, C.A., Pettke, T., (2005) Magma evolution and the formation of porphyry Cu–Au ore fluids: evidence from silicate and sulfide melt inclusions. Mineralium Deposita: **39**:845–863.

Hamada, M., Fujii, T. (2008) Experimental constraints on the effects of pressure and H_2O on the fractional crystallization of high-Mg island arc basalt. Contributions to Mineralogy and Petrology; **155**, 767–790.

Hasse, K.M., Stroncik, N.A., Garbe-Schönberg, C.-D., Stoffers, P. (2006) Formation of island arc dacite magmas by extreme crystal fractionation: an example from Brothers seamount, Kermadec Island arc (SW Pacific). Journal of Volcanology and Geothermal Research; **152**: 316–330.

Hattori, K. (1996) Occurrence and origin of sulfide and sulfate in the 1991 Mount Pinatubo eruption products. In Newhall, C. G., and Punongbayan, R. S., eds., Fire and Mud: eruptions and lahars of Mount Pinatubo, Philippines: Seattle and London, University of Washington Press.

Hedenquist, J.W., and Lowenstern, J.B. (1994) The role of magmas in the formation of hydrothermal ore deposits. Nature; **370**: 519–527.

Hedenquist, J. W., Arribas, Jr., A., and Reynolds T. J. (1998) Evolution of an intrusion centered hydrothermal system: far Southeast-Lepanto porphyry and epithermal Cu–Au deposits. Philippines. Economic Geology; **93**: 373–404.

Herzberg, C.T., W.S. Fyfe, and Carr, M.J. (1983) Density constraints on the formation of the continental Moho and crust. Contribution to Mineralogy and Petrology; **84**:1–5.

Hildreth, W. and Wilson, C. J. N. (2007). Compositional zoning of the Bishop Tuff. Journal of Petrology; **48**(5): 951–999.

Hilton, D. R., Fischer, T. P., and Marty, B. (2002) Noble gases and volatile recycling at subduction zones, in Porcelli, D., Ballentine, C. J., and Wieler, R., eds., Noble Gases in Geochemistry and Cosmochemistry, 47. Reviews in Mineralogy & Geochemistry: Washington, Mineralogical Society of America, 319–370.

Holland, H. D. (1972) Granites, Solutions, and Base Metal Deposits. Economic Geology and the Bulletin of the Society of Economic Geologists; **67**(3): 281– &.

Holzheid, A., and Lodders, K. (2001) Solubility of copper in silicate melts as function of oxygen and sulfur fugacities, temperature, and silicate composition. Geochimica et Cosmochimica Acta; **65**:1933–1951.

Hopson, C. A., and Melson, W. G. (1990) Compositional trends and eruptive cycles at Mount St. Helens. Geoscience Canada; **17**:131–141.

Jugo, P. J., Candela, P. A., and Piccoli, P. M. (1999) Magmatic sulfides and Au : Cu ratios in porphyry deposits: an experimental study of copper and gold partitioning at 850 degrees C, 100 MPa in a haplogranitic melt pyrrhotite intermediate solid solution gold metal assemblage, at gas saturation. Lithos; **46**:573–589.

Jugo, P., Luth, R., and Richards, J. (2005) Experimental data on the speciation of sulfur as a function of oxygen fugacity in basaltic melts: Geochimica et Cosmochimica Acta; **69**:497–503.

Jugo, P.J. (2009) Sulfur content at sulfide saturation in oxidized magma. Geology 2009; **37**:415–418.

Jégo, S., Pichavant, M., and Mavrogenes, J.A. (2010) Controls on gold solubility in arc magmas: An experimental study at 1000°C and 4 kbar. Geochimica et Cosmochimica Acta; **74**:2165–2189

Kullerud, G. (1968) High temperature phase relations in the Cu–Fe–S system. Carnegie Institute of Washington Yearbook ’66 v. 1966–1967:404–409.

Kress, V. (1997) Thermochemistry of sulfide liquids. I. the system O–S–Fe at 1 bar. Contributions to mineralogy and petrology; **127**:176–186.

Kress, V., Greene, L.E., Ortiz, M.D., Mioduszewski, L. (2008) Thermochemistry of sulfide liquids IV: density measurements and the thermodynamics of O–S–Fe–Ni–Cu liquids at low to moderate pressures. Contributions to Mineralogy and Petrology; **156**(6):785–797.

Larocque, J., Canil, D. (2010) The role of amphibole in the evolution of arc magmas and crust: the case from the Jurassic Bonanza arc section, Vancouver Island, Canada. Contributions to Mineralogy and Petrology; **159**:475–492.

Larocque, A. C. L., James, A. S. and Siebe, C. (1998). Metal-residence sites in lavas and tuffs from Volcan Popocatepetl, Mexico: implications for metal mobility in the environment. Environmental-Geology; **33**(2/3): 197–208.

Larocque, A. C. L., Stimac, J. A., Keith, J. D. and Huminicki, M. A. E. (2000). Evidence for Open-System Behavior in Immiscible Fe–S–O Liquids in Silicate Magmas: Implications for Contributions of Metals and Sulfur to Ore-Forming Fluids. The Canadian Mineralogist; **38**: 1233–1249.

Luhr, J.F., Carmichael, I.S.E, Varekamp, J.C. (1984) The 1982 eruptions of El Chichón volcano, Chiapas, Mexico: mineralogy and petrology of the anhydrite-bearing pumices. Journal of Volcanology and Geothermal Research; **23**: 69–108.

Li, C., and Ripley, E.M. (2005) Empirical equations to predict the sulfur content of mafic magmas at sulfide saturation and applications to magmatic sulfide deposits. Mineralum Deposita; **40**: 218–230.

Li, C., and Ripley, E.M. (2009) Sulfur Contents at Sulfide–Liquid or Anhydrite Saturation in Silicate Melts: Empirical Equations and Example Applications. Economic Geology; **104**: 405–412.

Liu, Y., Samaha, N.T., and Baker, D.R. (2007) Sulfur concentration at sulfide saturation (SCSS) in magmatic silicate melts. Geochimica et Cosmochimica Acta; **71**: 1783–1799.

Lowenstern, J.B. (2001) Carbon dioxide in magmas and implications for hydrothermal systems. Mineralum Deposita; **36**(6):490–502.

Lynton, S. J., Candela, P. A., and Piccoli, P. M. (1993) An Experimental Study of the Partitioning of Copper between Pyrrhotite and a High-Silica Rhyolitic Melt. Economic Geology and the Bulletin of the Society of Economic Geologists; **88**(4): 901–915.

MacLean, W.H., and Shimazaki, H. (1976). The partition of Co, Ni, Cu, and Zn between sulfide and silicate liquids. Economic Geology; **71**(6):1049–1057.

Mavrogenes J.A., O'Neill H.S.C. (1999) The relative effects of pressure, temperature and oxygen fugacity on the solubility of sulfide in mafic magmas. Geochimica et Cosmochimica Acta; **63**(7–8): 1173–1180.

Mengason, M.J. (2007) Experimental Study of the Partitioning of Cu, Ag, Au, Mo, and W Among Pyrrhotite and Immiscible Fe–S–O and Silicate Melts. Geology Department, College Park, University of Maryland. M.S. Thesis. 105

Mengason, M., Piccoli, P. M., and Candela, P.A. (2010) An evaluation of the effect of copper on the estimation of sulfur fugacity (fS_2) from pyrrhotite composition. Economic Geology; **105**(6):1163–1169.

Mengason, M., Piccoli, P., Candela, P. (2011 – in press) Molybdenum, tungsten and manganese partitioning in the system pyrrhotite–Fe–S–O melt-rhyolite melt: impact of sulfide segregation on arc magma evolution. Geochimica et Cosmochimica Acta. *Accepted for publication.*

Mungall, J.E. (2002) Roasting the mantle: Slab melting and the genesis of major Au and Au-rich Cu deposits. Geology; **30**(10):915–918.

Mungall, J.E. (2002b) Empirical models relating viscosity and tracer diffusion in magmatic silicate melts. Geochimica et Cosmochimica Acta; **66**(1);125–143.

Mungall, J. E., Andrews, D. R. A., Cabri, L. J., Sylvester, P. J., and Tubrett, M. (2005) Partitioning of Cu, Ni, An, and platinum-group elements between monosulfide solid solution and sulfide melt under controlled oxygen and sulfur fugacities. Geochimica et Cosmochimica Acta; **69**(17): 4349–4360.

Müntener, O., Kelemen, P. B. & Grove, T. L. (2001) The role of H_2O during crystallization of primitive arc magmas under upper-most mantle conditions and genesis of igneous pyroxenites: an experimental study. Contributions to Mineralogy and Petrology; **141**:643–658.

Naldrett, A. J. (1969). A Portion of the System Fe–S–O between 900 and 1080°C and its Application to Sulfide Ore Magmas. Journal of Petrology; **10**(Part 2):171–201.

NAVDAT database (www.navdat.com) Database search on 7/26/2011: queried on Cu data present and igneous rocks according to names from original papers.

Otamendi, J.E., Ducea, M.N., Tibaldi, A.M., Bergantz, G.W., De La Rosa, J.D., and Vujovich, G.I. (2009) Generation of Tonalitic and Dioritic Magmas by Coupled Partial Melting of Gabbroic and Metasedimentary Rocks within the Deep Crust of the Famatinian Magmatic Arc, Argentina. Journal of Petrology; **50**(5):841–873.

Plafker, G., Nokleberg, W. J., Lull, J. S. (1989) Bedrock geology and techtonic evolution of the Wrangellia, Penninsular, and Chugach terranes along the Trans-Alaska crustal transect in the Chugach Mountains and Southern Copper River Basin, Alaka. Journal of Geophysical Research; **94**(B4)4255–4295.

Pankhurst, R. J., Rapela, C. W., Saavedra, J., Baldo, E. G., Dahlquist, J., Pascua, I. & Fanning, C. M. (1998) The Famatinian magmatic arc in the central Sierras Pampeanas: an Early to Mid-Ordovician continental arc on the Gondwana margin. In: Pankhurst, R. J. & Rapela, C.W. (eds) The Proto-Andean Margin of Gondwana. Geological Society, London, Special Publications; **142**:343–368.

Peach, C.L., Mathez, E.A., Keays, R.R. (1990) Sulfide melt–silicate melt distribution coefficients for noble metals and other chalcophile elements as deduced from MORB: implications for partial melting. Geochimica et Cosmochimica Acta; **54**:3379–3389.

Peregoedova, A., Barnes, S. J., and Baker, D. R. (2006). An experimental study of mass transfer of platinum-group elements, gold, nickel and copper in sulfur-dominated vapor at magmatic temperatures. Chemical Geology; **235**(1–2): 59–75.

Redmond, P. B., Einaudi, M. T., Inan, E. E., Landtwing, M. R., and Heinrich, C. A. (2004) Copper deposition by fluid cooling in intrusion-centered systems: new insights from the Bingham porphyry ore deposit, Utah. Geology; **32**(3): 217–220.

Ricci, J.E. (1951) The phase rule and heterogeneous equilibrium. New York, Dover Publications Inc.

Richards, J.P. (2009) Postsubduction porphyry Cu–Au and epithermal Au deposits: products of remelting of subduction-modified lithosphere. Geology; **37**:247–250.

Richards, J.P. (2011) Magmatic to hydrothermal metal fluxes in convergent and collided margins. Ore Geology Reviews; **40**:1–26.

Ripley, E. M., Brophy, J. G., and Li, C. S. (2002) Copper solubility in a basaltic melt and sulfide liquid/silicate melt partition coefficients of Cu and Fe. Geochimica et Cosmochimica Acta; **66**(15):2791–2800.

Rutherford, M. J. and Devine, J. D. (1991). Pre-eruption conditions and volatiles in the 1991 Pinatubo magma. EOS Transactions of the American Geophysical Union; **72**(44): 62.

Sattari, P., Brenan, J. M., Horn, I., and McDonough, W. F. (2002) Experimental constraints on the sulfide- and chromite-silicate melt partitioning behavior of rhenium and platinum-group elements: Economic Geology and the Bulletin of the Society of Economic Geologists; **97**:385–398.

Schmidt, M. W., and Poli, S. (1998) Experimentally based water budgets for dehydrating slabs and consequences for arc magma generation. Earth and Planetary Science Letters; **163**: 361–379.

Shishkina, T.A., Botcharnikov, R.E., Holtz, F., Almeev, R.R., and Portnyagin, M.V. (2010) Solubility of H_2O- and CO_2-bearing fluids in tholeiitic basalts at pressures up to 500 MPa. Chemical Geology; **277**:115–125.

Sillitoe, R.H. (2010) Gold-rich porphyry deposits: descriptive and genetic models and their role in exploration and discovery. Reviews in Economic Geology; **13**:315–345.

Simon, A.C., Pettke, T., Candela, P.A., Piccoli, P.M., Heinrich, C.A. (2006) Copper partitioning in a melt–vapor–brine–magnetite–pyrrhotite assemblage. Geochimica et Cosmochimica Acta; **70**(22):5583–5600.

Simon, A. C., Candela, P. A., Piccoli, P. M., Mengason, M., Englander, L. (2008) The effect of crystal-melt partitioning on the budgets of Cu, Au, and Ag. American Mineralogist; **93**(8–9):1437–1448.

Sinclair, W.D. (2007) Porphryr deposits. In: Goodfellow, W.D. (Ed.) Mineral deposits of Canada: a synthesis of major deposit types, district metallogeny, the evolution of geological provinces, and exploration methods. Geological Association of Canada, Mineral Deposits Division, Special Publication No. 5.

Sisson, T. W., Ratajeski, K., Hankins, W. B. and Glazner, A. F. (2005) Voluminous granitic magmas from common basaltic sources. Contributions to Mineralogy and Petrology; **148**:635–661.

Shishkina, T.A., Botcharnikov, R.E., Holtz, F., Almeev, R.R., and Portnyagin, M.V. (2010) Solubility of H_2O- and CO_2-bearing fluids in tholeiitic basalts at pressures up to 500 MPa. Chemical Geology; **227**(1–2):115–125.

Stimac, J. and Hickmott, D. (1994). Trace-element partition coefficients for ilmenite, orthopyroxene and pyrrhotite in rhyolite determined by micro-PIXE analysis. Chemical Geology; **117**: 313–330.

Stimac, J. and Hickmott, D. (1996) Ore Metal Partitioning in Intermediate-to-Silicic Magmas: PIXE Results on Natural Mineral/Melt Assemblages. Second Giant Ore Deposits Workshop, Kingston, Ontario, Canada.

Stone, W.E., Crocket, J.H., Fleet, M.E., (1990) Partitioning of palladium, iridium, platinum, and gold between sulfide liquid and basalt melt at 1200°C. Geochimica et Cosmochimica acta; **54**(8):2341–2344

Sunderman, B., Fries, S., Oats, W. (1998) A thermodynamic assessment of the Au–Cu system. Calphad; **22**(3):335–354.

Stuller, B. C. (2001). The partitioning behavior of manganese, cobalt, nickel, zinc, molybdenum, tungsten and gold between pyrrhotite and a rhyolitic melt. Geology. College Park, University of Maryland. M.S. Thesis.

Tatsumi, Y., 2003. Some constraints on arc magma genesis. In: Eiler, J. (Ed.), Inside the Subduction Factory. : Geophysical Monograph, 138. American Geophysical Union, Washington, DC, pp. 277–292.

Tatsumi, Y., and Eggins, S. (1995) Subduction Zone Magmatism. Oxford: Blackwell Scientific.

Toulmin, P., and Barton, P. B. (1964) A thermodynamic study of pyrite and pyrrhotite. Geochimica et Cosmochimica Acta; **28**:641–671.

Ueda, A., and Itaya, T. (1981) Microphenocrystic pyrrhotite from dacite rocks of Satsuma-Iwojima, Southwest Kyushu, Japan, and the solubility of sulfur in dacite magma: Contributions to Mineralogy and Petrology; **78**:21–26.

Wallace, P. J. (2005) Volatiles in subduction zone magmas: concentrations and fluxes based on melt inclusion and volcanic gas data. Journal of Volcanology and Geothermal Research; **140**:217–240.

Wallace, P.J., and Carmichael, I.S.E. (1994) S-speciation in submarine basaltic glasses as deter- mined by measurements of S-ka X-ray wavelength shifts: American Mineralogist; **79**:161–167.

Warshaw, C. M. and Smith, R. L. (1988) Proxenes and Fayalites in the Bandelier Tuff, New-Mexico - Temperatures and Comparison with Other Rhyolites. American Mineralogist; **73**(9–10):1025–1037.

Whitney, J. A. (1984) Fugacities of sulfurous gases in pyrrhotite-bearing silicic magmas. American Mineralogist; **69**:69–78.

Witter, J.B., Kress, V.C., Delmelle, P., and Stix, J. (2004) Volatile degassing, petrology, and magma dynamics of the Villarrica Lava Lake, Southern Chile. Journal of Volcanology and Geothermal Research; **134**:303–337.

Witter, J. B., Kress, V. C. and Newhall, C. G. (2005) Volcan Popocatepetl, Mexico. Petrology, magma mixing, and immediate sources of volatiles for the 1994 - Present eruption. Journal of Petrology; **46**(11):2337–2366.

Yang, X. M., Lentz, D. R., and Sylvester, P. J. (2006) Gold contents of sulfide minerals in granitoids from southwestern New Brunswick, Canada. Mineralium Deposita; **41**(4): 369–386.

Zajacz, Z., Candela, P.A., Piccoli, P.M., Wälle M., Sanchez-Valle, C. (2011) The Solubility of Au and Cu in Andesite Melts. Mineralogy; **75**(3):2242.

Zajacz, Z., Seo, J.H., Candela, P.A., Piccoli, P.M., Tossell, J.A. (2011) The solubility of copper in high-temperature magmatic vapors: A quest for the significance of various chloride and sulfide complexes. Geochimica et Cosmochimica Acta; **75**(10):2811–2827.